

AN ANALYSIS OF LANDSLIDE VOLUME, STRUCTURES, AND KINEMATICS FROM
SATELLITE IMAGERY OF THE 2016 LAMPLUGH ROCK AVALANCHE,
GLACIER BAY NATIONAL PARK AND PRESERVE, ALASKA

by

Erin K. Bessette-Kirton

A thesis submitted to the Faculty and the Board of Trustees of the Colorado School of Mines in partial fulfillment of the requirements for the degree of Master of Science (Geological Engineering).

Golden, Colorado

Date: _____

Signed: _____

Erin K. Bessette-Kirton

Signed: _____

Dr. Wendy Zhou

Thesis Advisor

Golden, Colorado

Date: _____

Signed: _____

Dr. Stephen Enders

Department Head

Department of Geology and Geological Engineering

ABSTRACT

During the past five years occurrences of large rock avalanches over glaciated terrain in Glacier Bay National Park and Preserve (GBNP), Alaska have drawn attention to the complex, highly variable, yet poorly understood dynamics of these events. The objective of this research is to study the emplacement processes of the Lamplugh rock avalanche through an analysis of the volume and distribution of material in conjunction with structures and surficial features within the deposit. This research demonstrates the ability to use high-resolution remotely sensed data to study rock avalanches in glaciated terrain and provides an improved framework with which to estimate many of the uncertainties affecting volume measurements in glacial environments. The Lamplugh rock avalanche occurred on June 28, 2016 and is the largest rock avalanche on record in GBNP. WorldView satellite stereo imagery was used to derive pre- and post-event, high-resolution (2m) Digital Elevation Models (DEMs). Differenced DEMs were used to calculate both source and deposit volumes and examine variations in deposit thickness. DEMs were also used in conjunction with high-resolution (~0.5m) optical imagery to map landslide structures and surficial features. The characterization of landslide structures and the evaluation of volume and thickness were used to make interpretations about emplacement processes. Unmeasured ice changes between the acquisition of pre- and post-event imagery and the rock avalanche occurrence were found to underestimate the total volume of deposited material by 91%. A large amount of surficial material downslope of the source area, much of which was likely snow and ice, was scoured and entrained during emplacement. The rock avalanche deposit is also characterized by lateral and distal rims that are significantly thicker than the interior of the deposit. The examination of overall deposit geometry in addition to the identification of structures and surficial features within the deposit indicates that emplacement occurred as multiple surges of failed rock avalanche material. An improved understanding of rock avalanche processes is critical to future hazard assessments of rock avalanches travelling on ice within GBNP and in other glaciated regions.

TABLE OF CONTENTS

ABSTRACT	iii
LIST OF FIGURES	vii
LIST OF TABLES	x
ACKNOWLEDGMENTS	xii
CHAPTER 1 INTRODUCTION	1
CHAPTER 2 BACKGROUND	5
2.1 Prior Work	5
2.1.1 Inventory of Rock Avalanches in Glacier Bay National Park and Preserve.....	5
2.1.2 Morphologies and Structures of Rock-Avalanche Deposits.....	6
2.2 Study Area and the Lamplugh Rock Avalanche	10
CHAPTER 3 PURPOSE.....	15
CHAPTER 4 METHODS	16
4.1 WorldView Imagery	16
4.1.1 Acquired Imagery	17
4.2 Elevation Datasets	19
4.3 Ames Stereo Pipeline Workflow	19
4.3.1 Pre-processing and Pre-alignment	20
4.3.2 Stereo Correlation	21
4.3.3 Raster Conversion.....	23
4.4 DEM Generation	23
4.5 DEM Accuracy Analysis.....	24
4.6 DEM Differencing.....	26
4.7 Elevation Adjustments.....	27

4.7.1 Scenario 1: Areas of Net Positive Elevation.....	28
4.7.2 Scenario 1: Areas of Net Negative Elevation.....	30
4.7.3 Scenario 2: Areas of Net Positive Elevation.....	31
4.7.4 Scenario 2: Areas of Net Negative Volume.....	32
4.7.5 Scenario 3: Areas of Net Positive Volume.....	33
4.7.6 Scenario 3: Areas of Net Negative Volume.....	35
4.8 Volume, Thickness, and Center of Mass.....	36
4.8.1 Volume.....	37
4.8.2 Average Thickness.....	37
4.8.3 Center of Mass.....	37
4.9 Structural Mapping.....	38
CHAPTER 5 RESULTS.....	40
5.1 DEM Generation.....	40
5.2 DEM Accuracy Analysis.....	40
5.3 Differenced DEMs.....	42
5.4 Elevation Adjustments.....	45
5.5 Volume, Thickness, and Center of Mass.....	48
5.5.1 Volume and Average Thickness.....	48
5.5.2 Center of Mass.....	54
5.6 Structural Mapping.....	55
5.6.1 Strike-slip faults.....	55
5.6.2 Thrust faults.....	57
5.6.3 Fault scarps.....	57
5.6.4 Transverse ridges.....	59

5.6.5 Fensters	59
5.6.6 Run-up	62
CHAPTER 6 DISCUSSION.....	63
6.1 Independent Checks on Volume Analysis Methodology	63
6.1.1 Seasonal Snow and Ice Change	63
6.1.2 Ice Insulation and Differential Melting.....	65
6.1.3 Volume Calculation	67
6.1.4 Improvements on Volume Estimates	69
6.2 Deposit Geometry Comparisons.....	71
6.3 Emplacement Hypotheses	76
CHAPTER 7 CONCLUSION.....	82
REFERENCES	84
APPENDIX A.....	91
APPENDIX B.....	93
APPENDIX C.....	94
APPENDIX D.....	95

LIST OF FIGURES

Figure 2-1. Map of Glacier Bay National Park and Preserve showing the location of the Lamplugh rock avalanche (Alaska Department of Natural Resources, Information Resource Management, 1998a, 1998b; National Park Service, 2014).....	11
Figure 2-2. Profile of pre-event topography along the travel path of the Lamplugh rock avalanche.	13
Figure 4-1. Digital Globe Inc. image collected on 8/27/2016 showing the location of the six control areas used to assess the relative accuracy of DEMs produced in ASP.	25
Figure 4-2. Diagram showing the effect of unmeasured changes in surface elevation between the acquisition of pre-event imagery collected on 6/15/2016 and post-event imagery collected on 7/16/2016 and the occurrence of the Lamplugh rock avalanche on 6/28/2016 in deposit areas with net positive volumes. The elevation of the glacier surface at time t_i (light blue line) is subtracted from the surface elevation measured at time t_f (red line) during DEM differencing. The thickness of the deposit measured by DEM differencing (h_2) is not equivalent to the actual thickness of the deposit (th_{true}). True deposit thickness can be measured by summing the difference in elevation on the adjacent glacier surface between t_i and t_f (h_1) with h_2	29
Figure 4-3. Diagram showing the effect of unmeasured changes in surface elevation between the acquisition of pre-event imagery collected on 6/15/2016 and post-event imagery collected on 7/16/2016 and the occurrence of the Lamplugh rock avalanche on 6/28/2016 in deposit areas with net negative volumes. The elevation of the glacier surface at time t_i (light blue line) is subtracted from the surface elevation measured at time t_f (red line) during DEM differencing. Neither the height of scoured and entrained material ($h_{entrained}$) nor the height of material deposited in the scoured area are represented by the change in elevation measured between t_i and t_f in areas of the deposit (h_{2n}). Elevation change on the adjacent glacier surface between t_i and t_f is represented by the height of h_{1n} . The actual thickness of entrained material can be measured by subtracting h_{1n} from the sum of h_{2n} and h_{fill}	31
Figure 4-4. Diagram showing the added effect of differential ice melt on ice changes that are not measured during DEM differencing in net positive deposit areas. The change in height of the deposit, either due to melting of underlying ice or melting and densification within the deposit is assumed to be zero. The actual thickness of the deposit (th_{true}) is measured by subtracting the elevation change on the adjacent surface between t_e and t_f (h_3) from the sum of h_1 and h_2 . When observed from an adjacent location in space the presence of differential ice melt causes the observed deposit thickness ($th_{apparent}$) to be greater than th_{true}	33
Figure 4-5. Diagram showing the added effect of differential ice melt on ice changes that are not measured during DEM differencing in net negative deposit areas. The change	

in height of the deposit, either due to melting of underlying ice or melting and densification within the deposit is assumed to be zero. The actual thickness of entrained material ($h_{entrained}$) is measured by subtracting h_{1n} from the sum of h_{2n} and h_{fill} and the change in elevation on the adjacent surface between t_e and t_f (h_{3n})..... 34

Figure 4-6. Diagram showing the added effect of post-depositional elevation changes within the rock avalanche deposit on ice changes that are not measured during DEM differencing in net positive deposit areas. The actual thickness of the deposit (h_{true}) is measured by subtracting (h_3) from the sum of h_1 , h_2 , and the change in elevation within the deposit between t_e and t_f (h_4). 35

Figure 4-7. Diagram showing the added effect of post-depositional elevation changes within the rock avalanche deposit on ice changes that are not measured during DEM differencing in net negative deposit areas. The actual thickness of entrained material ($h_{entrained}$) is measured by subtracting the sum of h_{1n} and the change in elevation within the deposit between t_e and t_f (h_{4n}) from the sum of h_{2n} , h_{fill} , and h_{3n} 36

Figure 5-1. Elevation difference in Control Areas 4-6 between 6/15/2016 and 7/16/2016..... 42

Figure 5-2. Elevation difference between pre- (6/15/2016) and post-event (7/16/2016) DEMs over the Lamplugh rock avalanche deposit. Dashed line indicates extent of source area, which is obscured by clouds in the image acquired on 7/16/2016..... 43

Figure 5-3. Elevation difference between pre- (6/15/2016 and SDMI 5-meter) and post-event (9/27/2016) DEMs in the source area of the Lamplugh rock avalanche. 45

Figure 5-4. Differenced DEMs between a) 7/16/2016-8/27/2016 and b) 8/27/2016-9/28/2016 showing post-event changes within the Lamplugh rock avalanche deposit and on the adjacent glacial surface..... 46

Figure 5-5. Adjusted elevation difference between pre- and post-event DEMs over the Lamplugh rock avalanche. Data in the source area are from a 5-meter resolution SDMI DEM (pre-event) and an ASP-generated DEM from 9/27/2016 (post-event). Data within the remainder of the deposit are derived from ASP DEMs from 6/15/2016 (pre-event) and 7/16/2016 (post-event). 50

Figure 5-6. Zones of the Lamplugh rock avalanche delineated based on areas of accumulation and depletion identified in the adjusted differenced DEM between 6/15/2016 and 7/16/2016 (Figure 5-5). 52

Figure 5-7. Generalized representations of structures and surficial features (1:48,000 scale) mapped on a Digital Globe, Inc. image (7/16/2016) of the Lamplugh rock avalanche. 56

Figure 5-8. Strike-slip movement along the distal margin of the Lamplugh rock avalanche deposit exemplified in a) Digital Globe, Inc. imagery from 7/16/2016 and b) adjusted differenced DEM between 6/15/2016 and 7/16/2016 (Figure 5-5).....	58
Figure 5-9. Digital Globe, Inc. image taken on 7/16/2016 showing transverse ridges in the toe of the Lamplugh rock avalanche.	60
Figure 5-10. Example of fensters identified in a) Digital Globe, Inc. imagery from 7/16/2016 and b) adjusted differenced DEM between 6/15/2016 and 7/16/2016 (Figure 5-5). Profile a-a' was derived from the post-event (7/16/2016) DEM.	61
Figure 5-11. Digital Globe, Inc. imagery from 7/16/2016 showing locations of run-up along the west lateral margin of the Lamplugh rock avalanche.....	62
Figure 6-1. Differenced cross-sections taken along a transverse profile through the deposit toe between 6/15/2016-7/16/2016 and 6/15/2016-8/27/2016. An increase in observed thickness ($\Delta = 2.7$ meters) with an increase in time between observations demonstrates differential melting between deposit-covered areas and the adjacent surface.	66
Figure 6-2. Normalized differenced cross-sections through the toes of the Lamplugh and West Salt Creek rock avalanches show a difference in relief between the distal rim and more proximal areas of the deposit.	73
Figure 6-3. Plots of L_{max} versus L for a) rock avalanches travelling over rock/soil and ice and b) confined and unconfined rock avalanches.	76
Figure A-1. Elevation difference in Control Areas 4-6 between 7/16/2016 and 8/27/2016.....	91
Figure A-2. Elevation difference in Control Areas 4-6 between 8/27/2016 and 9/28/2016.....	91
Figure A-3. Elevation difference in Control Areas 1-3 between SDMI 5m- and 9/27/2016.....	92
Figure A-4. Elevation difference in Control Areas 1-3 between 6/15/2016- and 9/27/2016.....	92
Figure B-1. Digital Globe, Inc. image of the Lamplugh rock avalanche on 7/16/2016 that was used for mapping of structures and surficial features.....	93
Figure C-1. Pre- and post-event elevation profiles along A-A' showing the location of Zones A-F. Pre-event elevation data is derived from a 5-meter resolution SDMI DEM (source area only) and the ASP-generated DEM from 6/15/2016. Post-event elevation data is derived from DEMs from 9/27/16 (source area only) and 7/16/2016.....	94

LIST OF TABLES

Table 2-1. Characteristics of previously documented rock avalanches travelling on ice, with areas larger than 1 km ² , in Glacier Bay National Park and Preserve.....	13
Table 4-1. Panchromatic and multispectral sensor resolution and geolocation accuracy of WorldView-1, 2, and 3 satellites (DigitalGlobe, Inc. 2016b, 2016c, 2016d).	16
Table 4-2. Horizontal (CE90) and vertical (LE90) geolocation accuracy of WorldView-1, 2, and 3 satellites (DigitalGlobe, 2016a, 2016d).	17
Table 4-3. Dates of pre- and post-event Digital Globe, Inc. imagery acquired for DEM generation and mapping of the Lamplugh rock avalanche.	18
Table 4-4. Average slope of each control area used to assess the accuracy of differenced DEMs over the Lamplugh rock avalanche.....	24
Table 4-5. Dates and uses of differenced DEMs for analysis of the Lamplugh rock avalanche. .	27
Table 5-1. Mean triangulation error in the north-south (Band 1), east-west (Band 2), and vertical (Band 3) directions for each DEM produced in ASP.	40
Table 5-2. Results of the chi-square goodness-of-fit test, mean, IQR, standard deviation, and relative vertical accuracy of elevation difference in control areas between DEM pairs used for differencing analyses.....	41
Table 5-3. Elevation changes on the Lamplugh rock avalanche deposit and adjacent surfaces measured as average total change and average daily rate of change between specified dates in June (pre-event), July, August, and September, 2016. Changes in elevation are measured on A) the glacier surface adjacent to areas of the deposit with a net positive volume, B) areas of the deposit with a net positive volume, C) the surface adjacent to areas of the deposit with a net negative volume, and D) areas of the deposit with a net negative volume.	44
Table 5-4. Measured and estimated parameters used in Equations 4-5 and 4-6 to calculate elevation adjustments for differences in elevation between 6/15/2016 and 7/16/2016 in the area of the Lamplugh rock avalanche deposit. Since h_2 and h_{2n} are measured from the changes in elevation in the deposit area between 6/15/2016 and 7/16/2016, these values are unique for each pixel of the differenced DEM (Figure 5-2) and are not reported here (i.e., N/A entries).....	47
Table 5-5. Deposit volumes and average thicknesses for each zone of the Lamplugh rock avalanche.....	54
Table 5-6. Longitudinal locations of the center of mass for the entire Lamplugh rock avalanche deposit and for only the east (unconfined) and west (confined) halves of the deposit.....	54

Table 6-1. Estimated snow and ice changes compared to the average elevation change observed on the glacier surface between 6/15/2016-7/16/2016, 7/16/2016-8/27/2016, and 8/27/2016-9/28/2016.	64
Table 6-2. Values of apparent and adjusted deposit volume and average thickness for each zone of the Lamplugh rock avalanche. Please refer to Figure 5-6 for zone delineation.	68
Table 6-3. Center of mass locations for rock avalanches travelling over rock/soil and ice and in confined and unconfined topographic settings.	75

ACKNOWLEDGMENTS

The U.S. Geological Survey provided funding and the opportunity for this research. I would like to acknowledge my committee member, Jeffrey Coe, from the U.S. Geological Survey for helping me develop the vision for this research and for providing guidance throughout the project. I would also like to express my appreciation for my advisor, Dr. Wendy Zhou, and my committee member, Dr. Paul Santi, who provided suggestions and insight throughout the project. I would like to acknowledge the Department of Geology and Geological Engineering for providing funding throughout my graduate study. Finally, I would like to thank my peers in the Department of Geology and Geological Engineering and my colleagues at the U.S. Geological Survey for comments and advice throughout my research.

CHAPTER 1 INTRODUCTION

Slope instabilities are common in mountainous terrain and increasing development in these areas necessitates hazard analyses. Mass wasting of mountainous terrain in polar regions can be particularly complex because of interactions with glacial ice (Korup & Dunning, 2015) and the presence of alpine permafrost (Evans & Delaney, 2014). Catastrophic slope failures are particularly common in areas of Alaska, British Columbia, the European Alps, the Russian Caucasus, and the New Zealand Alps. Types of mass wasting in alpine areas include glacier avalanches, rock falls, debris flows, landslides in rock and soil, rock slides, and rock avalanches (Evans & Clague, 1994; Geertsema et al., 2006; Geertsema & Cruden, 2008). This research will focus on rock avalanches sourced from periglacial rock slopes that travel over ice. This type of mass movement (also commonly referred to as rock-ice avalanches) is characterized as a large volume, highly mobile failure that involves rapid, flow-like movement of rock and ice (Deline et al., 2015; Evans & Delaney, 2015). Rock-ice avalanches have the potential to be extremely catastrophic, with estimates of volumes greater than 10^9 m^3 and velocities in excess of 100 m/s (Pudasaini & Krautblatter, 2014). Significant hazards can arise when rock-ice avalanches occur in populated mountain areas or when deposits travel significant distances from the location of failure into developed areas. Secondary effects of rock avalanches, including tsunamis (Wieczorek et al., 2007), breached landslide dams (Korup & Dunning, 2015), and rapidly induced glacial advances (Hewitt, 2009) can also cause significant hazards.

Several notable factors contribute to an inadequate understanding of rock avalanche processes in glaciated environments. The infrequent occurrence and typically remote locations of rock-ice avalanches make direct detection and observation difficult. Recognition is further hindered by glacial processes and snow cover, which limit the preservation of characteristically

thin deposits (Deline et al., 2015). Additionally, misclassification of rock-avalanche deposits as moraines has caused an under representation of documented historic events (Deline et al., 2015). Many well studied rock avalanches on glaciers have been triggered by earthquakes, including the 1964 Alaska Earthquake (McSaveney, 1978; Post, 1967) and the 2002 Denali Fault earthquake (Jibson et al., 2006). Recent documentation of rock-avalanche events unprecedented in frequency and magnitude has drawn attention to climate change as an additional driving factor (e.g. Geertsema et al., 2006; Gruber & Haeberli, 2007; Huggel et al., 2012). Glacial debuttressing and permafrost degradation have been causally linked to failures, however these processes are poorly understood and the exact mechanisms of individual failures remain ambiguous. The potential effect of increasing temperatures on slope stability in mountainous regions is especially relevant in light of recent warming trends and future climate predictions. Projections for temperature increases by 2055 in mid- and high-latitude alpine environments range from 3-4°C and 4-7°C, respectively (Krautblatter et al., 2012). Changes of this magnitude could have significant effects on the processes involved in rock-ice avalanche failures.

Landslide-hazard assessments rely on an accurate understanding of movement dynamics. The relationships between volume, area, and travel distance are particularly critical to assess the hazard potential of long-runout events (Legros, 2002). The complex and highly variable behavior of rock avalanches on glaciers corroborates the difficulty of predicting these geometric parameters. Both empirical correlations (Evans & Clague, 1999; Schneider et al., 2011a) and numerical models (Bottino et al., 2002) suggest that the travel distance of rock avalanches travelling over ice exceeds that of rock avalanches travelling over other substrates. Several mechanisms exist to explain these observations, including: 1) the surface friction of ice is lower than that of rock or soil and 2) melting of entrained snow and ice increases the fluidity of debris

(Evans & Clague, 1999). Although empirical correlations and modeling have been shown to support this hypothesis, contradictory cases have also been cited. It has been shown that some rock-ice avalanches of similar volume have differing amounts of mobility (Evans & Clague, 1999) and that the mobility of some rock-ice avalanches travelling over glaciers have mobility values closer to those that would be expected from travel over soil or rock (Schneider et al., 2011a). These findings suggest that other unknown factors may also play a role in controlling the travel distance of rock-ice avalanches. Research involving both empirical relationships and numerical models has identified volume, topography, flow rheology (ice and water content), and frictional characteristics of the surface as the most significant factors influencing the emplacement of rock-ice avalanches (Pudasaini & Krautblatter, 2014; Rosio et al., 2012; Schneider et al., 2011).

Volume estimations for rock-ice avalanches are difficult to obtain and routinely lack both accuracy and precision (Korup & Dunning, 2015; Schneider et al., 2011a). Many available literature values are crude estimates, made either based on deposit area and reported average thickness or by assuming that the relationship between volume and area is comparable to that of other similarly sized events (Sosio et al., 2012). Acquisition of high-resolution pre- and post-event topography data has been used to calculate volumes of other types of mass movements (e.g. Coe et al., 1997; Tsutsui et al., 2007) and could greatly improve rock-ice avalanche volume estimates.

Topography is also an important factor controlling the travel distance and path of rock-ice avalanches. Because rock-ice avalanche deposits are typically thin, topographic control is more significant than it is for rock avalanches travelling over rock or soil (Rosio et al., 2012). The effects of micro-topographic variations (1-10 m) may have a more significant role in

controlling the mobility of flows over generally low gradient, smooth glacial surfaces compared to steep surfaces with variations in topography and surface roughness (Rosio et al., 2012; Schneider et al., 2011a).

Flow rheology and frictional characteristics of the sliding surface are harder to quantify than volume and topography and are significantly more difficult to study remotely. However, morphological features within landslide deposits reflect physical flow processes, which are directly affected by rheology and surface characteristics. Identification of structural features in both rock-avalanches on glaciers (e.g. Delaney & Evans, 2014; Dufresne and Davies, 2009; McSavaney, 1978) and on rock and soil (e.g. Coe et al., 2016; Dufresne et al., 2016) have been used to interpret the dynamics of mass movements.

Alaska has a rich history of rock-ice avalanches and during the past five years the occurrence of several large events in GBNP has drawn attention to this area. Most recently, the Lamplugh rock-ice avalanche occurred on June 28, 2016 (Petley, 2016) and is the largest event on record in GBNP (Bessette-Kirton & Coe, 2016; Post, 1967). The recent occurrence and exceptional size of this event make it an excellent candidate for a case study of the factors influencing rock-ice avalanche emplacement as a means of informing hazard assessments both within GBNP and in other glaciated regions. Additionally, the availability of high-resolution pre- and post-event imagery of the Lamplugh rock avalanche provides a platform through which the feasibility of using remotely sensed data to measure the volume of rock avalanches in remote areas can be assessed.

CHAPTER 2 BACKGROUND

2.1 Prior Work

This section describes a previous study on rock avalanches in GBNP and a number of other prior works that studied the morphology and dynamics of rock avalanches travelling over both ice and rock and soil.

2.1.1 Inventory of Rock Avalanches in Glacier Bay National Park and Preserve

This thesis is part of a larger a study by Bessette-Kirton and Coe (2016) which examines changes in frequency, magnitude, and mobility of rock avalanche events in GBNP since 1984. Landsat imagery (30-meter resolution) was used to create an inventory of rock avalanches in a 5000 km² area of GBNP. Landsat images were used to identify and map 24 rock avalanches that occurred between 1984 and 2016. For each mapped rock avalanche the following parameters were recorded: date, or range in possible dates of occurrence, the total area covered by the rock avalanche (including the source area, travel path, and deposit), the maximum travel distance measured along a curvilinear centerline (L), and the maximum change in elevation between the start and end points of the centerline (H) (Bessette-Kirton & Coe, 2016).

Coe et al. (2017) conducted further analysis of the GBNP rock avalanche inventory and found that three main clusters of rock avalanches occurred during the period of study, the last of which began in June 2012 and includes four of the five largest rock avalanches in the inventory. An evaluation of rock avalanche characteristics shows that during the 33-year period of record, the magnitude (area) and mobility (as measured by H/L) of recorded rock avalanches increased (Coe et al., 2017). A slight increase in the recurrence interval of rock avalanches was also observed (Coe et al., 2017). This analysis in conjunction with the finding that the long-term trend

in mean annual maximum air temperature exceeded 0° C in 2010, shortly before the start of the third cluster of large rock avalanches, indicates that temperature-related permafrost degradation may be related to the increasing size and occurrence of failures (Coe et al., 2017).

The inventory by Bessette-Kirton and Coe (2016) includes preliminary mapping of the Lamplugh rock avalanche. The Lamplugh rock avalanche occurred on June 28, 2016 and was recorded as a M=2.9 seismic event in the Alaska Earthquake Center catalog (Petley, 2016). In comparison to the other 23 events identified in the inventory of GBNP, The Lamplugh rock avalanche has the largest area (>2.5 times greater than the next largest) and is tied for the highest mobility (with a Height/Length=0.15). The geometric parameters obtained from 30-meter resolution Landsat imagery could be refined with higher-resolution imagery.

2.1.2 Morphologies and Structures of Rock-Avalanche Deposits

Identification and analysis of depositional morphology, including overall geometries and the presence of relatively small structures, can provide insight into the sequence and characteristics of rock avalanche emplacement. This type of investigation is particularly important to rock avalanche studies since failures are rarely witnessed. Observations of morphologic and structural features in rock avalanche deposits have been recognized as important indicators of movement since the first published account of a rock avalanche, in which Heim described the 1881 Elm rock avalanche in Switzerland (as cited in Hsü, 1978). However, with a few exceptions, the majority of studies on deposit structures and surficial features rely on qualitative observations and localized measurements to draw conclusions about the overall mechanisms of emplacement. Additionally, the absence of sufficiently detailed pre- and post-event topography data for the majority of rock avalanche studies does not allow for a detailed

understanding of observations presented in the literature. The combination of field observations and detailed topographic data has the potential to provide valuable insight into rock avalanche emplacement processes.

Conceptual models have been used to describe rock avalanche deposit geometry as a basis for comparison with field data and observations. The deposit geometry of a simple or classic rock avalanche was described by Hewitt et al. (2008) as “an extensive thin sheet, rarely more than 2 to 10 m thick and lobate in plan... [which] varies little in thickness and has minor surface relief, commonly with a slight ridge at the distal rim.” This geometry has been demonstrated experimentally (Friedmann et al., 2006) and in numerical models (Legros, 2002), but is rarely seen in nature because of topographic confinement (Hewitt et al., 2008) and interaction with or entrainment of substrate material (Dufresne, 2016; Hungr & Evans 2004). Additional thickness distribution models that have been corroborated by field observations vary based on the degree of confinement (Legros, 2002) and the type or progression of movement (Strom, 2006). The main types of thickness distributions identified in these models are: 1) a linear decrease in thickness with distance (Legros, 2002), 2) minimal variation in thickness with distance (Legros, 2002), and 3) a thin deposit at the proximal end with an increasing accumulation of material towards the distal end (Strom, 2006). The thickness distribution models presented in the literature do not address rock avalanches travelling over ice. Limited field observations indicate that the average thickness of rock avalanches emplaced on glaciers is an order of magnitude less than that of rock avalanches travelling over rock and soil, (e.g. Jibson et al., 2006; McSaveney, 1978) with typical average thicknesses ranging from 0.5 to 5 meters (Deline et al., 2015).

Observations of deposit structures and surficial features have been used to make interpretations about the mechanisms of rock avalanche emplacement in both prehistoric events (Dufresne et al., 2016; Eppler et al., 1987; Evans et al., 1994; Mudge, 1965) and modern rock avalanches travelling both over rock or soil (Hadley, 1978; Johnson, 1978; Marangunic & Bull, 1966; McSaveney, 1978; Shreve, 1966; Shreve, 1968) and ice (Cox and Allen, 2009; Delaney and Evans, 2014; Fahnestock, 1978; Jibson et al., 2006; Jiskoot, 2011; Lipovsky et al., 2008; McSaveney, 2002; Shugar and Clague, 2011). With the exception of a handful of studies (e.g. Tschirgant, Austria (Dufresne et al., 2016); Sherman Glacier, Alaska (Marangunic & Bull, 1966; McSaveney, 1978; Shreve, 1966); and West Salt Creek, Colorado (Coe et al., 2016)), detailed mapping of morphological and structural features in rock avalanche deposits has not been widely reported.

The most commonly recognized structures in rock avalanche deposits are sets of transverse and longitudinal ridges and furrows. Descriptions of transverse ridges (Jibson et al., 2006; Jiskoot, 2011; Johnson, 1978; McSaveney, 2002; Shugar and Clague, 2011) indicate a mechanism of compression and associated flow deceleration. Eppler et al. (1987) and McSaveney (1978) specifically identified sets of transverse ridges and troughs as surface folds rather than flow fronts or imbricate thrust sheets. Longitudinal flow features (Cox & Allen, 2009; Delaney & Evans, 2014; Hadley, 1978; Jibson et al., 2006; Jiskoot, 2011; Johnson, 1978; Marangunic & Bull, 1966; McSaveney, 1978; McSaveney, 2002; Mudge, 1965; Shreve, 1966; Shugar and Clague, 2011) are generally interpreted to indicate shearing and Eppler et al. (1987) specifically identified longitudinal ridges as strike-slip faults with measurable offset. Dufresne and Davies (2009) differentiated between longitudinal or elongate ridges and flowbands in rock avalanches travelling over different substrates. Longitudinal ridges are described as forming in

rock avalanches travelling over rock or soil and having relief of tens of meters above the remainder of the deposit. Flowbands are formed in rock avalanches deposited on glaciers and have a much lower relief, but are significantly more elongate and often extend along the entire length of flow.

Other significant features that have been widely reported in studies of rock avalanches are lateral and distal ridges or rims. However, many of the descriptions available in the literature are purely qualitative and do not provide absolute elevation offsets between the ridges or rims, and either the surrounding surface or the remainder of the deposit. Ambiguous descriptions and a general lack of quantification make it difficult to understand the true magnitude of the features described.

Lateral ridges and distal rims have been specifically identified in deposits of rock avalanches emplaced on glaciers. Lateral and distal rims and ridges in the Sherman Glacier rock avalanche deposit were described by Shreve (1966) as 3-15 meters high and 15-150 meters wide with hummocky topography and imbricate structures. Conversely, Marangunic and Bull (1966) described variability in the presence of a narrow rim at the distal edge of the Sherman Glacier rock avalanche deposit and indicated that there was no evidence for imbricate structures. The presence of “imbricate thrust sheets” forming a raised rim has also been described in the Mount Cook, New Zealand rock avalanche (McSaveney, 2002).

Descriptions of three rock avalanches on the Black Rapids Glacier that were triggered in 2002 by the Denali Fault earthquake are characterized to be uniformly thin (2-3 meters) with a thick distal rim composed of large blocks (Shugar & Clague, 2011). Conversely, Jibson et al. (2006) described the Black Rapids rock avalanches as uniform deposits (~3 meters) with sharply defined margins with an average height of 2-3 meters, giving no indication of a change in

thickness between the body and edge of the deposits. The presence of thicker (3-15 meters) deposits is noted on two avalanches on the nearby West Fork Glacier in areas where large blocks are present and sharp steep margins are noted, but no further distinctions regarding differential deposit thickness between the distal edge and middle of the deposit are made (Jibson et al., 2006). Although lateral and distal rims have been identified in deposits of rock-ice avalanches, ambiguity and a lack of detailed data cause some uncertainty in the size and extent of the described features.

2.2 Study Area and the Lamplugh Rock Avalanche

The Lamplugh rock avalanche is located on the western peninsula of GBNP in southeast Alaska (Figure 2-1). GBNP has a maritime climate, which in combination with mountainous terrain contributes to high annual precipitation rates in the form of rain and snow (Loso et al., 2011). Melting of the Glacier Bay Icefield, which reached a maximum thickness of 1.5 km during the Little Ice Age (LIA) formed Glacier Bay proper (Connor et al., 2009). Changes to the glacial landscape in this region are rapid, with accumulations of up to four meters water equivalent (weq) per year and ablation rates of as much as 14 meters weq per year (Larsen et al., 2007). Post-LIA isostatic rebound as a result of deglaciation contributes to uplift rates of ~30 mm/year in Glacier Bay (Larsen et al., 2005). The Fairweather Fault runs approximately north-south through the western peninsula of GBNP and accommodates slip along the transform boundary between the Pacific and North American Plates, further contributing to dynamic landscape processes (Plafker et al., 1978).

Paraglacial landscapes resulting from the geologic and climatological setting of GBNP are prone to processes that contribute to rock slope destabilization. Glacier oversteepening resulting

from uplift and erosion can increase rock slope stress and lead to slope instability (Deline et al., 2015). Additionally, glacial debutressing acts to remove lateral support at the base of slopes and the removal of glacial ice can cause fracturing as a result of stress-release (Deline et al., 2015).

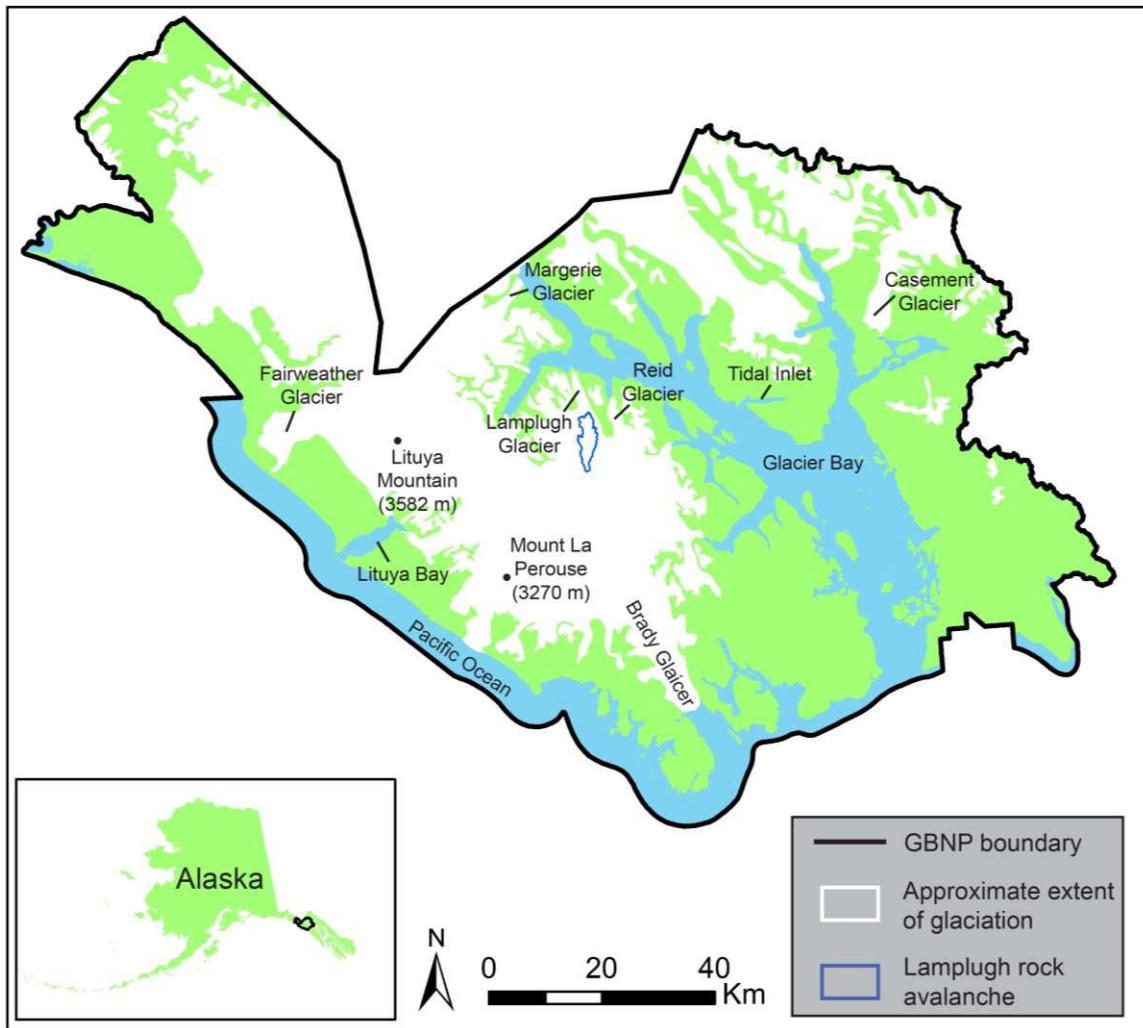


Figure 2-1. Map of Glacier Bay National Park and Preserve showing the location of the Lamplugh rock avalanche (Alaska Department of Natural Resources, Information Resource Management, 1998a, 1998b; National Park Service, 2014)

With the exception of the previously described recent work by Bessette-Kirton and Coe (2016), documentation of rock avalanches in GBNP has historically been sparse. Table 2-1 summarizes the date, approximate location, and area of previously documented rock avalanches with areas greater than 1 km² in GBNP. Rock avalanches with deposits ranging in area from 2-

8.5 km² on the Casement, Johns Hopkins, Margerie, and Fairweather Glaciers (Figure 2-1) were recorded between 1945 and 1968 (Post, 1967). Older undated deposits have also been recorded on the Casement and Margerie Glaciers. Recent rock avalanches on Lituya Mountain (2012) and Mount La Perouse (2014), both of which were detected seismically, have attracted the attention of researchers because of their unprecedented magnitude in comparison to prior events in this area (Geertsema, 2012; Petley, 2014). In 1958 a seismically triggered rock avalanche caused a tsunami in Lituya Bay (Figure 2-1) that travelled 524 meters up the opposite shore (Wieczorek et al., 2007). More recently, monitoring and assessment of a large, slowly moving rock mass along the shore of Tidal Inlet (Figure 2-1) has identified the catastrophic potential of a tsunami induced by a rapid failure of rock (Wieczorek et al., 2007). Although both of these cases are located in unglaciated regions of GBNP, similar hazards could also arise on glaciated rock slopes.

The Lamplugh rock avalanche originated from a bedrock ridge at an elevation of approximately 2,150 m a.s.l. and travelled a total of ~10,500 meters, about 6,700 meters of which was on the glacial valley floor. As shown schematically in Figure 2-2, the north-facing ridge drops steeply to an elevation of approximately 900 m a.s.l. before sloping more gently toward the transition to the glacier surface, which is located at approximately 700 m a.s.l. The average gradient of the valley floor of the Lamplugh Glacier along the profile shown in Figure 2-2 is approximately 1.3 degrees. The west side of the travel path along the Lamplugh Glacier is confined by mountains, while the east side is an unconfined valley. The distal margin of the Lamplugh rock avalanche lies approximately 8,600 meters from the terminus of the Lamplugh Glacier, which feeds into Glacier Bay. The source area consists of sedimentary and metamorphic rocks of the Triassic to Cretaceous Kelp Bay Group, including phyllite, quartzite, greenschist, greenstone, greywacke, and greywacke semischist (Wilson et al., 2015). The Lamplugh Glacier

Table 2-1. Characteristics of previously documented rock avalanches travelling on ice, with areas larger than 1 km², in Glacier Bay National Park and Preserve.

Date	Approximate Location	Area (km ²)	Source
1945?	Casement Glacier	3	Post, 1967
1961?	Johns Hopkins Glacier	2	Post, 1967
1961	Margerie Glacier	2.5	Post, 1967
1965?	Fairweather Glacier	7.5	Post, 1967
Pre 9/7/84	Mount Sabine	1.7	Bessette-Kirton & Coe, 2016
5/21/85-6/22/85	Fairweather Glacier	3.7	Bessette-Kirton & Coe, 2016
10/12/85-6/25/86	Mount Sabine	1.4	Bessette-Kirton & Coe, 2016
6/15/94-8/11/94	Mount Crillon	1.5	Bessette-Kirton & Coe, 2016
8/2/14-5/1/15	Mount Wilbur	3.6	Bessette-Kirton & Coe, 2016
5/24/15-7/4/15	South Crillon Glacier	1.3	Bessette-Kirton & Coe, 2016
6/11/2012	Lituya Mountain	7.9	Bessette-Kirton & Coe, 2016; Geertsema, 2012
2/16/2014	Mount La Perouse	5.5	Bessette-Kirton & Coe, 2016; Petley, February 25, 2014
6/28/2016	Lamplugh Glacier	22.2	this research

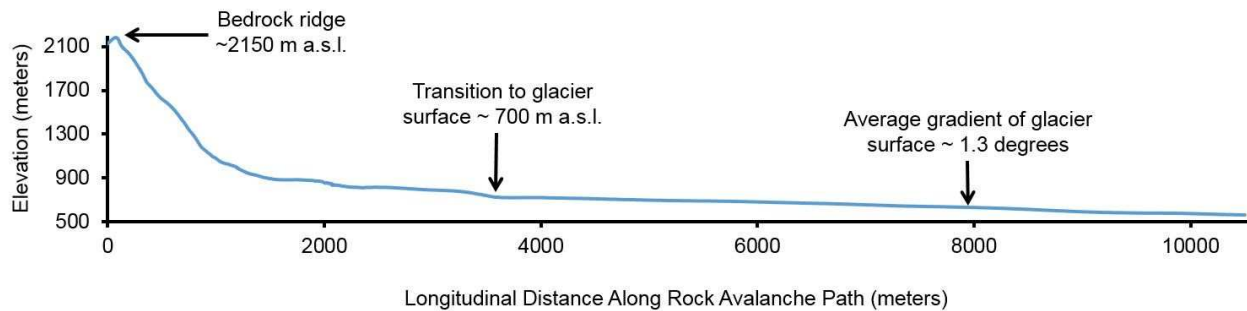


Figure 2-2. Profile of pre-event topography along the travel path of the Lamplugh rock avalanche.

originates from a flow divide at 750 m a.s.l that is shared by the Brady and Reid Glaciers, and flows north toward Glacier Bay (Loso et al., 2011). Mass balance measurements between 1995-

2011 show that the Lamplugh Glacier consistently lost mass throughout the period, with a maximum loss rate of 0.54 meters per year between 2000 and 2005 (Loso et al., 2011).

CHAPTER 3 PURPOSE

The purpose of this research is to study the emplacement mechanisms of rock avalanches travelling over ice through a case study of the Lamplugh rock avalanche in GBNP. This research will specifically focus on the volume and distribution of material within the deposit, and structures and surficial features. Data used for this research are limited to that which can be obtained from satellite imagery. The main objectives of this research are to:

1. Demonstrate the capacity to use high-resolution satellite imagery to study rock avalanches travelling over glaciers and develop a framework for improved volume estimates and remote identification of characteristics indicative of emplacement processes.
2. Establish interpretations of emplacement dynamics through an integrated examination of volume and thickness distribution, landslide structures, and surficial features.

The following sections describe the methodologies and results relevant to each of these objectives.

CHAPTER 4 METHODS

4.1 WorldView Imagery

The WorldView-1, 2, and 3 satellites are part of the Digital Globe, Inc. constellation and have been collecting high-resolution imagery since 2007, 2009, and 2014, respectively (DigitalGlobe, Inc., 2016b, 2016c, 2016d). The satellites in the Digital Globe constellation collect imagery in the visible light spectrum from both panchromatic and multispectral sensors. As shown in Table 4-1, there is some variation in the resolution between both sensors and specific satellites, although overall the resolution is strikingly better than many other satellites (e.g. Landsat). The panchromatic and multispectral band resolutions listed in Table 4-1 indicate the Ground Sample Distance (GSD) at 20 degrees off-nadir. This value is listed instead of the slightly better GSD at-nadir resolution because all of the imagery used in this research pertains to the former.

Table 4-1. Panchromatic and multispectral sensor resolution and geolocation accuracy of WorldView-1, 2, and 3 satellites (DigitalGlobe, Inc. 2016b, 2016c, 2016d).

Satellite	Panchromatic Band Resolution (GSD at 20° off-nadir)	Multispectral Band Resolution (GSD at 20° off-nadir)
WorldView-1	0.55 m	n/a
WorldView-2	0.52 m	2.07 m
WorldView-3	0.34 m	1.38 m

In addition to traditional imagery collection, the Digital Globe constellation has the capability to collect stereo pairs from the same orbit with a time delay of approximately 60-90 seconds (Shean et al., 2016). This research will use Basic Level 1B (radiometrically and sensor-corrected) and Ortho Ready Standard (radiometrically and sensor-corrected and georectified) stereo products from WorldView-1, 2, and 3. All quantitative analyses will utilize Level 1B

imagery, and therefore only the accuracy of this type of imagery will be discussed further. The horizontal and vertical geolocation accuracies of Digital Globe products are measured as circular error at the 90th percentile (CE90) and linear error at the 90th percentile (LE90), respectively (DigitalGlobe, Inc. 2016a). These metrics indicate that at a minimum, 90 percent of the points measured have a horizontal or vertical error less than the specified CE90 or LE90 value (DigitalGlobe, Inc. 2016a). The horizontal and vertical geolocation accuracies of WorldView Basic Stereo products, without the use of ground control, are listed in Table 4-2. It should be noted that documentation of an accuracy analysis for WorldView-3 products has not yet been released, therefore the value of CE90 listed is considered an estimate (DigitalGlobe, Inc. 2016d).

Table 4-2. Horizontal (CE90) and vertical (LE90) geolocation accuracy of WorldView-1, 2, and 3 satellites (DigitalGlobe, 2016a, 2016d).

Satellite	Horizontal Geolocation Accuracy (CE90)	Vertical Geolocation Accuracy (LE90)
WorldView-1	4.0 m	3.7 m
WorldView-2	3.5 m	3.6 m
WorldView-3	3.5 m	n/a

4.1.1 Acquired Imagery

Between June 2015 and November 2016, thirty WorldView stereo pairs were collected in the area of the Lamplugh rock avalanche. Many of these images are obscured by the presence of cloud cover and limited daylight during winter months. Eleven images with minimal cloud cover and reasonable image quality (Table 4-3) were acquired for processing. As noted in Table 4-3, portions of some images are covered in clouds or obscured by shadows and in nearly all cases, the full extent of the rock avalanche source area is not included in both stereo images.

Table 4-3. Dates of pre- and post-event Digital Globe, Inc. imagery acquired for DEM generation and mapping of the Lamplugh rock avalanche.

Collection Date	Pre/post-event	WorldView Satellite	Stereo pairs used for DEM generation	Image (type) used for scarp delineation and/or deposit mapping	Notes
<i>6/19/2015</i>	pre	2	No	Scarp delineation (pan-sharpened multi-spectral)	Parts of scarp and deposit areas are covered by clouds; incomplete coverage of study area in stereo pairs;
<i>8/01/2015</i>	pre	1	Yes	Scarp delineation (panchromatic)	
<i>10/02/2015</i>	pre	1	No	Scarp delineation	Scarp area is shadowed.
<i>6/15/2016</i>	pre	1	Yes	Scarp delineation (panchromatic)	
<i>7/09/2016</i>	post	3	No	Scarp delineation (pan-sharpened multi-spectral)	Scarp area and parts of the deposit area are covered in clouds; incomplete coverage of scarp in stereo pairs.
<i>7/16/2016</i>	post	3	Yes	Scarp delineation and deposit mapping (pan-sharpened multi-spectral)	Scarp area is covered by clouds; incomplete coverage of scarp in stereo pairs.
<i>8/20/2016</i>	post	1	No	Scarp delineation (panchromatic)	Clouds over toe of deposit; scarp area is shadowed. Note: the control areas used for accuracy analysis are also covered by clouds so quality of DEM could not be assessed.
<i>8/27/2016</i>	post	2	Yes	Scarp delineation (pan-sharpened multi-spectral)	Thin clouds over deposit area; scarp area is shadowed.
<i>9/27/2016</i>	post	1	Yes (scarp area only)	Scarp delineation and deposit (scarp only) mapping (panchromatic)	Image is significantly shadowed over deposit area; scarp area is clear of clouds, but shadowed; scarp area is covered in snow.
<i>9/28/2016</i>	post	3	Yes	Scarp delineation (pan-sharpened multi-spectral)	Image is shadowed in scarp area; scarp area is covered in snow; incomplete coverage of scarp in stereo pairs.
<i>10/29/2016</i>	post	3	No	Scarp delineation and deposit (scarp only) mapping (pan-sharpened multi-spectral; scarp area only)	Image is shadowed in scarp area and over deposit; deposit is covered in snow; incomplete coverage of scarp in stereo pairs.

4.2 Elevation Datasets

Existing elevation data for the study area includes a 30-meter resolution DEM collected from the Shuttle Radar Topography Mission (SRTM) (U.S. Geological Survey et al., 2000) and a 5-meter resolution DEM collected through the Alaska Statewide Digital Mapping Initiative (SDMI) (Dewberry, 2013; U.S. Geological Survey, 2012). The SRTM DEM was collected in February 2000 and vertical accuracy in the Glacier Bay area is estimated to be ± 5 meters (Larsen et al., 2007). The SDMI 5-meter DEM was collected between August and September, 2012 and was created using Interferometric Synthetic Aperture Radar (IFSAR). The vertical accuracy of the SDMI DEM is 1.5 meters in areas with slopes ranging from 0 to 10 degrees and 9.0 meters in areas with slopes ranging from 10-20 degrees (Dewberry, 2013).

4.3 Ames Stereo Pipeline Workflow

The NASA Ames Stereo Pipeline (ASP) is a semi-automated, open-source stereogrammetry software that is capable of generating DEMs from high-resolution satellite imagery (Beyer et al., 2016). ASP was originally created to process planetary imagery and has only recently been adapted for terrestrial use. The capability to process Digital Globe imagery was established to create models of ice and bare rock (Beyer et al., 2016) and functionality has only been fine-tuned for imagery of the Antarctic and Greenland ice sheets, with some test cases in Washington State and Alaska (Shean et al., 2016). ASP has functionality specific to WorldView-1, 2, and 3 images and was used to generate high-resolution (2m) DEMs from Level 1B products. ASP Version 2.5.3 was released on October 11, 2016 and was used for all processing. The generalized workflow used to generate DEMs in ASP consists of the following

steps: 1) image pre-processing and pre-alignment, 2) stereo correlation, and 3) raster conversion. Each processing step is discussed in detail in the following sections.

4.3.1 Pre-processing and Pre-alignment

Major sources of inaccuracy in WorldView imagery are sensor boundary artifacts, which are caused by slight offsets among all of the individual sensors within a single cluster of sensors, all of which are used to produce one complete image. ASP provides corrections for WorldView-1 and 2 images, which were applied to all applicable images during pre-processing. Artifact corrections for WorldView-3 imagery are not available in Version 2.5.3.

During pre-processing, individual image tiles from the same parent image can be mosaicked. This can reduce the number of scenes that need to be processed if more than one image tile is required to cover the study area. For most of the image sets listed in Table 4-3 the complete extent of the Lamplugh rock avalanche deposit was included in a single image tile. For the images in which this was not the case, image tiles were mosaicked prior to further processing.

Orthorectification to a coarse (~30-meter resolution) DEM was used to pre-align stereo images to reduce the amount of time needed to search for matching points in the source images during stereo correlation. This process improves the quality of results, especially in areas of steep terrain, and eliminates the need to use an alignment algorithm during stereo correlation (Beyer et al., 2016). All images were superimposed onto a 30-meter resolution SRTM DEM.

According to the ASP User Guide a bundle adjustment process, which adjusts camera positions and orientations to be self-consistent, is recommended during pre-processing unless co-registration with ground control points is performed during post-processing (Beyer et al., 2016).

Alternatively, Shean et al. (2016) assert that this step is not necessary for WorldView-1 and 2 images because the geolocation accuracy of these satellites typically results in low triangulation error during stereo correlation. The use of bundle adjustment is recommended for triangulation errors (see Section 4.3.2) greater than one meter (O. Alexandrov, personal communication, January 30, 2017). The use of bundle adjustment on WorldView-2 and 3 images in this research resulted in a misalignment between the point cloud generated during stereo correlation and the final DEM, and in some cases produced anomalously high or low elevation values. This discrepancy could be a result of a software bug (O. Alexandrov, personal communication, January 30, 2017) or could require additional processing adjustments, which were not pursued further. Although the use of bundle adjustment was successful for WorldView-1 imagery, the triangulation error for all DEMs was found to be reasonably close to one meter. To maintain consistency in processing, a bundle adjustment was not used to produce any of the DEMs used for analysis.

4.3.2 Stereo Correlation

Image matching and triangulation are used during stereo correlation to produce a point cloud of elevation values. Initially ASP builds a disparity map by computing the x and y offsets for each matched pixel in a set of stereo pairs. This disparity map is built using normalized cross-correlation with a search window of 21 x 21 pixels (Beyer et al., 2016). The initial disparity is a first approximation, which uses only integer values. Sub-pixel refinement is used to iteratively optimize the offset of each pixel using the integer value as an initial approximation. Several refinement algorithms are available in ASP. The use of an affine adaptive Bayesian expectation-maximization algorithm (subpixel-mode 2) produces the most accurate results, but is

significantly more time intensive (Shean et al., 2016). Subpixel-mode 2 is recommended for scientific analyses and can improve results in areas with steep topography (Shean et al., 2016). Subpixel-mode 2 was used to produce all DEMs in this research.

Before triangulation, the disparity map is automatically filtered to reduce the presence of artifacts in the point cloud. During triangulation the camera models associated with each stereo pair are used to calculate elevation values for each point by reconstructing a three-dimensional location in space through the intersection of rays from each camera (Beyer et al., 2016). Image matching can be poor or fail altogether in areas with limited texture or low contrast, or in areas that are highly distorted due to different image perspectives, which is often the case in steep areas. (Beyer et al., 2016). While the absence of tree cover and vegetation and the presence of rock and ice make the study area an ideal candidate for image processing in ASP, areas of steep topography or poor lighting due to shadows or cloud cover could nevertheless cause processing blunders.

Another source of inaccuracy specific to WorldView imagery is camera jitter, which results from slight inaccuracies in the position and orientation of sensors. Low frequency camera jitter can be corrected automatically in ASP by solving for adjustments in an individual image before performing stereo correlation. This process reduces the presence of horizontal banding and was implemented on a case by case basis to improve DEM quality. Although this step improved image quality in most cases, stripping artifacts are still apparent in some DEMs and in the future, fine-tuning of this parameter could further improve quality.

4.3.3 Raster Conversion

During post-processing the point cloud of elevation values created during stereo correlation is converted to a gridded DEM that can be used with a geographic information system (GIS) platform. The output resolution of the DEM is recommended to be at least three times coarser than that of the input image resolution (Beyer et al., 2016). Since Digital Globe panchromatic imagery has an input resolution of 0.5 meter, DEMs were produced with an output resolution of 2 meters. An automated filtering process was used to remove outliers larger than three times the value of the 75th percentile (Beyer et al., 2016). During triangulation, the distance between two theoretical photogrammetric rays at their closest intersection is recorded, and a map of intersection error values can be specified as an additional output during DEM generation. The intersection error can be used as a metric of relative accuracy or self-consistency, but is not representative of the absolute accuracy of a DEM (Beyer et al., 2016).

4.4 DEM Generation

One set of pre-event stereo pairs (6/15/2016) and three sets of post-event stereo pairs (7/16/2016, 8/27/2016, and 9/28/2016) were used to produce DEMs over the study area. In all of these images, the rock avalanche scarp area is covered in clouds, obscured by shadows, or does not appear in both stereo images, causing the source area to appear as a hole in the output DEMs. Improved coverage of the scarp area was identified in an additional post-event stereo pair from 9/27/2016. This set of images was used to produce a DEM over only the source area. Since the source area was not completely covered in the pre-event image acquired on 6/15/2016, a 5-meter resolution SDMI DEM was also used for pre-event coverage of the source area.

4.5 DEM Accuracy Analysis

Since vertical ground control is not available for the study area the relative accuracy of DEM pairs was assessed to establish a baseline from which to assess elevation changes between any two given dates. The relative accuracy of DEMs produced in ASP was assessed by determining the elevation difference between stable bedrock locations in each DEM pair. Six control areas located approximately 12 kilometers north of the study area (Figure 4-1) were chosen by identifying areas of bedrock that were assumed to be stable and were not covered by snow. Control Areas 4-6 are common to the four sets of images used to produce DEMs over the deposit area. Control Areas 1-3 were used to assess the elevation difference between the post-event DEM of the source area (9/27/2016), the pre-event DEM from 6/15/2016, and the SDMI DEM since Control Areas 4-6 are not located in the images collected on 9/27/2016. The average slope of each control area is listed in Table 4-4. With the exception of the source area, the average slope in the control areas exceeds the range of slopes observed within the Lamplugh rock avalanche. Since vertical accuracy of DEMs is a function of slope (Tsutsui et al., 2007), it is assumed that the level of accuracy determined in the control areas will be the upper limit of elevation accuracy in the Lamplugh rock avalanche deposit.

Table 4-4. Average slope of each control area used to assess the accuracy of differenced DEMs over the Lamplugh rock avalanche.

Control Area	Average Slope
1	40.4 degrees
2	40.1 degrees
3	32.0 degrees
4	32.5 degrees
5	23.1 degrees
6	23.3 degrees

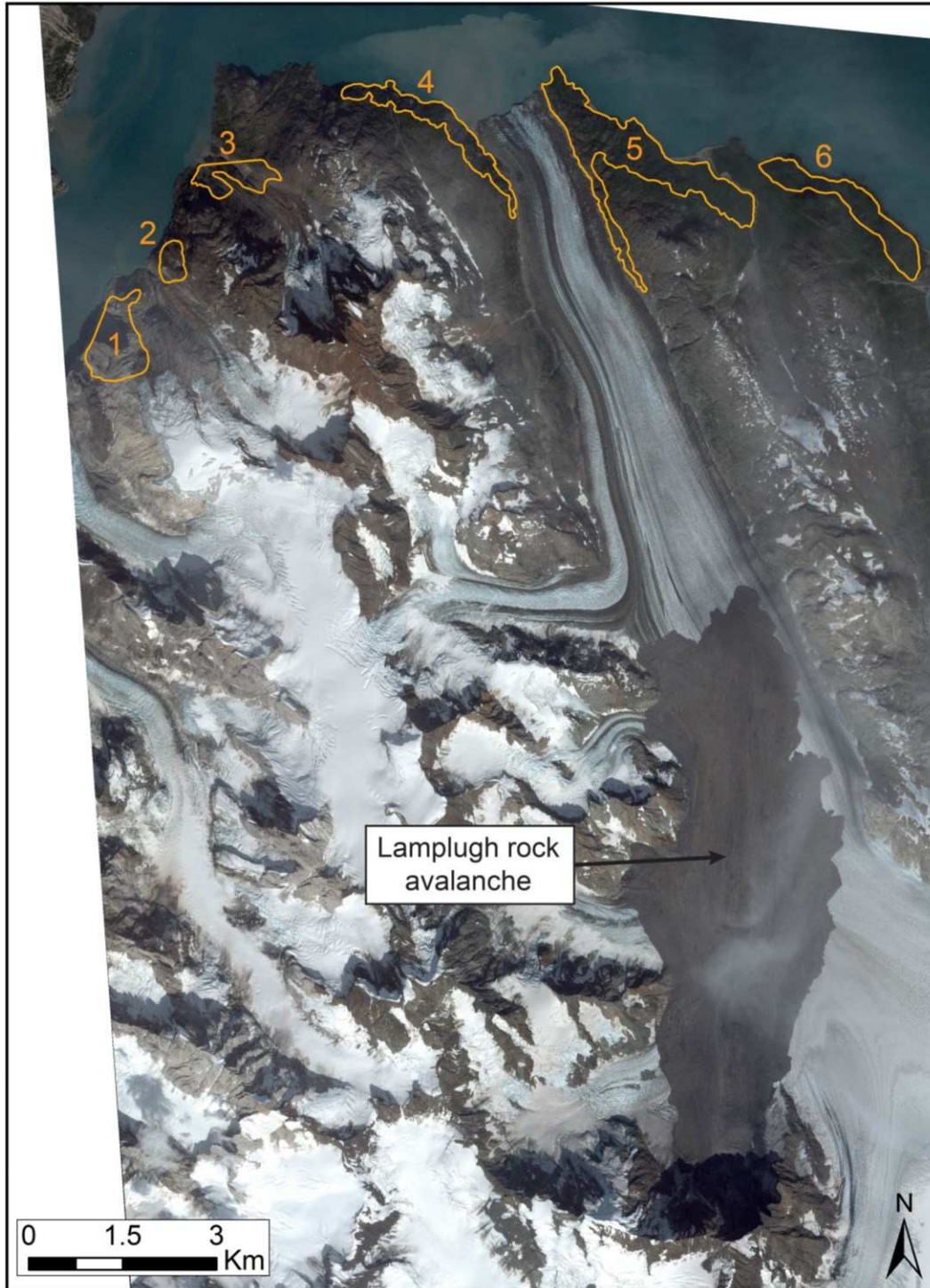


Figure 4-1. Digital Globe Inc. image collected on 8/27/2016 showing the location of the six control areas used to assess the relative accuracy of DEMs produced in ASP.

DEMs of the control areas were produced in ASP and differenced DEMs corresponding to the image sets used for analyses were produced by pixel-wise subtraction. The differenced pixel values from each control area were extracted and used for statistical analyses. The chi-square goodness-of-fit test was used to test the distribution normality of differenced pixel values for each pair of images acquired on a specific date. The chi-square goodness-of-fit test checks the null hypothesis that a dataset was derived from a normal distribution at a given level of confidence. The mean of all differenced elevation values was found for each normally distributed set of differenced elevation values. Since normality cannot be assumed in all cases, an alternative method of estimating the population mean was also used in specific cases. According to the central limits theorem (CLT), the distribution of sample means obtained from random samples within a population will be normally distributed (Davis, 2002). Sampling with replacement with 10,000 replicates was used to find the distribution of sample means for non-normal distributions of differenced elevation values. The mean of this distribution, i.e. mean of the sample means, was used to determine the average elevation difference between each image pair. The standard deviation and interquartile range (IQR) of the differenced elevation distributions were found as measures of the variability in elevation difference that can be expected from processing. The IQR was used in addition to standard deviation since this measure is less sensitive to outliers and is acceptable to use with data that is not normally distributed.

4.6 DEM Differencing

The differences in elevation for each of the image sets listed in Table 4-5 were found using pixel by pixel subtraction. Table 4-5 also describes the use of each differenced DEM in further analyses.

Table 4-5. Dates and uses of differenced DEMs for analysis of the Lamplugh rock avalanche.

Dates of Differenced DEM	Use of Differenced DEM
6/15/2016-7/16/2016	Shortest available time interval between pre- and post-event images; used for primary assessment of elevation changes during emplacement.
7/16/2016-8/27/2016	Post-failure changes within deposit; seasonal snow and ice change on adjacent glacier surface
8/27/2016-9/28/2016	Post-failure changes within deposit; seasonal snow and ice change on adjacent glacier surface
SDMI 5m-9/27/2016	Most complete pre- and post-event coverage in the source area; used for primary assessment of changes during emplacement.
6/15/2016-9/27/2016	Partial coverage of source area; shortest available time interval between pre- and post-event images; used for primary assessment of changes during emplacement.

4.7 Elevation Adjustments

The net snow and ice change between two dates for which stereo imagery is available can be measured by the creation and differencing of DEMs. However, the unmeasured changes in snow and ice between the acquisition of pre- or post-event imagery and the rock avalanche occurrence may be significant. The measured differences between pre- and post-event imagery are indicative of the elevation change between the actual imagery dates, but may not be an accurate representation of surface elevations at the time of the event. To reconstruct the thickness and volume of the Lamplugh rock avalanche at the time of the event, several elevation adjustments must be made to approximate topographic elevations directly before and after the event. The following factors were not immediately accounted for during initial DEM differencing and required additional adjustments:

- A. Snow and ice melt on the adjacent glacier surface between 6/15/2016 (date of pre-event images) and 6/28/2016 (date of rock avalanche).

- B. Snow and ice melt on the adjacent glacier surface between 6/28/2016 (date of rock avalanche) and 7/16/2016 (date of post-event images).
- C. Snow and ice melt in the area covered by the deposit from melting of entrained snow and ice, compaction within the deposit, and/or melting of underlying ice.

The effects of these factors cannot be directly quantified from the data that are available, but they are significant considerations for calculating deposit volume and thickness. The following sections describe how these factors affect both positive and negative areas of the deposit. No elevation adjustments were made in the source area because most of this area consists of bedrock and is not affected by changes to the glacier surface. Three scenarios were examined: Scenario 1 takes into account the elevation loss due to A and assumes B and C are equivalent; Scenario 2 extends Scenario 1 to account for elevation loss due to B, while C is assumed to be zero; Scenario 3 replicates Scenario 2 with a nonzero value of C.

4.7.1 Scenario 1: Areas of Net Positive Elevation

The effect of melting between the acquisition of pre-event images (t_i) and the rock avalanche event (t_e) is represented in Figure 4-2 by a decrease in surface elevation between t_i and t_{e1} (t_e at time step 1). Consequently, the height at which the deposit is emplaced is lower than the surface elevation measured at t_i . Additional melting between emplacement and the acquisition of post-event images (t_f) is assumed to be uniform in areas covered by the deposit and areas on the adjacent surface. In Figure 4-2, the pre- and post-event surfaces that are subtracted during DEM differencing are represented by the light blue and red lines, respectively. The green arrows represent the elevation change measured in individual locations both within the deposit and on the adjacent surface. In areas covered by the deposit, the elevation difference measured between

pre- and post-event DEMs (h_2) is not representative of the entire deposit thickness. If the value of h_2 for every pixel over the deposit area is multiplied by pixel area, the resultant volume will not be representative of the actual deposit volume. The hachured area in Figure 4-2 represents the volume of the deposit that is not measured. This effect is only observed when examining the vertical change between identical locations in space (pixel by pixel), as is done during DEM differencing. The change in elevation on the adjacent glacier surface between t_i and t_f (h_1) is accurately measured by the differenced DEM. The true deposit thickness (th_{true}) is therefore expressed by Equation 4-1.

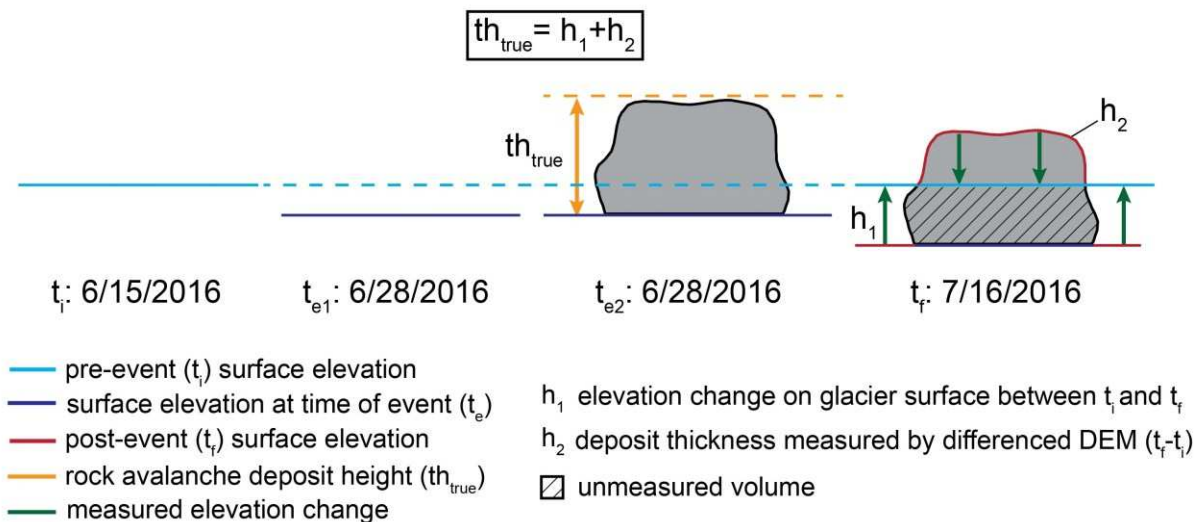


Figure 4-2. Diagram showing the effect of unmeasured changes in surface elevation between the acquisition of pre-event imagery collected on 6/15/2016 and post-event imagery collected on 7/16/2016 and the occurrence of the Lamplugh rock avalanche on 6/28/2016 in deposit areas with net positive volumes. The elevation of the glacier surface at time t_i (light blue line) is subtracted from the surface elevation measured at time t_f (red line) during DEM differencing. The thickness of the deposit measured by DEM differencing (h_2) is not equivalent to the actual thickness of the deposit (th_{true}). True deposit thickness can be measured by summing the difference in elevation on the adjacent glacier surface between t_i and t_f (h_1) with h_2 .

$$th_{true} = h_1 + h_2 \quad \text{Equation 4-1}$$

th_{true} : true deposit thickness (m)

h_1 : change in elevation on the glacier surface measured by DEM differencing between t_i and t_f (m)

h_2 : deposit thickness measured by DEM differencing between t_i and t_f (m)

4.7.2 Scenario 1: Areas of Net Negative Elevation

The impact of unmeasured elevation changes from ice melt is more complex in areas of the deposit that have a net negative elevation. Scour and entrainment of surficial material is assumed to be the cause of deposit areas with a net loss in elevation between 6/15/2016 and 7/16/2016. As discussed in later sections, differential melting cannot be the cause of net negative areas within the extent of the deposit. As shown in Figure 4-3, the effects of unmeasured ice melt in net negative areas are twofold. First, the height of material that is entrained ($h_{entrained}$) is overestimated in areas within the deposit, and second, the thickness of material deposited in the scoured area (h_{fill}) is not accounted for. Figure 4-3 shows a loss in elevation on the glacier surface between t_i and t_{e1} , which is not measured by differencing of pre- and post-event DEMs. Time steps t_{e2} and t_{e3} show scour and entrainment of material and the subsequent deposition of material. The elevation differences in areas on the glacial surface and areas within the deposit which are measured by subtracting the elevation of the pre-event surface (light blue line) and the post-event surface (red line) are represented by h_{1n} and h_{2n} , respectively. If ice melt between t_e and t_f is assumed to be the same in areas covered by deposit and on the adjacent glacier surface, $h_{entrained}$ is expressed by Equation 4-2.

$$h_{entrained} = h_{fill} - h_{1n} + h_{2n} \quad \text{Equation 4-2}$$

$h_{entrained}$: height of material that is scoured and entrained during emplacement (m)

h_{fill} : thickness of the deposit that is emplaced in the scour area (m)

h_{1n} : change in elevation on the glacier surface measured by DEM differencing between t_i and t_f (m)
 h_{2n} : height of scoured area measured by DEM differencing between t_i and t_f (m)

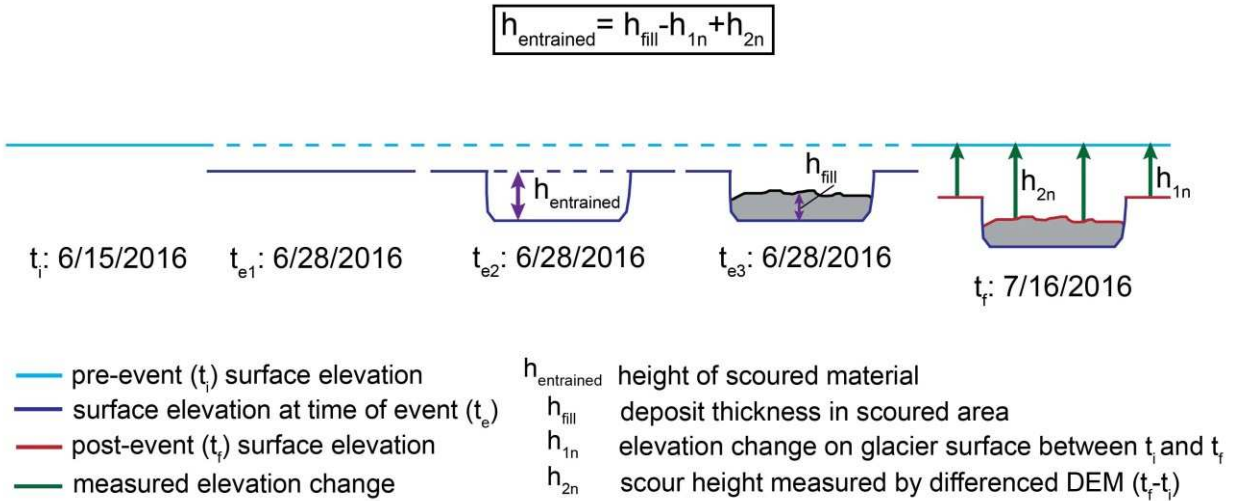


Figure 4-3. Diagram showing the effect of unmeasured changes in surface elevation between the acquisition of pre-event imagery collected on 6/15/2016 and post-event imagery collected on 7/16/2016 and the occurrence of the Lamplugh rock avalanche on 6/28/2016 in deposit areas with net negative volumes. The elevation of the glacier surface at time t_i (light blue line) is subtracted from the surface elevation measured at time t_f (red line) during DEM differencing. Neither the height of scoured and entrained material ($h_{\text{entrained}}$) nor the height of material deposited in the scoured area are represented by the change in elevation measured between t_i and t_f in areas of the deposit (h_{2n}). Elevation change on the adjacent glacier surface between t_i and t_f is represented by the height of h_{1n} . The actual thickness of entrained material can be measured by subtracting h_{1n} from the sum of h_{2n} and h_{fill} .

4.7.3 Scenario 2: Areas of Net Positive Elevation

The case discussed in Scenario 1 becomes more complicated if differential melting between the area covered by debris and the surrounding glacier surface is taken into account. In this case, the deposit is assumed to prevent any ice melt in the area underlying the deposit and it is assumed that the deposit does not undergo compaction from melting of entrained snow and ice or other densification processes. Scenario 3 (below) will explore the adjustments required when there is ice melt under the deposit or compaction within the deposit. Figure 4-4 shows how differential melting affects elevation measurements made during DEM differencing. Time steps

t_i , t_{e1} , and t_{e2} are assumed to be the same as those shown in Figure 4-2. The change in elevation on the adjacent glacier surface between t_e and t_f (h_3) is shown by the purple arrow in Figure 4-4. The value of h_3 cannot be directly measured from pre and post-event DEMs. With the presence of differential melting, the actual thickness of the deposit is expressed by Equation 4-3.

$$th_{true} = h_1 + h_2 - h_3 \quad \text{Equation 4-3}$$

th_{true} : true deposit thickness (m)

h_1 : change in elevation on the glacier surface measured by DEM differencing between t_i and t_f (m)

h_2 : deposit thickness measured by DEM differencing between t_i and t_f (m)

h_3 : change in elevation on the glacier surface between t_e and t_f (m)

The sum of h_1 and h_2 is equivalent to the apparent thickness ($th_{apparent}$) of the rock avalanche deposit on 7/16/2016 rather than the true thickness of the deposit at the time of deposition. This effect is apparent if the thickness of the deposit is observed or measured from two different locations in space (i.e. comparing the height of the deposit with the height of a location on the adjacent ice surface) rather than observing the difference from one location in space (i.e. a specific pixel in the differenced DEM).

4.7.4 Scenario 2: Areas of Net Negative Volume

The modification of Scenario 1 for areas of net negative volume to include differential melting between the adjacent surface and the deposit with the assumption that the change in elevation within the deposit is zero is shown in Figure 4-5. The change in elevation on the adjacent glacier surface between t_e and t_f is measured by h_{3n} . The height of entrained material is found using Equation 4-4.

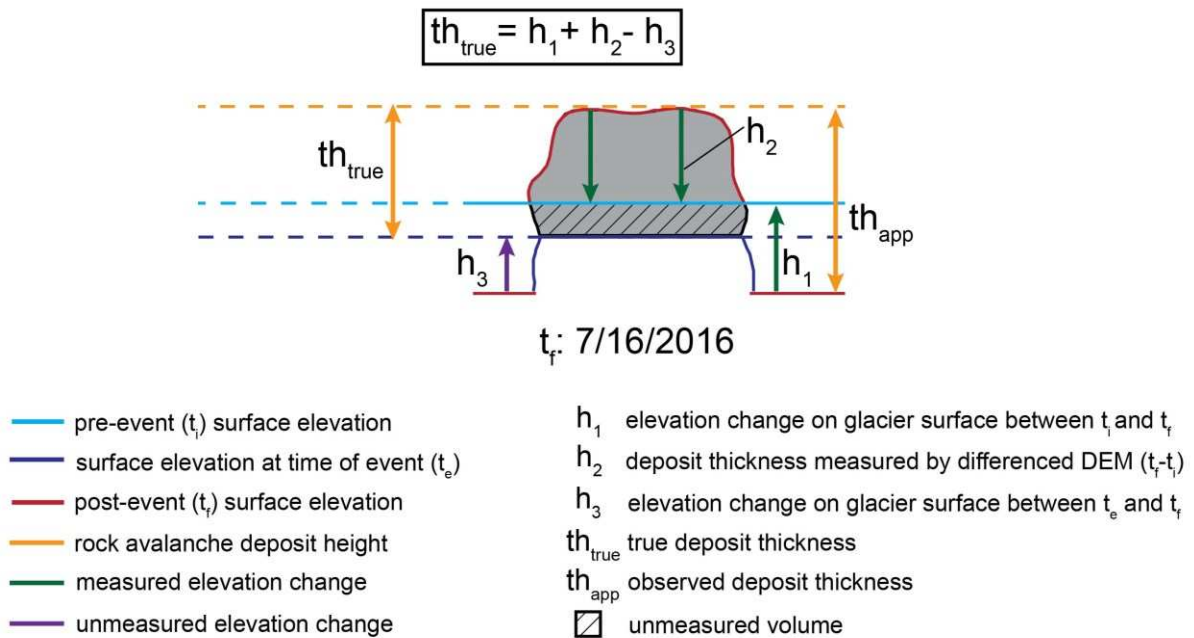


Figure 4-4. Diagram showing the added effect of differential ice melt on ice changes that are not measured during DEM differencing in net positive deposit areas. The change in height of the deposit, either due to melting of underlying ice or melting and densification within the deposit is assumed to be zero. The actual thickness of the deposit (th_{true}) is measured by subtracting the elevation change on the adjacent surface between t_e and t_f (h_3) from the sum of h_1 and h_2 . When observed from an adjacent location in space the presence of differential ice melt causes the observed deposit thickness ($th_{apparent}$) to be greater than th_{true} .

$$h_{entrained} = h_{fill} - h_{1n} + h_{2n} + h_{3n} \quad \text{Equation 4-4}$$

- $h_{entrained}$: height of material that is scoured and entrained during emplacement (m)
- h_{fill} : thickness of the deposit that is emplaced in the scour area (m)
- h_{1n} : change in elevation on the glacier surface measured by DEM differencing between t_i and t_f (m)
- h_{2n} : height of scoured area measured by DEM differencing between t_i and t_f (m)
- h_{3n} : change in elevation on the glacier surface between t_e and t_f (m)

4.7.5 Scenario 3: Areas of Net Positive Volume

Although the loss of ice in areas underlying the deposit or melting of material within the deposit is expected to be less than the loss of elevation on the adjacent glacier surface

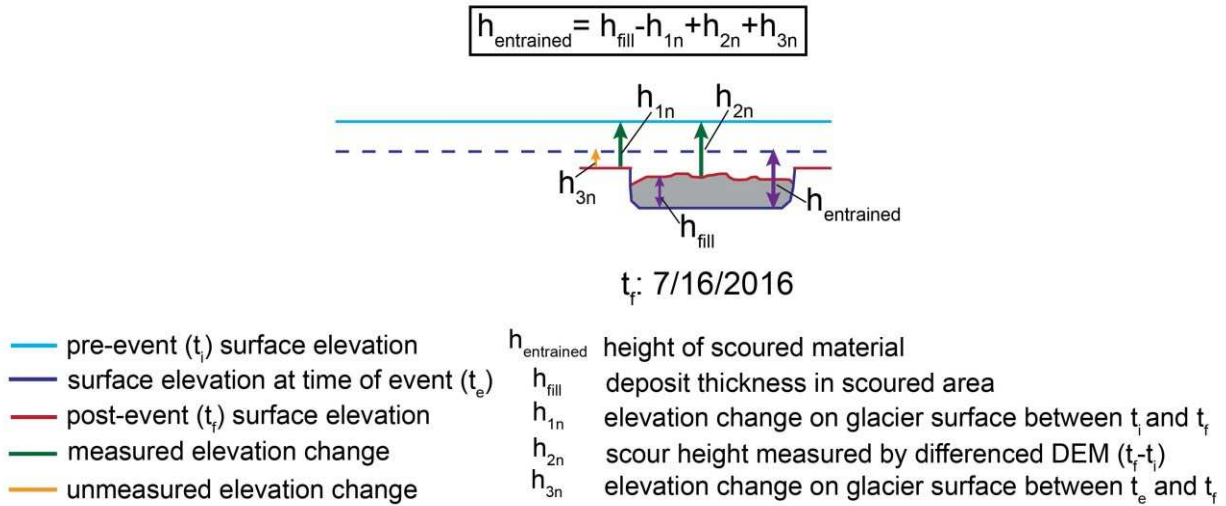


Figure 4-5. Diagram showing the added effect of differential ice melt on ice changes that are not measured during DEM differencing in net negative deposit areas. The change in height of the deposit, either due to melting of underlying ice or melting and densification within the deposit is assumed to be zero. The actual thickness of entrained material ($h_{\text{entrained}}$) is measured by subtracting h_{1n} from the sum of h_{2n} and h_{fill} and the change in elevation on the adjacent surface between t_e and t_f (h_{3n}).

(Jiskoot, 2011; Reznichenko et al., 2011), it is unrealistic to assume that no change in elevation will occur within the deposit. Figure 4-6 extends the scenario shown in Figure 4-4 to include some degree of melting and compaction in the deposit area. The change in elevation within the deposit between t_e and t_f consists of a decrease in elevation due to melting of the underlying ice (h_4) and further decrease in elevation from compaction within the deposit (h_5). Similarly to h_3 , these parameters cannot be measured directly from pre- and post-event DEMs. Additionally, no differentiation between h_4 and h_5 can be made from the data available in this research, so the resultant change from both parameters is notated as the sum (h_4+h_5). In this scenario, the true thickness of the rock avalanche at the time of deposition is expressed by Equation 4-5.

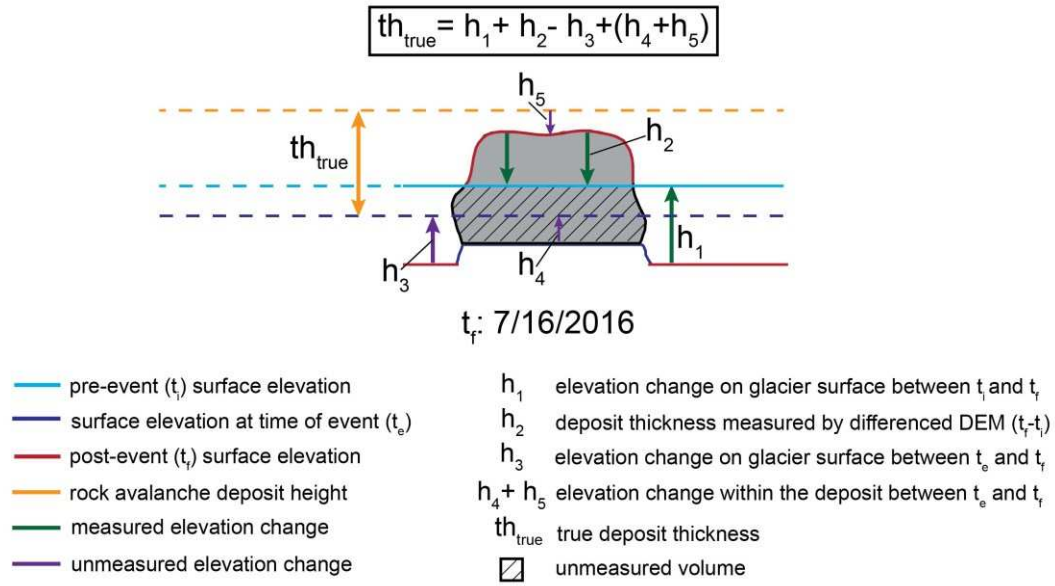


Figure 4-6. Diagram showing the added effect of post-depositional elevation changes within the rock avalanche deposit on ice changes that are not measured during DEM differencing in net positive deposit areas. The actual thickness of the deposit (th_{true}) is measured by subtracting (h_3) from the sum of h_1 , h_2 , and the change in elevation within the deposit between t_e and t_f (h_4).

$$th_{true} = h_1 + h_2 - h_3 + (h_4 + h_5) \quad \text{Equation 4-5}$$

- th_{true} : true deposit thickness (m)
- h_1 : change in elevation on the glacier surface measured by DEM differencing between t_i and t_f (m)
- h_2 : deposit thickness measured by DEM differencing between t_i and t_f (m)
- h_3 : change in elevation on the glacier surface between t_e and t_f (m)
- $h_4 + h_5$: change in elevation within the deposit between t_e and t_f (m)

4.7.6 Scenario 3: Areas of Net Negative Volume

Figure 4-7 shows the additional contribution from melting below the deposit or compaction within the deposit in net negative deposit areas. Post-emplacment changes within the deposit are represented by the height of h_{4n} . The thickness of entrained material is found using Equation 4-6.

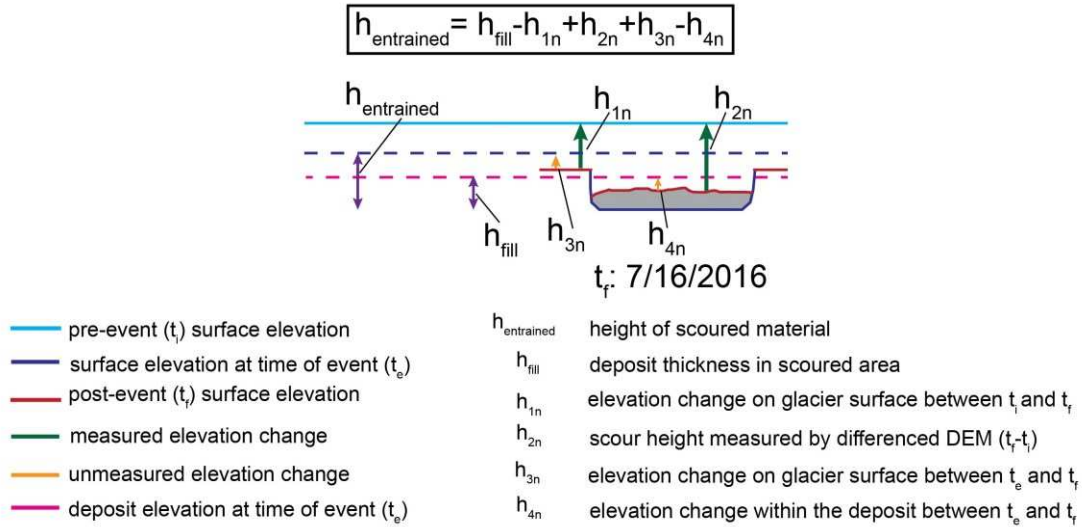


Figure 4-7. Diagram showing the added effect of post-depositional elevation changes within the rock avalanche deposit on ice changes that are not measured during DEM differencing in net negative deposit areas. The actual thickness of entrained material ($h_{\text{entrained}}$) is measured by subtracting the sum of h_{1n} and the change in elevation within the deposit between t_e and t_f (h_{4n}) from the sum of h_{2n} , h_{fill} , and h_{3n} .

$$h_{\text{entrained}} = h_{\text{fill}} - h_{1n} + h_{2n} + h_{3n} - h_{4n} \quad \text{Equation 4-6}$$

- $h_{\text{entrained}}$: height of material that is scoured and entrained during emplacement (m)
- h_{fill} : thickness of the deposit that is emplaced in the scour area (m)
- h_{1n} : change in elevation on the glacier surface measured by DEM differencing between t_i and t_f (m)
- h_{2n} : height of scoured area measured by DEM differencing between t_i and t_f (m)
- h_{3n} : change in elevation on the glacier surface between t_e and t_f (m)
- h_{4n} : change in elevation within the deposit between t_e and t_f (m)

4.8 Volume, Thickness, and Center of Mass

Differenced DEMs were used to determine geometric characteristics of the Lamplugh rock avalanche through pixel-by-pixel calculations.

4.8.1 Volume

Three volume contributions were calculated for the Lamplugh rock avalanche: 1) source volume, 2) deposit volume, and 3) volume of scoured and entrained material. Source volume was calculated by isolating the areas of negative elevation change within the source area. Deposit volume was found by summing areas of positive elevation within both the source and deposit areas with the amount of material that was deposited in the scoured area (h_{fill}). The volume of scoured and entrained material was found using Equation 4-6.

The volume of each area was calculated by integrating the elevation difference of each pixel in the differenced DEM (Equation 4-7).

$$Volume = \frac{A}{n} \sum_{i=1}^n \Delta z_i \quad \text{Equation 4-7}$$

A : area (m^2)

n : number of cells

z_i : elevation difference of the i^{th} pixel (m)

4.8.2 Average Thickness

Similarly, the average thickness of each area was calculated using Equation 4-8.

$$Average\ Thickness = \frac{1}{n} \sum_{i=1}^n \Delta z_i \quad \text{Equation 4-8}$$

A : area (m^2)

n : number of cells

z_i : elevation difference of the i^{th} pixel (m)

4.8.3 Center of Mass

The longitudinal component of the center of mass along a centerline profile extending from the headscarp to the distal margin was calculated using Equation 4-9.

$$y_{COM} = \sum_{i=1}^n \frac{th_i}{th_T} \times y_i \quad \text{Equation 4-9}$$

y_{COM} : longitudinal coordinate of the location of the center of mass (m)

n : number of cells

th_i : thickness of the i^{th} pixel (m)

th_T : total thickness of all n pixels (m)

y_i : longitudinal coordinate of the i^{th} pixel (m)

Accumulation of material as a result of topographic confinement is expected to influence the location of the center of mass within the deposit in comparison to a similar event undergoing completely unconfined spreading. Since the west margin of the Lamplugh rock avalanche is partially confined, the center of mass was calculated separately for both the east and west halves of the deposit to examine the effects of topographic confinement.

4.9 Structural Mapping

In addition to analyzing the overall geometric properties of the Lamplugh rock avalanche, a detailed examination of surficial features and landslide structures within the deposit from satellite imagery at a scale of 1:1000 was used to study movement types and processes.

Terminology from structural geology was used to classify landslide structures. The use of terms such as “strike-slip fault,” “thrust fault,” or “fenster” are used to describe the relative motion of different parts of the rock avalanche deposit and have no connotation to the deformation of bedrock. Differenced DEMs were used in conjunction with WorldView Ortho Ready Standard Stereo imagery to map structural features within the deposit. To produce Ortho Ready Standard images Digital Globe uses data collected from the high-resolution panchromatic band to pan-sharpen the associated, relatively coarse resolution multispectral image to provide the highest possible resolution true color image. As described in Table 4-3 eleven panchromatic and multispectral images ranging in resolution from ~0.3 to 0.5 meters were used to delineate the

deposit extent. Pan-sharpened multi-spectral imagery (0.21 x 0.38-meter resolution) from 7/16/2016 was used to map surficial features and landslide structures throughout the deposit. This image was exclusively used because it provides the best representation of undisturbed depositional features. Images from 9/27/2016 (panchromatic; 0.5-meter resolution) and 10/29/2016 (pan-sharpened multi-spectral; 0.4-meter resolution) were used to map structures in the source area. ArcGIS was used for all mapping.

The 3DAnalyst toolbox in ArcGIS was used to create post-event cross-sectional topographic profiles of the deposit on 7/16/2016 to inform the identification of structures. A hillshade of the deposit from 7/16/2016 and the adjusted differenced DEM between 6/15/2016 and 7/16/2016 were used to confirm the presence of features initially identified in optical imagery.

CHAPTER 5 RESULTS

5.1 DEM Generation

One pre-event and three post-event DEMs with coverage of the rock avalanche deposit, and one post-event DEM with coverage of only the source area, were produced in ASP. The triangulation error for each of the DEMs produced in ASP was determined (Table 5-1) as a measure of how well image correlation was performed. High values of triangulation error are likely due to poor correlation in areas of steep terrain or areas that are obscured by cloud cover or shadows.

Table 5-1. Mean triangulation error in the north-south (Band 1), east-west (Band 2), and vertical (Band 3) directions for each DEM produced in ASP.

DEM Date	Band 1 (m)	Band 2 (m)	Band 3 (m)
6/15/2016	0.70	1.99	0.62
7/16/2016	0.02	0.05	0.01
8/27/2016	0.78	3.23	1.62
9/27/2016	0.07	0.24	0.01
9/28/2016	0.58	1.81	0.11

5.2 DEM Accuracy Analysis

The distribution of differenced elevation values within the control areas was examined to assess the relative accuracy of each pair of differenced DEMs. Since the control areas are located in areas of stable rock with no snow cover, the mean elevation difference between all pixels in the control area is expected to be zero. However, as shown by the distribution of differenced elevation values in Control Areas 4-6 between 6/15/2016 and 7/16/2016 (Figure 5-1), the mean is not centered at zero. Histograms from each of the other differenced DEMs show similar deviations from zero and are included in Appendix A. The results of the chi-square goodness-of-fit test and the mean, standard deviation, and IQR of each distribution are listed in Table 5-2. A

result of zero from the chi-square goodness-of-fit test indicates that the dataset comes from a normal distribution, while a value of one indicates that normality of the dataset cannot be assumed.

A non-zero mean elevation difference between DEMs is attributed to a systematic shift between two individual dates. This shift is most likely caused by one or more of the following factors: slight differences in satellite positioning between acquisition dates, differences in satellite acquisition between satellite platforms, the presence of artifacts in one or both images, and processing inaccuracies in ASP. The mean difference between each DEM pair was used to shift the corresponding differenced DEM for use in the remaining analyses. The IQR represents the range of values within which the middle 50% of the data falls. Similarly, about 68% of the data falls within a range of values equal to plus or minus one standard deviation away from the mean if the data is normally distributed. The differences in standard deviation and IQR indicate that the data distributions are largely concentrated around the mean, with long tails of outliers. Since the IQR is less sensitive to the effects of outliers this measure was used to assess the variability in elevation difference between two individual dates as a result of processing error. Therefore, the relative vertical accuracy for each given set of dates is taken to be $\pm \text{IQR}/2$. The relative vertical accuracy for each pair of DEMs is also listed in Table 5-2.

Table 5-2. Results of the chi-square goodness-of-fit test, mean, IQR, standard deviation, and relative vertical accuracy of elevation difference in control areas between DEM pairs used for differencing analyses.

Dates of differenced DEM	6/15/2016-7/16/2016	7/16/2016-8/27/2016	8/27/2016-9/28/2016	SDMI 5m-9/27/2016	6/15/2016-9/27/2016
Chi-square goodness-of-fit test	0	0	1	1	1
Mean (m)	-2.29	2.17	1.22	13.26	-2.68
Interquartile range (m)	1.43	1.05	1.11	3.93	2.86
Standard deviation (m)	2.05	2.48	2.46	5.40	3.19
Relative vertical accuracy (m)	± 0.72	± 0.53	± 0.55	± 1.96	± 1.43

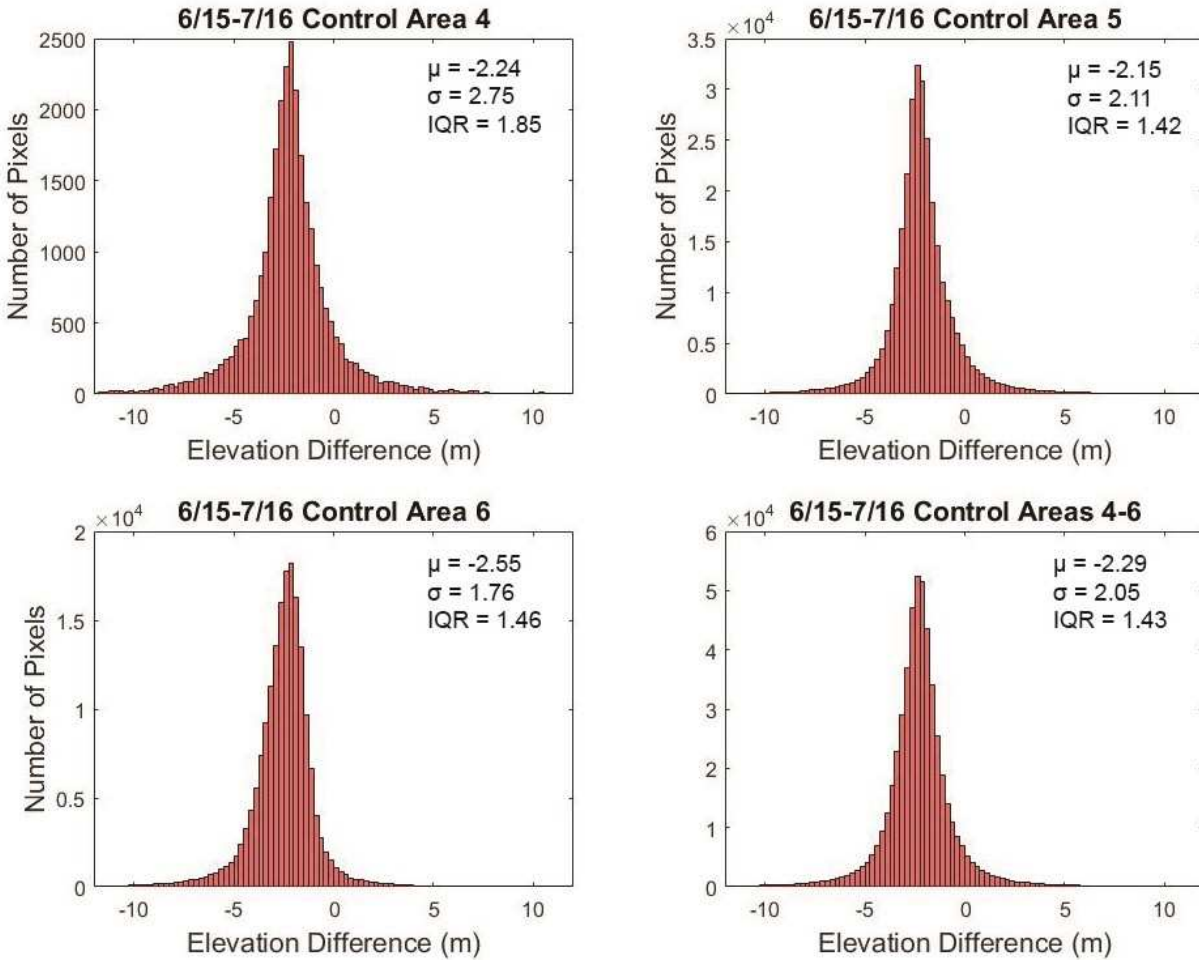


Figure 5-1. Elevation difference in Control Areas 4-6 between 6/15/2016 and 7/16/2016.

5.3 Differenced DEMs

The pre-event DEM from 6/15/2016 and the post-event DEM from 7/16/2016 were used for all analyses of the deposit area because these dates are the closest to the date of occurrence and are therefore most representative of the rock avalanche deposit at the time of emplacement. The elevation difference between 6/15/2016 and 7/16/2016 is shown in Figure 5-2. Differenced elevation data were acquired in the source area (Figure 5-3) by using the pre-event DEM from 6/15/2016 and a SDMI 5-meter DEM with a post-event DEM from 9/27/2016. The differenced DEM between 6/15/2016 and 9/27/2016 is expected to be most representative of changes in

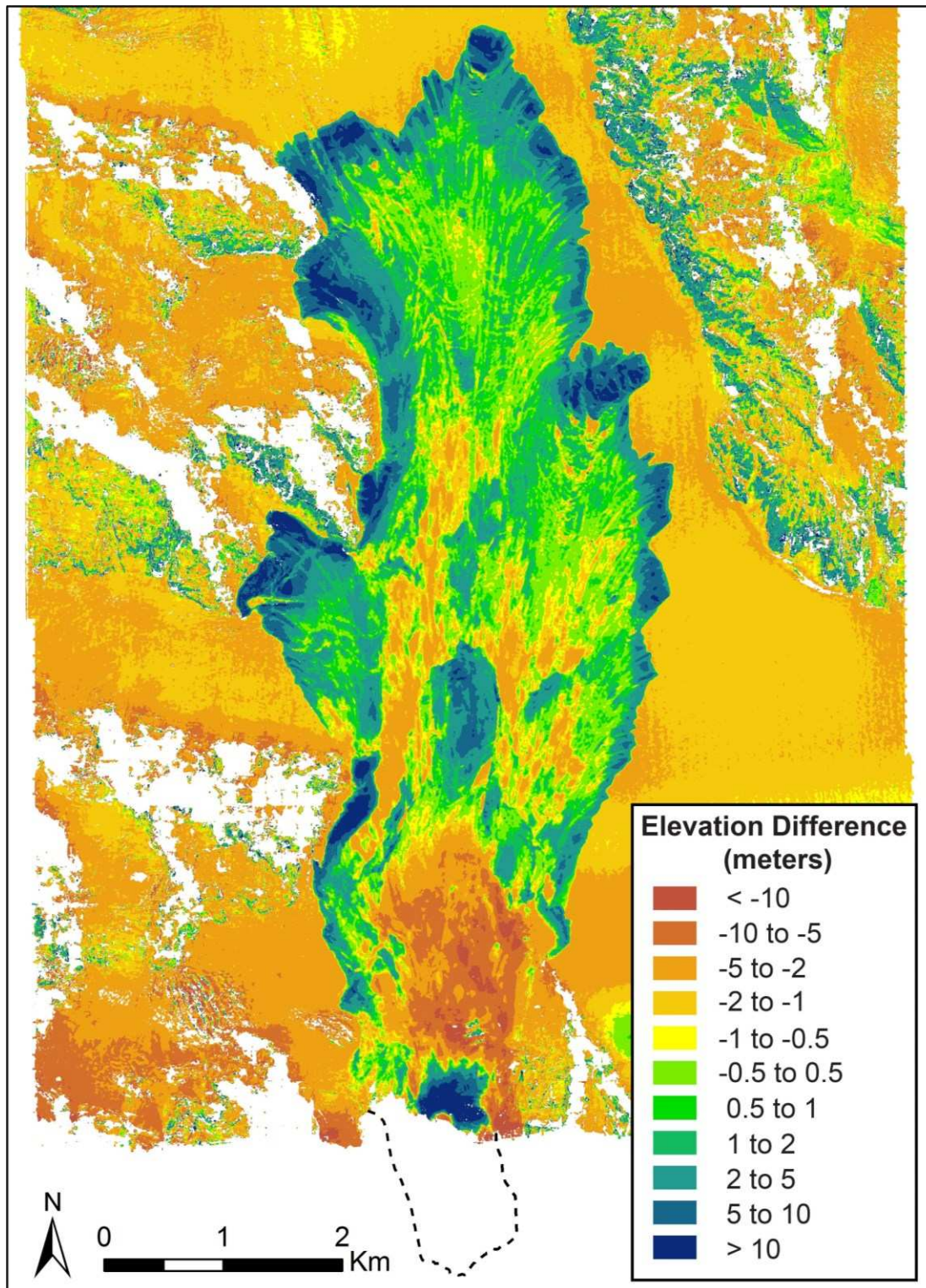


Figure 5-2. Elevation difference between pre- (6/15/2016) and post-event (7/16/2016) DEMs over the Lamplugh rock avalanche deposit. Dashed line indicates extent of source area, which is obscured by clouds in the image acquired on 7/16/2016.

topography from the rock-slope failure, but only partially covers the source area. Elevation values derived from the difference between the SDMI 5-meter and 9/27/2016 DEMs were used in areas that were not covered by the DEM from 6/15/2016.

Elevation differences between 7/16/2016-8/27/2016 and 8/27/2016-9/28/2016 (Figure 5-4) were used to observe progressive changes in the deposit and to make estimates of seasonal snow and ice changes on the glacial surface surrounding the deposit. The average elevation change on the adjacent glacier surface was calculated between 6/15/2016-7/16/2016, 7/16/2016-8/27/2016, and 8/27/2016-9/28/2016 and the average elevation change within both positive and negative areas of the deposit was calculated between 7/16/2016-8/27/2016 and 8/27/2016-9/28/2016. The absolute elevation changes in addition to the daily rate of elevation change for each period are listed in Table 5-3.

Table 5-3. Elevation changes on the Lamplugh rock avalanche deposit and adjacent surfaces measured as average total change and average daily rate of change between specified dates in June (pre-event), July, August, and September, 2016. Changes in elevation are measured on A) the glacier surface adjacent to areas of the deposit with a net positive volume, B) areas of the deposit with a net positive volume, C) the surface adjacent to areas of the deposit with a net negative volume, and D) areas of the deposit with a net negative volume.

Dates of Differenced DEM	6/15/2016-7/16/2016	7/16/2016-8/27/2016	8/27/2016-9/28/2016
Average elevation change on A (m)	-1.84	-3.46	-1.56
Average rate of elevation change on A (m/day)	-0.06	-0.08	-0.05
Average elevation change on B (m)	--	-1.44	-1.01
Average rate of elevation change on B (m/day)	--	-0.03	-0.03
Average elevation change on C (m)	-3.33	-3.31	-1.06
Average rate of elevation change on C (m/day)	-0.11	-0.08	-0.03
Average elevation change on D (m)	--	1.63	0.34
Average rate of elevation change on D (m/day)	--	0.04	0.01

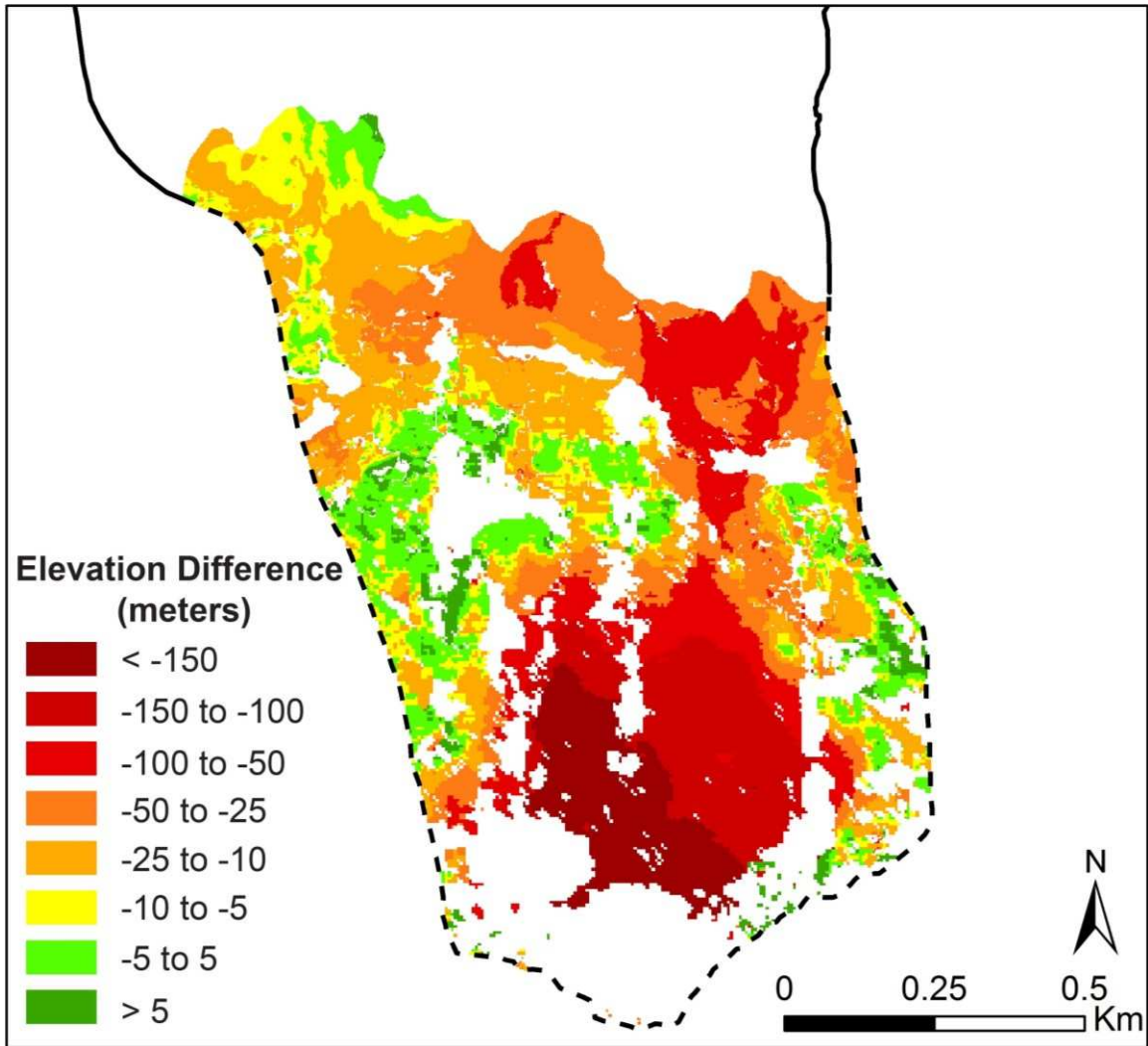


Figure 5-3. Elevation difference between pre- (6/15/2016 and SDMI 5-meter) and post-event (9/27/2016) DEMs in the source area of the Lamplugh rock avalanche.

5.4 Elevation Adjustments

The examination of elevation differences within the deposit and on the adjacent glacier surface between 6/15/2016-7/16/2016 and two additional post-event dates (8/27/2016 and 9/28/2016), as shown in Figure 5-2 and 5-4, indicate that elevation changes on the adjacent glacier surface occurred throughout the period from June through September. Additionally, post-event changes measured in August and September indicate that the elevation of the deposit

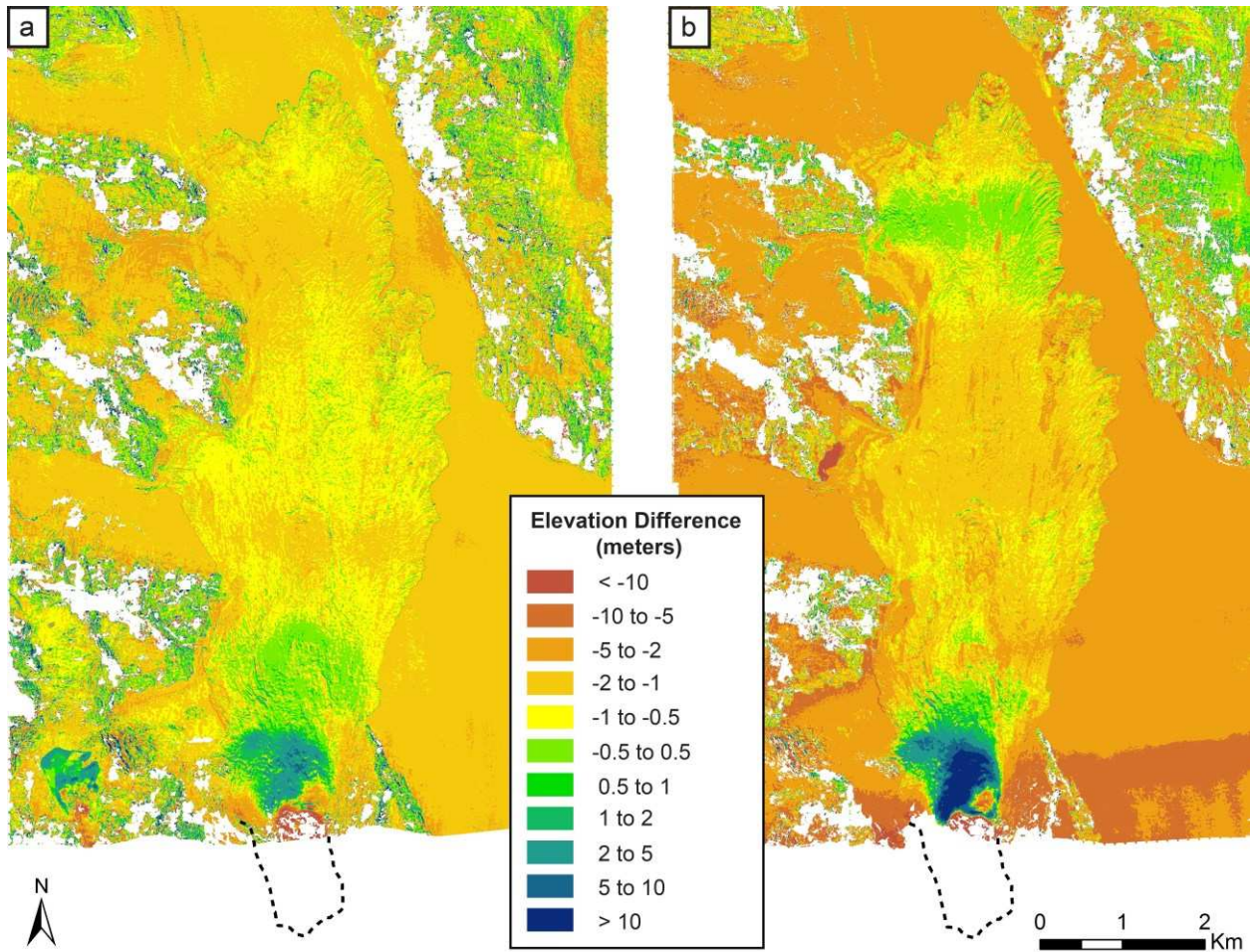


Figure 5-4. Differenced DEMs between a) 7/16/2016-8/27/2016 and b) 8/27/2016-9/28/2016 showing post-event changes within the Lamplugh rock avalanche deposit and on the adjacent glacial surface.

decreased after deposition, but changes within the debris covered area were less than changes on the adjacent ice surface. This observation shows that snow and ice melt was retarded by the rock avalanche deposit.

Based on observations of post-event elevation losses within the deposit and on the adjacent glacier surface, Equations 4-5 and 4-6 were used to calculate elevation adjustments. The parameters required to solve for h_{true} and $h_{entrained}$ (Equations 4-5 and 4-6, respectively) are summarized in Table 5-4 and were found as follows.

Table 5-4. Measured and estimated parameters used in Equations 4-5 and 4-6 to calculate elevation adjustments for differences in elevation between 6/15/2016 and 7/16/2016 in the area of the Lamplugh rock avalanche deposit. Since h_2 and h_{2n} are measured from the changes in elevation in the deposit area between 6/15/2016 and 7/16/2016, these values are unique for each pixel of the differenced DEM (Figure 5-2) and are not reported here (i.e., N/A entries).

	<i>Areas of net positive volume</i>		<i>Areas of net negative volume</i>		
Measured Parameters	h_1	h_2	h_{1n}	h_{2n}	
Measured Value (m)	-1.84	N/A	-3.33	N/A	
Estimated Parameters	h_3	h_4	th_{scour}	h_{3n}	h_{4n}
Estimated Value (m)	-1.14	-0.59	1-4	-1.32	-0.59

The value of h_1 was measured from the change in elevation of the adjacent surface between 6/15/2016 and 7/16/2016. The values of h_2 and h_{2n} are measured from changes in elevation over the deposit between 6/15/2016 and 7/16/2016. These values are unique for each pixel within the deposit and are therefore not reported in Table 5-4. The change in elevation on the adjacent surface between 6/28/2016 and 7/16/2016 (h_3) was estimated by scaling the total snow and ice loss on the adjacent surface during the 31 days between 6/15/2016 and 7/16/2016 for the 18-day period between 6/28/2016 and 7/16/2016. Change in elevation within the deposit between 6/28/2016 and 7/16/2016 from ice melt of the underlying glacial surface and melting of entrained snow and ice (h_4) was estimated from the daily average elevation loss over the deposit between 7/16/2016-8/27/2016 and 8/27/2016-9/28/2016. The value of h_4 was also used for areas of net negative volume (h_{4n}) because post-event DEMs show an elevation increase in these areas. This positive elevation change is likely due to continued deposition at the base of the source area and is exemplified by the dark blue area directly below the source area in Figure 5-4. A range of values was estimated for the thickness of the deposit in the scoured area (h_{fill}) through examination of multispectral imagery and the use of elevation data from 7/16/2016, since this value cannot be directly calculated. The local relief of fensters in the scour area ranges between 2 and 4 meters. The debris cover appears very thin to absent in some locations. Based on these

observations, h_{fill} was estimated to range from 1-4 meters. The average thickness determined for the remainder of the deposit was assumed to also represent the average deposit thickness in this area. The elevation differences between 6/15/2016-7/16/2016 (Figure 5-2) were adjusted by applying Equation 4-5 to each pixel in areas of the deposit with a net positive elevation and by applying Equation 4-6 to each pixel in areas of the deposit with a net negative elevation. Equations 4-5 and 4-6 give adjustments of 1.29 meters and -1.21 meters for net positive and negative deposit areas, respectively. Figure 5-5 shows the resulting differenced DEM, which is a reconstruction of the change in surface elevation between two theoretical times just before and just after occurrence of the Lamplugh rock avalanche. The deposit at the base of the source area is likely a product of continuing accumulation between the time of the event and the acquisition of post-event imagery on 7/16/2016.

5.5 Volume, Thickness, and Center of Mass

The adjusted differenced DEM (Figure 5-5) was used for all calculations of rock avalanche geometry, as described in the following sections.

5.5.1 Volume and Average Thickness

Major areas of depletion and accumulation were used to divide the total rock avalanche area into six distinct zones (Figure 5-6). The delineation of zones A-F was used to quantify the distribution of material throughout the deposit. The differenced DEM shows a net loss of material in the source and scour areas (zones A and C, respectively). A significant accumulation of material occurs just below the source area (Zone B), in a toe-like feature in the middle of the

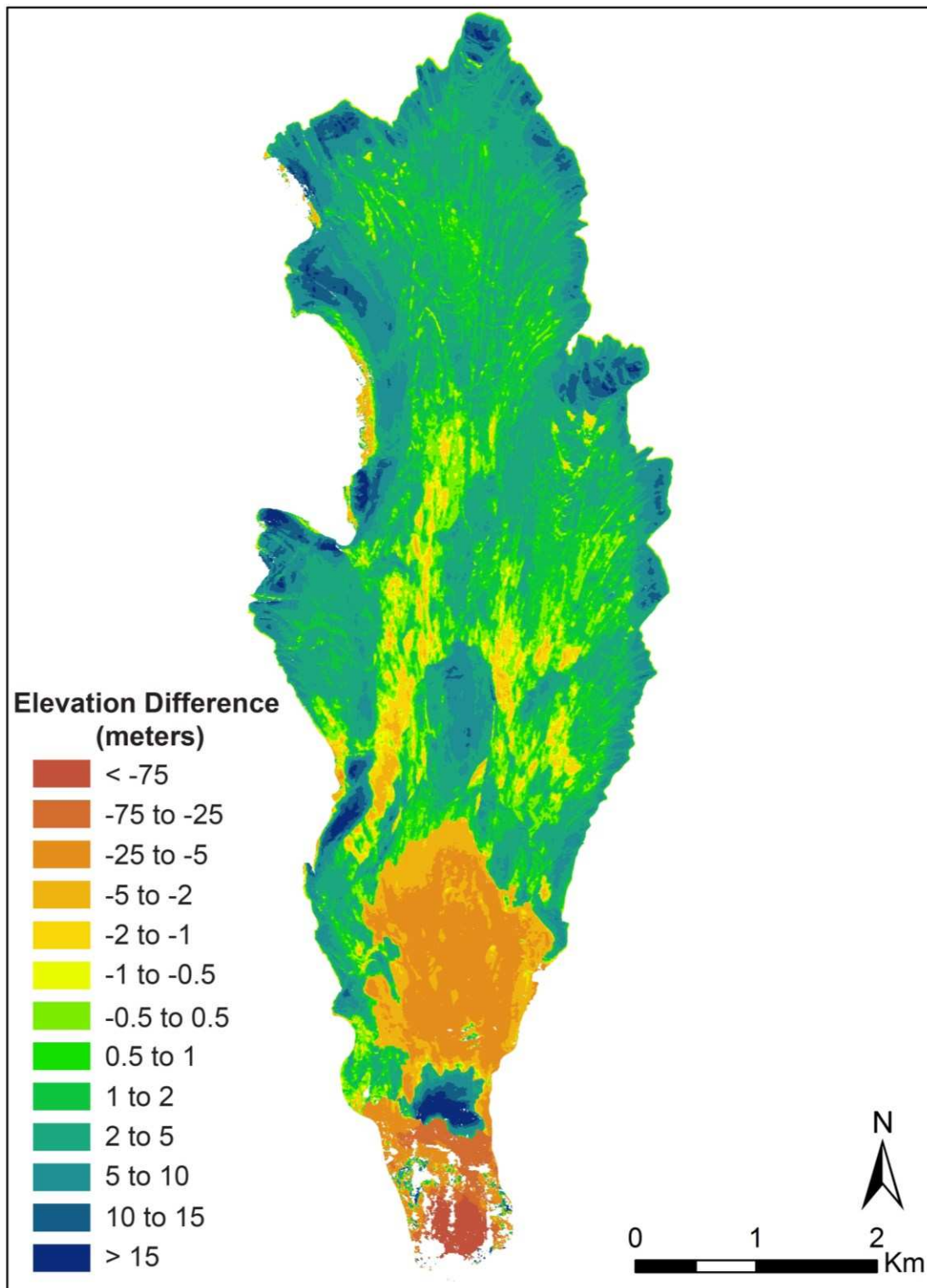


Figure 5-5. Adjusted elevation difference between pre- and post-event DEMs over the Lamplugh rock avalanche. Data in the source area are from a 5-meter resolution SDMI DEM (pre-event) and an ASP-generated DEM from 9/27/2016 (post-event). Data within the remainder of the deposit are derived from ASP DEMs from 6/15/2016 (pre-event) and 7/16/2016 (post-event).

deposit (Zone D), and along the lateral and distal margins (Zone F). The accumulation of material along the margins forms lateral and distal rims ranging from approximately 250 to 850 meters in width. A transport area (Zone E) contains areas of accumulation and depletion and generally appears very thin. Please refer to Appendix C for identification of zones A-F on pre- and post-event elevation profiles through a longitudinal cross-section of the rock avalanche deposit.

The zonation of the Lamplugh rock avalanche shown in Figure 5-6 was made purely based on the final areal extent of each zone and does not account for vertical overlap of material that may span multiple zones (for example, material from Zone A passed through Zone E before stopping in Zone F). Calculations of volume and average thickness were made for different areas of the deposit to determine the overall distribution of material rather than to examine the characteristics of separate surges of movement that may span more than one of the delineated deposit zones. The volume and average thickness calculated from the adjusted, differenced DEM (Figure 5-5) for each zone are listed in Table 5-5.

A range of volumes based on the relative vertical accuracy (Table 5-2) between each DEM pair was determined for each zone and is listed in Table 5-5. The calculated volume ranges are based only on processing error and do not account for other sources of error, such as errors resulting from the estimation of parameters used to calculate elevation adjustments (Section 5.4). Minimum and maximum volumes for each zone were found by adding or subtracting the relative vertical accuracy from the adjusted differenced DEM (Figure 5-5) before applying Equation 4-7. The relative accuracies of the differenced DEMs covering the source area are ± 1.96 meters (SDMI 5m-6/15/2016) and ± 1.43 meters (6/15/2016-9/27/2016), while the relative accuracy of the differenced DEM covering the deposit area is ± 0.72 meters. The error associated with the

volume of material deposited in Zone C was calculated by determining the minimum and maximum average thicknesses in Zone E that could result from a processing error of ± 0.72 meters. Each of these thicknesses was multiplied by the area of Zone C to determine the corresponding minimum and maximum deposit volumes. Since relative elevation accuracy is expected to decrease in areas of steeper slopes (Tsutsui et al., 2007), larger errors could be associated with steep parts of the source area. However, the average slope in the source area is 40.4 degrees, which is within the range of average slope values in the control areas that were used to assess the relative accuracy of DEMs with coverage of the source area (Control Areas 1-3). Thus, no further volume error analyses were performed.

The error in the total volume of deposited material is 24.7%, while the error in the total volume of depleted material is 4.4%. These errors yield ranges of 44.6-73.8 Mm³ and 61.2-66.8 Mm³ for the total amount of deposited and depleted material, respectively. Since the calculation of error is based on the relative vertical accuracy, zones in which thin deposits cover a relatively large area have the largest percent volume error. The percent error in volume for Zone E is nearly 50% since the relative vertical accuracy (± 0.72 meters) is greater than half of the average deposit thickness (1.4 meters). In areas with thick deposits (zones B and F) or large elevation losses (zones A and C) the percent errors do not exceed 12%.

The source area contains areas of both net positive and net negative elevation change. To differentiate between eroded areas and areas in which failed material had presumably accumulated, the positive and negative contributions to volume in the source area were separated. As shown in Figure 5-3, the use of every available elevation dataset did not eliminate all of the areas with missing data in the source area. The average negative elevation change in the source area was multiplied by the amount of missing area to account for holes in the differenced

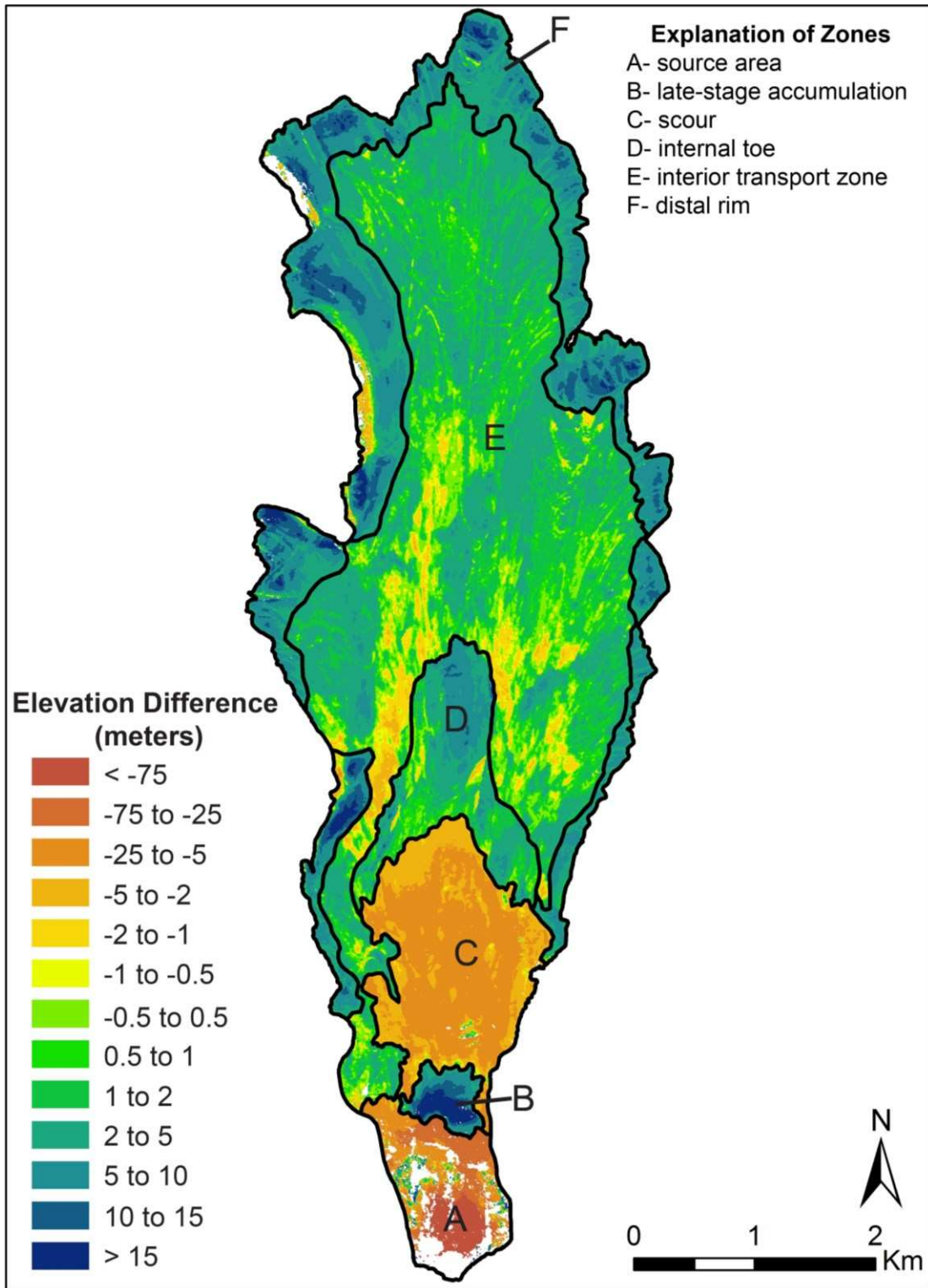


Figure 5-6. Zones of the Lamplugh rock avalanche delineated based on areas of accumulation and depletion identified in the adjusted differenced DEM between 6/15/2016 and 7/16/2016 (Figure 5-5).

DEM. This value was added to the volume of areas with negative differenced elevations to obtain a total source volume of 49.8 Mm³.

The total deposit volume partially consists of the accumulated material in zones A, B, D, E, and F, all of which are visible in Figure 5-5. The positive accumulation of material in Zone C, which is evident in optical imagery, is not measured in the adjusted differenced DEM. The volume of material deposited in Zone C was calculated by multiplying the average thickness determined for the interior transport area (Zone E) by the area of Zone C. The total volume of deposited material was found, by summing the positive volume contributions from zones A-F, to be 59.2 Mm³.

The volume of scoured material from Zone C was calculated to be 14.2 Mm³, which yields 64 Mm³ of total eroded material from zones A and C. Based on the assumption that the material eroded from Zone C, which was likely a combination of snow, ice, and rock, remained within the deposit, this material is part of the volume contribution from zones D, E, and F. It is difficult to make a direct mass balance comparison between the total amount of accumulated and depleted material because the compositions of the failure mass and the scoured and entrained material are unknown. It is likely that some portion of the volume calculated for these areas consisted of snow and ice. However, based on the appearances of zones A and C in pre-event imagery, it is estimated that the majority of the 49.8 Mm³ of material that failed in the source area consisted of rock. The presence or amount of snow and ice that was part of the failure mass cannot be evaluated from the data that are available in this research. As the failed rock mass traveled downslope, an additional 14.2 Mm³ of material was scoured and entrained. Thus, the total amount of rock, ice, and snow mobilized by the Lamplugh rock avalanche was 64 Mm³.

Table 5-5. Deposit volumes and average thicknesses for each zone of the Lamplugh rock avalanche.

Deposit Zone	Area (km²)	Volume (Mm³)	Volume Error (Mm³)	Volume Error (%)	Average Thickness (m)
<i>A (eroded material)</i>	0.7	-49.8	±1.2	2.4	-54.2
<i>A (deposited material)</i>	0.1	0.45	±0.1	22.2	8.3
<i>B</i>	0.3	3.1	±0.2	6.5	11.6
<i>C (scoured material)</i>	2.3	-14.2	±1.6	11.3	-6.2
<i>C (deposited material)</i>	2.3	3.2	±1.6	50	1.4
<i>D</i>	1.5	4.5	±1.1	24.4	3.0
<i>E</i>	11.0	16.7	±7.9	47.3	1.4
<i>F</i>	5.1	31.0	±3.7	11.9	6.1
Total deposited material	20.3	59.2	±14.6	24.7	--
Total eroded material	3.0	64.0	±2.8	4.4	--

5.5.2 Center of Mass

Center of mass locations for the entire Lamplugh rock avalanche deposit in addition to the center of mass locations for only the east and west halves of the deposit are listed in Table 5-6. These results indicate that the center of mass of the east side of the deposit, which spread over the unconfined glacier surface, is located closer to the distal edge than the center of mass of the confined side of the deposit.

Table 5-6. Longitudinal locations of the center of mass for the entire Lamplugh rock avalanche deposit and for only the east (unconfined) and west (confined) halves of the deposit.

	Length from point of origin at center of headscarp (m)	% change from center of mass of entire deposit (+ value indicates shorter distance to headscarp)
<i>Entire deposit</i>	4266.1	--
<i>West side only</i>	4477.2	5.0
<i>East side only</i>	4032.7	-5.5

5.6 Structural Mapping

Strike-slip faults, thrust faults, fault scarps, transverse ridges, and fensters were identified from satellite imagery as structures related to the primary emplacement mechanism of the Lamplugh rock avalanche. Entrained snow and ice, dust deposits and run-up areas were additionally identified as surficial features that were related to the primary mode of emplacement. Infilled crevasses were identified as secondary deposit structures that formed after emplacement. A simplified representation of the structures and surficial features mapped in the Lamplugh rock avalanche deposit is shown in Figure 5-7. A complete 1:16,000 scale map of structures and surficial features is included in Appendix B. The characteristics of each set of structures or features are discussed in the following sections.

5.6.1 Strike-slip faults

Strike-slip faults were identified throughout the deposit and indicate the general direction of movement and differential shearing within the avalanche deposit. Strike-slip faults were identified by visible offsets in deposit material and the presence of longitudinal ridges and furrows. Offsets in material type are only visible in localized areas in which transverse bands of material differing in color or composition are cross-cut by shearing in the longitudinal direction. Indications of strike-slip faulting along longitudinal ridges or furrows are prevalent throughout the deposit. In some areas of thick accumulation of material around the margin, vertical offset along strike-slip faults is present, resulting in the formation of longitudinal ridges and furrows. Elsewhere, strike-slip faults appear as linear features with minimal to no vertical offset, many of which can be seen in the adjusted differenced DEM (Figure 5-5). Along the lateral margins some strike-slip faults curve along the arcuate flow paths of individual lobes. Differential movement is

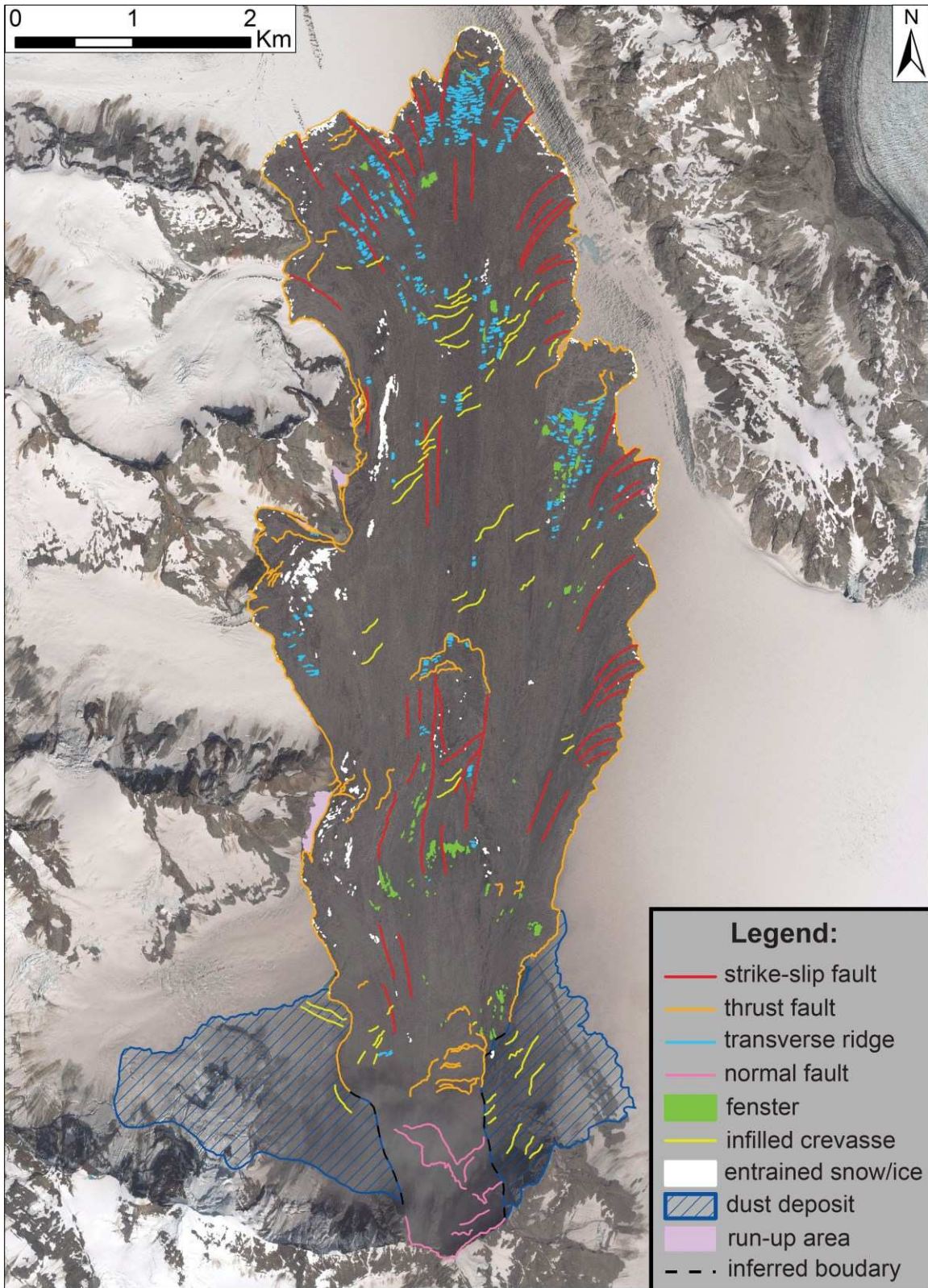


Figure 5-7. Generalized representations of structures and surficial features (1:48,000 scale) mapped on a Digital Globe, Inc. image (7/16/2016) of the Lamplugh rock avalanche.

manifested most prominently along strike-slip faults in the east lateral and distal margins.

Individual strike-slip faults extend up to 1000 meters in length between the middle and edge of the deposit. An example of strike-slip displacement along the west side of the distal margin is shown in Figure 5-8.

5.6.2 Thrust faults

Thrust faults are concentrated along the edges of the deposit and in zones B and D, where material has overridden possibly previously deposited, underlying avalanche material.

Additionally, nearly the entire boundary of the rock avalanche deposit is a thrust fault characterized by movement over the underlying, pre-event ice surface. The accumulation of material along the lateral and distal rims appear to have been formed by a series of sequential thrusts. Thrust faults indicate zones of compression, and in many locations throughout the deposit, thrust faults can be identified by raised ridges in the post-event DEM. Along the lateral and distal margins, thrust faults within the deposit and along the boundary are cut by strike-slip faults.

5.6.3 Fault scarps

Normal fault scarps indicate zones of extension and were most prominently identified in the source zone. In the optical imagery used for mapping, visibility of the source area is limited by either cloud cover, shadowing, or the presence of a dust cloud, which has likely limited the identification of normal faults.

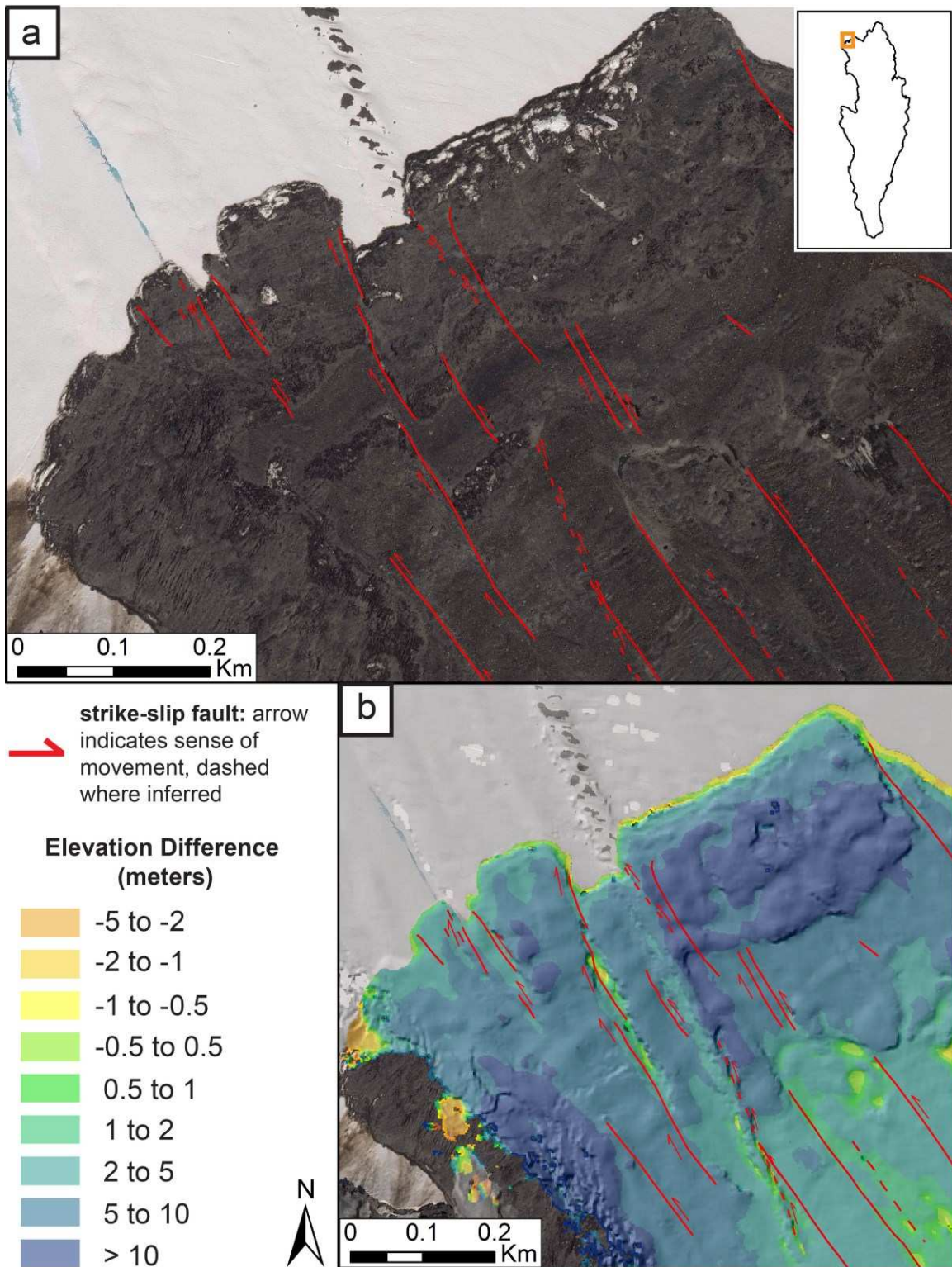


Figure 5-8. Strike-slip movement along the distal margin of the Lamplugh rock avalanche deposit exemplified in a) Digital Globe, Inc. imagery from 7/16/2016 and b) adjusted differenced DEM between 6/15/2016 and 7/16/2016 (Figure 5-5).

5.6.4 Transverse ridges

Relatively small compressional structures oriented transverse to the direction of flow were identified throughout the deposit. These structures were interpreted to be either folds or thrust faults, or both. The differentiation between types of compressional features cannot be confirmed without field observations. Transverse ridges are most prominent in three zones near the deposit margin. In these areas, the transverse ridges are located just proximally to the thickest accumulation of material along the rim. A concentration of transverse ridges was also identified in the distal margin of the internal toe (Zone D). In localized areas throughout the deposit, bands of transverse ridges are roughly aligned normal to the direction of adjacent strike-slip faults. In comparison to the thrust faults identified within the deposit, transverse ridges are significantly smaller in both lateral extent and vertical offset. The presence of transverse ridges appears to indicate areas of localized compression. Transverse ridges range in length from ~10 meters to ~125 meters, with an average length of approximately 30 meters. The relief across these features ranges from approximately 0.5 to 4 meters. An example of transverse ridges in the deposit toe is shown in Figure 5-9. This figure shows that the transverse ridges do not have the same orientation as crevasses in the underlying ice.

5.6.5 Fensters

The term 'fenster' is defined in structural geology as a window which exposes underlying rock through erosion from tectonic movement. In this context, fenster is used to characterize depressions in the rock avalanche deposit through which the underlying glacial ice surface is exposed. In addition to the presence of underlying ice, areas of negative relief within the deposit, as identified in the differenced DEM (Figure 5-5) were used to identify and delineate fensters. In

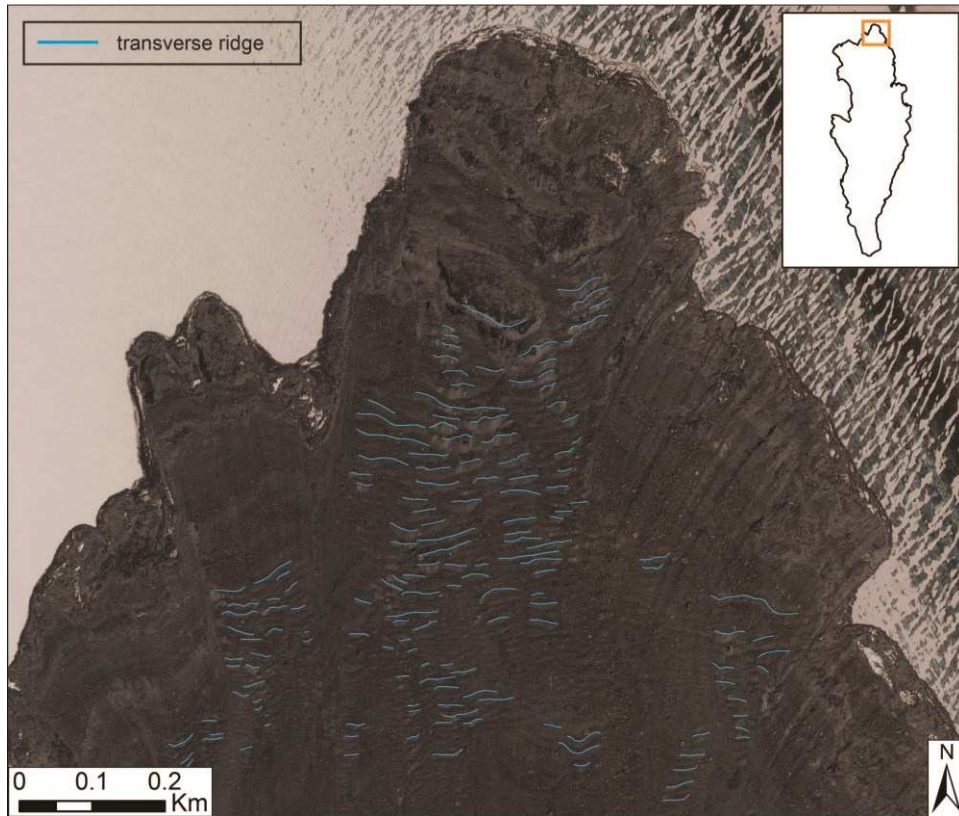


Figure 5-9. Digital Globe, Inc. image taken on 7/16/2016 showing transverse ridges in the toe of the Lamplugh rock avalanche.

some locations, fensters expose striations in the underlying ice. Additionally, several small fensters have been identified directly behind (upslope relative to the overall direction of movement) boulders ranging in size from approximately 3 to 13 meters in diameter. In these locations, the fensters appear to have formed from the movement of individual boulders. The formation of fensters is presumed to have occurred relatively late in emplacement, because many of these structures are well-preserved in the rock avalanche deposit. Additionally, alignment with the localized direction of strike-slip motion along the deposit margins indicates that some fensters formed in conjunction with at least one phase of strike-slip faulting. An example of fensters near the east lateral margin of the rock avalanche deposit is shown in Figure 5-10.

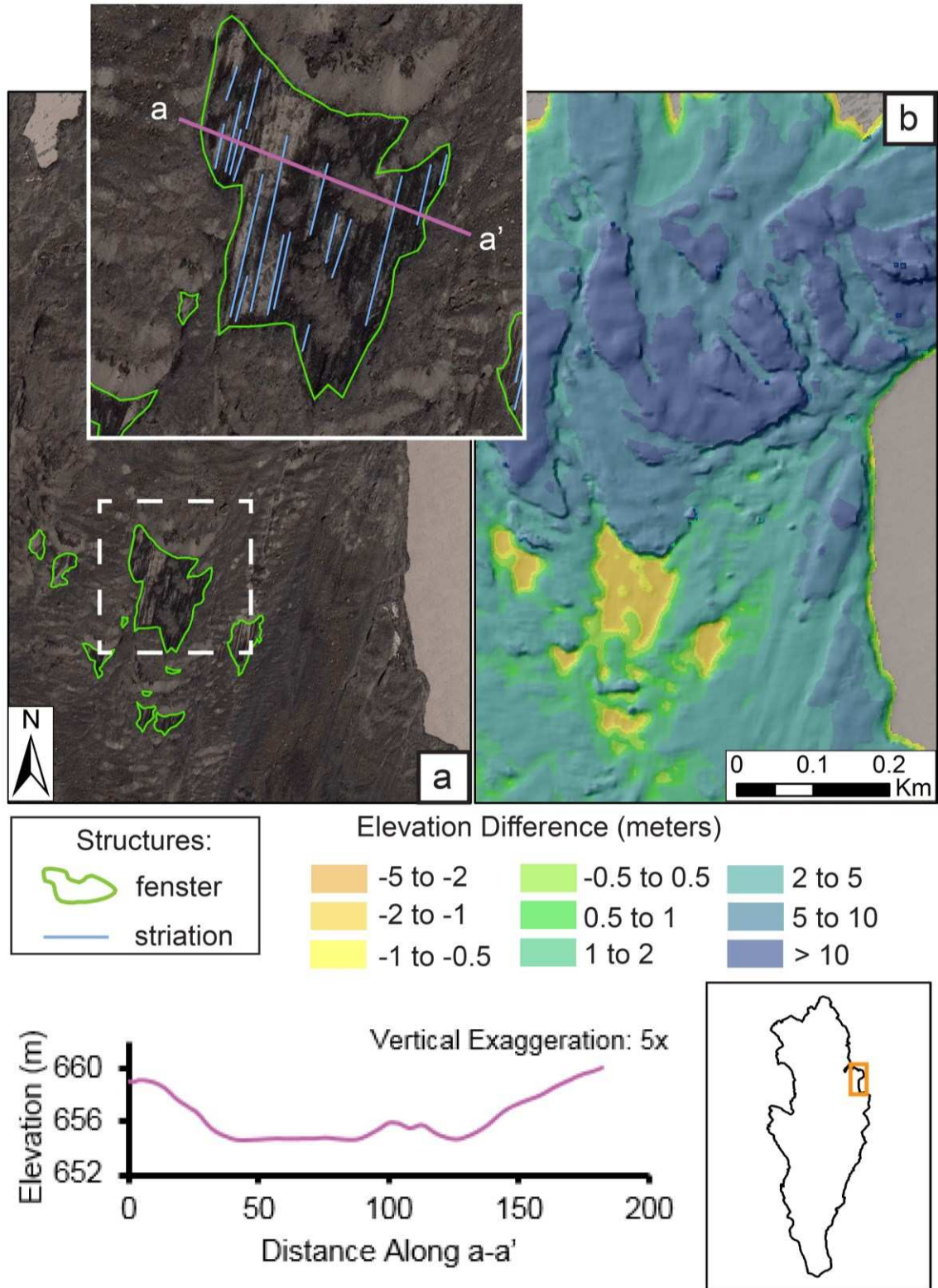


Figure 5-10. Example of fensters identified in a) Digital Globe, Inc. imagery from 7/16/2016 and b) adjusted differenced DEM between 6/15/2016 and 7/16/2016 (Figure 5-5). Profile a-a' was derived from the post-event (7/16/2016) DEM.

5.6.6 Run-up

Run-up occurs in three locations along the west lateral margin of the deposit (Figure 5-11) where moving material encountered areas of steep topographic relief. In these areas material appears to have partially ascended the adjacent slope before losing energy and sliding back to lower elevations.

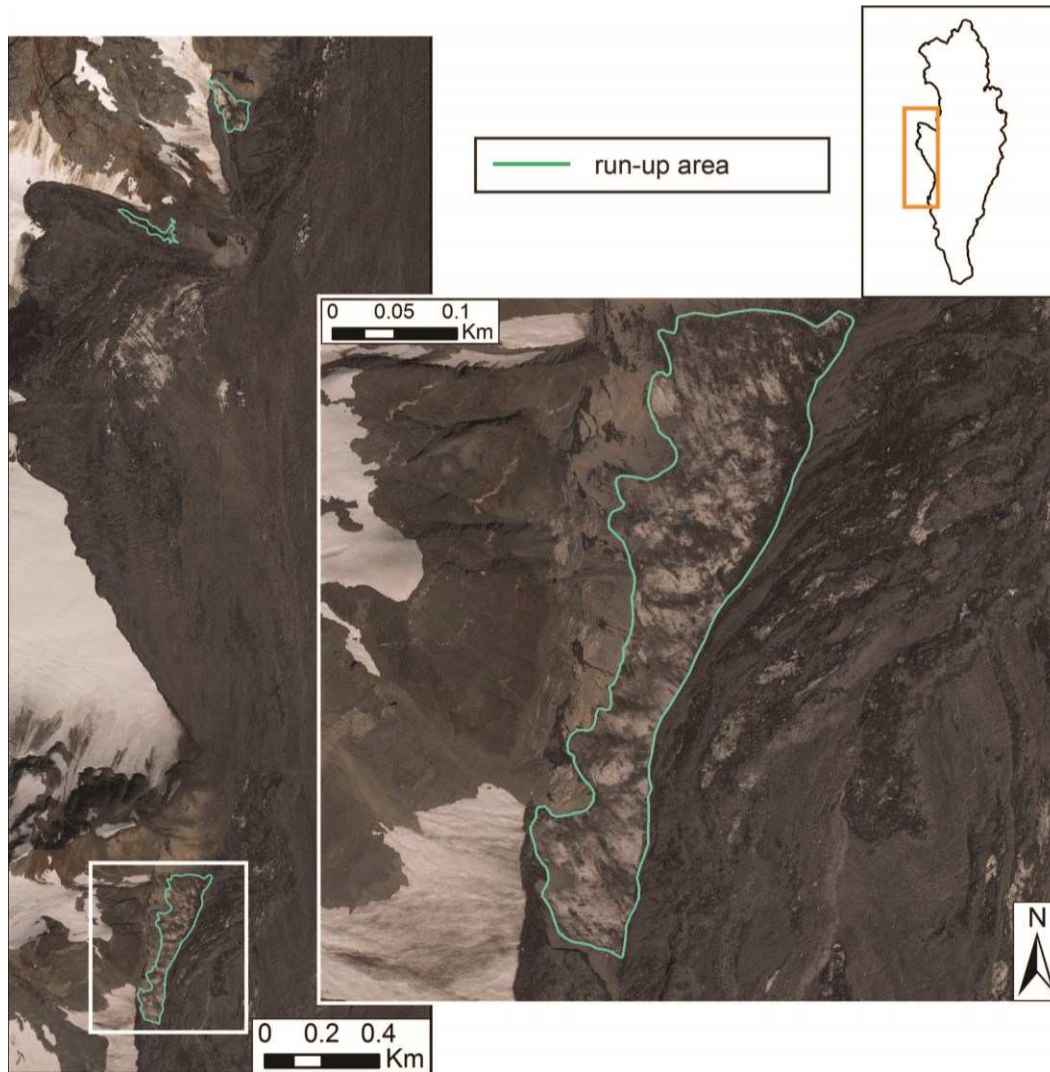


Figure 5-11. Digital Globe, Inc. imagery from 7/16/2016 showing locations of run-up along the west lateral margin of the Lamplugh rock avalanche.

CHAPTER 6 DISCUSSION

6.1 Independent Checks on Volume Analysis Methodology

As described in previous sections, many uncertainties are intrinsic to volume measurements of rock avalanches emplaced on glaciers. The following sections discuss the extent to which these uncertainties are accounted for in the calculations made in this research.

6.1.1 Seasonal Snow and Ice Change

As discussed in Section 4.7, the analysis of rock avalanche deposit geometry is complicated by non-uniform background elevation changes associated with dynamic glacial processes and the variable, elevation controlled climate of GBNP. Seasonal variations in snowpack and both seasonal and long-term ice loss likely contribute to these observed changes. As noted previously, the average annual ice loss on the Lamplugh Glacier between 2000 and 2005 was 0.54 meters per year (Loso et al., 2011). Seasonal fluctuations in the elevation of the ice surface, particularly during the ablation season, may differ from the total amount of annual ice change. The daily ablation rate on the Brady Glacier, which is directly adjacent to the Lamplugh Glacier and shares a flow divide at approximately 750 m a.s.l. (Loso et al., 2011), was measured as 14.3 mm/day during the summer melt season (Pelto, 2010). The measurement of daily ablation rate is based on the transient snow line, which represents the transition from bare glacier ice to areas covered in snow, and is assumed to be regionally similar between the Lamplugh and Brady glaciers, based on their proximity. Since no additional data is available for the Lamplugh Glacier, 14.3 mm/day was used to represent the maximum possible rate of elevation change due to seasonal ice loss on the Lamplugh Glacier. The interaction between rates

of seasonal and long-term ice loss is likely complex and since this research is based solely on data from one melt season, long-term rates of ice loss were not taken into consideration.

Snowfall records for the study area are sparse and snowfall amounts at the closest weather stations, all of which are located at sea level, are expected to vary drastically from the amounts of snowfall at elevations between 700 and 2,000 m a.s.l. The National Operational Hydrologic Remote Sensing Center (2004) operates a nationwide snow depth model as part of the Snow Data Assimilation System (SNODAS) program. Although the model for Alaska is experimental, SNODAS data was used to approximate snow depth on the surface of the Lamplugh Glacier in June, July, August, and September. This approximation is crude, but provides a baseline to compare against elevation differences observed from DEM differencing. The seasonal ice loss and approximate change in snow depth between 6/15/2016-7/16/2016, 7/16/2016-8/27/2016, and 8/27/2016-9/28/2016 was compared with the average elevation change observed on the glacier surface in each of the corresponding differenced DEMs (Table 6-1). The

Table 6-1. Estimated snow and ice changes compared to the average elevation change observed on the glacier surface between 6/15/2016-7/16/2016, 7/16/2016-8/27/2016, and 8/27/2016-9/28/2016.

Date Range	Average snow cover change (from SNODAS) (m)	Average ice loss (based on Pelto, 2010) (m)	Average total snow and ice loss (m)	Observed change in elevation (differenced DEM) (m)
6/15/2016-7/16/2016	-0.57	-0.44	-1.01	-1.84 ± 0.72
7/16/2016-8/27/2016	-1.02	-0.60	-1.62	-3.46 ± 0.53
8/27/2016-9/28/2016	0.03	-0.46	-0.43	-1.56 ± 0.55

discrepancies between observed and estimated elevation change are likely due to snow and ice changes that are not accounted for in the estimated value of seasonal ablation and/or the snow depth model.

6.1.2 Ice Insulation and Differential Melting

Post-event changes within the Lamplugh rock avalanche deposit and on the adjacent glacier surface demonstrate differential melting as a result of insulation in areas covered by debris. The role of ice insulation, which results in an increase in apparent deposit thickness with an increase in time between observations, is exemplified by comparing differenced cross-sections between 6/15/2016-7/16/2016 and 6/15/2016-8/27/2016 (Figure 6-1). The maximum thickness of the transverse profile measured between 6/15/2016 and 7/16/2016 is 18.6 meters, while the maximum thickness of the deposit appears to be 21.3 meters when measured between 6/15/2016 and 8/27/2016.

The insulating role of rock avalanche debris on underlying glacier surfaces has been previously documented from both laboratory experiments and field measurements (Reznichenko et al., 2011). The presence of rock avalanche debris acts primarily to shield underlying ice from solar radiation and the wide distribution of grain size, that is typical of rock avalanche deposits, results in a high thermal inertia (a large quantity of heat is required to cause an increase in temperature) (Reznichenko et al., 2011). Deposit thicknesses greater than 10 centimeters can reduce ice ablation by 25-75% (Jiskoot, 2011), while thicknesses in excess of 2 to 3 meters reduce melting of the underlying ice surface to nearly zero (Reznichenko et al., 2011). In the case of very thin deposits (<2 cm) the presence of a debris cover increases the ablation of underlying ice (Jiskoot, 2011). The average thickness of different areas within the Lamplugh

rock avalanche deposit varies between 1.4 and 11.6 meters. Based on previously documented rates of reduced ablation as a result of debris cover, it is expected that ablation beneath the Lamplugh rock avalanche deposit is reduced by between 25-100%. The rate of differential melting between areas covered by the rock avalanche deposit and the adjacent glacier surface ranged from 37.5% to 60% between 7/16/2016 and 9/28/2016. The amount of this change that is exclusively related to reduced ablation cannot be quantified because changes in elevation due to melting of underlying ice cannot be differentiated from melting of entrained snow and ice or compaction within the deposit.

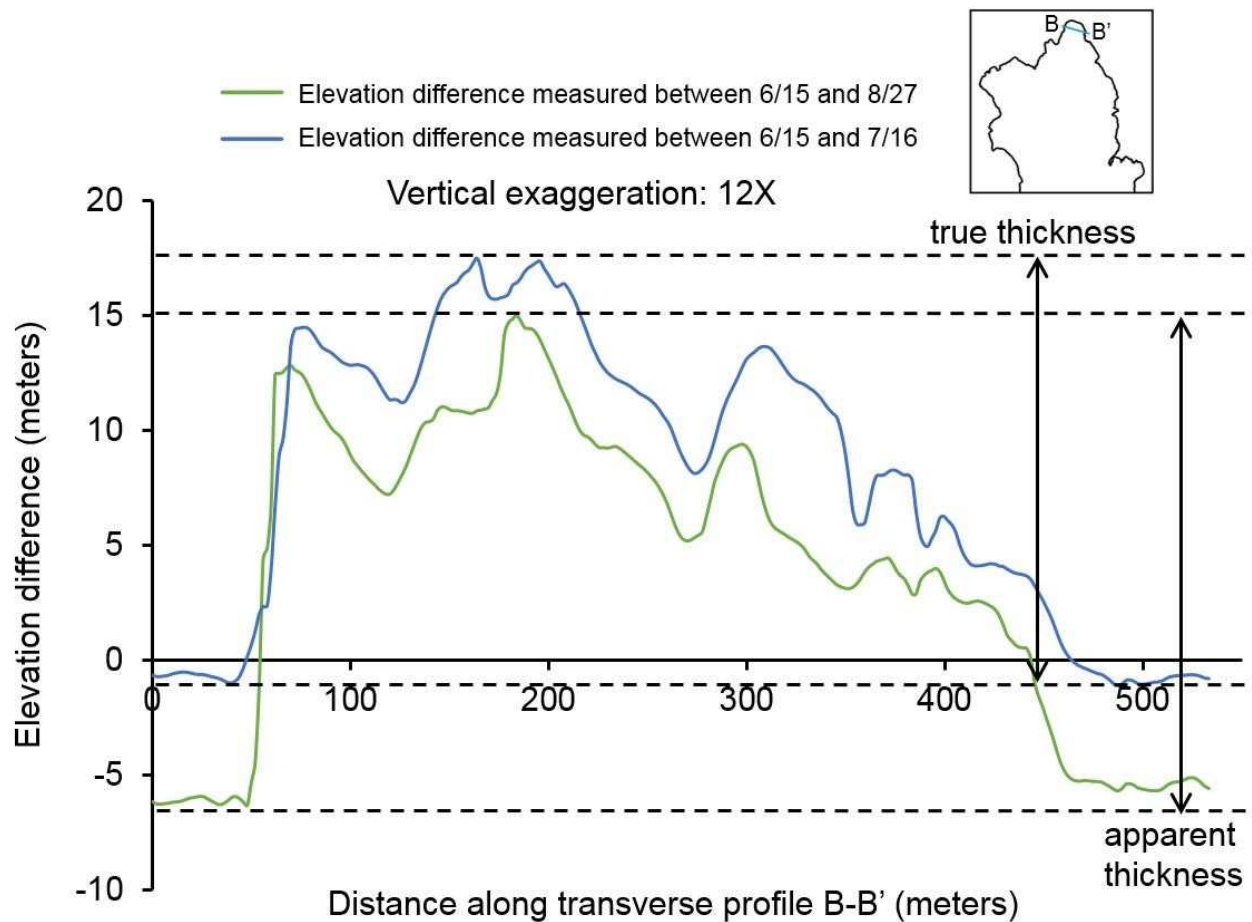


Figure 6-1. Differenced cross-sections taken along a transverse profile through the deposit toe between 6/15/2016-7/16/2016 and 6/15/2016-8/27/2016. An increase in observed thickness ($\Delta = 2.7$ meters) with an increase in time between observations demonstrates differential melting between deposit-covered areas and the adjacent surface.

Although it is evident that differential melting between the Lamplugh rock avalanche deposit and the adjacent surface is present, it is unlikely that the amount of melting and compaction that occurs within the deposit is completely uniform. Since the deposit is acting as an insulator to the underlying ice, it is reasonable to assume that thicker areas of the deposit would provide more insulation in comparison to thinner areas of the deposit. This could contribute to elevation differences within the deposit as a result of differential melting rather than processes associated with emplacement. Post-event changes between 7/16/2016-8/27/2016 and 8/27/2016-9/28/2016 show a generally uniform loss of elevation throughout the deposit. The spatial distribution of elevation loss is not significantly different in thin versus thick areas of the deposit. Post-event elevation loss in fensters is higher than in surrounding areas and is approximately equal to the elevation loss on the surrounding glacier. Since the thickness of the deposit is greater than the range of thicknesses which have been documented to cause increased melting of underlying ice, the maximum amount of unmeasured melting within the deposit area is not expected to exceed the amount of melting that is observed on the adjacent glacier surface.

6.1.3 Volume Calculation

The quantification of unmeasured changes on the glacier surface and within the deposit between the pre- and post-event DEMs and the time of avalanche occurrence, as discussed in Section 5.4, results in a total deposit volume that is more than twice that which was calculated from the raw differenced DEM between 6/15/2016-7/16/2016. Table 6-2 compares the modified and apparent volumes and average thickness for each area of the deposit. The source volume is not included in this comparison, since elevation adjustments were not made in this area.

The difference between source (eroded material in Zone A) and total deposit volumes indicates that the mass of failed material increased in volume by 19% during emplacement. It is possible that a significant amount of snow and ice was part of the source material, which would result in an overestimation of the amount of bulking if some or all of the failed snow and ice

Table 6-2. Values of apparent and adjusted deposit volume and average thickness for each zone of the Lamplugh rock avalanche. Please refer to Figure 5-6 for zone delineation.

Zone	Apparent Volume (Mm³)	Adjusted Volume (Mm³)	Apparent Average Thickness (m)	Adjusted Average Thickness (m)	Percent Change
B	2.7	3.1	9.8	11.6	15%
C (scoured material)	-11.4	-14.2	0	-5.1	--
C (deposited material)	0	3.2	0	1.4	--
D	2.5	4.5	1.7	3.0	80%
E	1.7	16.7	0.2	1.4	882%
F	24.1	31.0	4.8	6.1	29%
TOTAL (+)	31.0	59.2	--	--	91%

melted during emplacement. Additionally, it is not known whether the scoured material consisted of snow and ice, rock and colluvium, or a combination of both. If rock and colluvium were part of the scoured area, incorporation of snow and ice would contribute to the observed increase in the volume of deposited material. The small amount of observable entrained snow and ice remaining in the deposit on 7/16/2016 gives some indication that the majority of snow and ice that was transported from either the source area or the scour zone melted during transport or shortly after deposition. Alternatively, entrained snow and ice may be present below the surface of the deposit, preventing it from being visible in optical imagery. The amount of bulking is difficult to quantify without knowledge of the amounts of snow and ice involved in failure and entrained along the travel path and without field observations of snow and ice content in the

deposit shortly after the event occurred. Previous work has suggested that the process of rock fragmentation alone can result in source volume expansion ranging from 15 to 25%, while larger bulking values are expected if substrate is entrained during emplacement (Jiskoot, 2011). The amount of bulking observed in the Lamplugh rock avalanche (19%) is within the range of the volume increase expected from rock fragmentation alone. This could indicate that the majority of material that was scoured and entrained along the travel path was snow and ice which subsequently melted and therefore did not contribute significantly to the calculation of deposit volume. Further conclusions cannot be drawn without field observations and knowledge of material properties.

6.1.4 Improvements on Volume Estimates

The volumetric analysis conducted for the Lamplugh rock avalanche is an improvement on existing volume estimates for rock avalanches travelling over ice. Rock avalanche volumes are typically calculated by multiplying an estimated average thickness by the deposit area or by using an established empirical correlation for volume as a function of area. The use of localized thickness measurements in previous rock avalanche studies has resulted in volume estimates that differ by up to nearly 300%. For example, observations of thickness in the Mount Steele, Canada rock avalanche deposit yielded a volume estimate of 28-81 Mm³ (Lipovsky et al., 2008). Observations of the variations in thickness within the Lamplugh rock avalanche deposit demonstrate how volume estimates in localized areas could cause such a range in the estimate of total volume. The use of empirical correlations relies on previous data which also has the potential to be generalized or inaccurate. Additionally, many reported literature values have not distinguished between source, scour and entrainment (bulking), and deposit volumes. This

differentiation is important to make since bulking is likely related to the dynamics of rock avalanche emplacement. Accurate estimations of volume require adequate pre- and post-event topography data, which are often difficult to acquire. Additional factors, such as erosion, or snow and ice changes in the case of rock avalanches on glaciers, further complicate volume calculations.

Integration of differences between pre- and post-event topography (Equation 4-7) has been used to calculate volume in previous studies of mass movements, including landslides (Tsutsui et al., 2007) and debris flows (Coe et al., 1997). The method utilized in this thesis applies previously established techniques to rock avalanches on glaciers, but extends and improves on these techniques by taking into account the effect of snow and ice changes on observed geometry. The results of this analysis provide significantly more detail on the deposit geometry than can be obtained through generalized estimates of volume and thickness that are typical of most well-documented rock avalanches. This method also provides a means of examining effects related to emplacement, including the loss of material due to scour and entrainment, the distribution of mass throughout the deposit, and relatively small elevation changes related to the formation of surficial features and landslide structures that are indicative of movement dynamics.

Elevation adjustments related to unmeasured ice melt are important to consider and have a demonstrably significant effect on the overall calculation of volume. The adjustments made in this research account for changes on the adjacent glacier surface due to melting between the acquisition of pre- and post-event imagery and the rock avalanche occurrence and post-event changes within the deposit. Several additional sources of elevation change exist, but were outside the scope of this research. Decreases in elevation on the ice surface during emplacement from

plowing or scour by the moving rock mass (Delaney and Evans, 2014) or melting from the generation of frictional heat (Sosio et al., 2012) were not taken into account.

6.2 Deposit Geometry Comparisons

A striking observation from the differenced DEM of the Lamplugh rock avalanche is that the material deposited at the distal and lateral margins is thicker than interior areas of the deposit. The average thickness of the distal rim is 6.1 meters, with upper end, 95th percentile thickness values of 14.0 meters and 11.8 meters along the confined and unconfined portions of the rim, respectively. The average thickness of the interior transport zone (Zone E) is 1.4 meters. The lateral and distal rims account for 25% of the total deposit area, but contain 54% of the total volume of deposited material. In comparison, the transport zone makes up 55% of the total deposit area and contains 27% of the total deposit volume. This observation alone indicates the presence of a thickness distribution in the Lamplugh rock avalanche deposit that has not been documented in detail elsewhere.

As discussed in Section 2.1.2, distal rims and lateral ridges are commonly observed in rock avalanches travelling over various substrates. However, a lack of detailed quantitative data has made it difficult to compare the relative thickness between distal or lateral rims and ridges with other areas of the deposit. In many cases, the thickness of the distal margin or localized observations from other areas of the deposit are used to represent thickness across the entire deposit, further muting the recognition of a change in thickness at the distal margin, if it does exist.

Detailed pre- and post-event topographic data is necessary to thoroughly examine thickness distributions throughout a deposit. Few such datasets exist and those that do are very

difficult to obtain from published literature. One dataset that does exist is from the 2014 West Salt Creek rock avalanche in Collbran, Colorado. Pre- and post-event topographic data for the West Salt Creek rock avalanche were obtained through the Colorado Geological Survey and the U.S. Geological Survey. A comparison of normalized differenced profiles through the deposit toes of the Lamplugh and West Salt Creek rock avalanches (Figure 6-2) shows a significantly larger difference in relief between the distal margin and more proximal parts of the Lamplugh rock avalanche deposit. It is important to note that the West Salt Creek rock avalanche was confined and therefore a direct comparison is not fully reflective of the differences in transport processes between the partially unconfined travel of the Lamplugh rock avalanche and similar events travelling over rock or soil. Regardless of this discrepancy, Figure 6-2 shows a significant difference in the distribution of material at the distal edges of the Lamplugh and West Salt Creek rock avalanches, which likely has implications related to the emplacement mechanism of each event. For example, compared to the West Salt Creek rock avalanche, the Lamplugh rock avalanche appears to have had multiple, highly mobile, flow-like surge fronts that progressively accumulated at the distal margin. This is evidenced by the irregular toe profile which appears to indicate a series of multiple thrust faults.

The lack of detailed rock avalanche studies, which include field data and topographic information makes it difficult to reconcile qualitative observations of distal rims and theoretical thickness distribution models that have been hypothesized for these types of events. For example, in his descriptions of the Elm rock avalanche Heim noted the presence of a distal rim that is higher than the middle of the deposit, but also recognizes an approximate linear decrease in deposit thickness with distance from the headscarp (as cited in Hsü, 1975). The thickness difference between the distal rim and interior areas of the Lamplugh rock avalanche varies

significantly from both documented descriptions of deposit features and theoretical thickness distribution models for rock avalanches travelling over rock and soil. Additionally, a comparison of deposit geometry with the West Salt Creek rock avalanche provides a quantitative measure of this difference. The presence of a thick distal rim in contrast to an otherwise thin deposit is reflected in qualitative observations of other rock avalanches travelling over ice (McSaveney, 2002; Shreve, 1966; Shugar and Clague, 2011) but conflicting descriptions and a lack of quantitative data make it difficult to draw concrete comparisons with the Lamplugh rock avalanche.

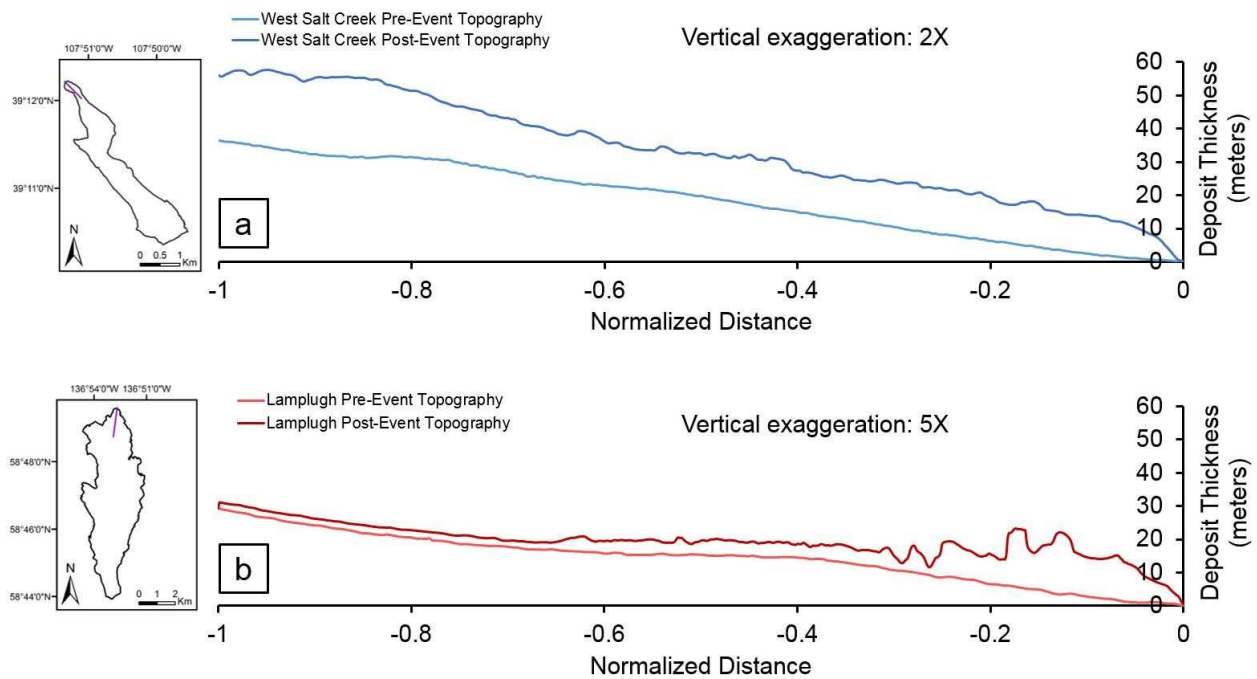


Figure 6-2. Normalized differenced cross-sections through the toes of the Lamplugh and West Salt Creek rock avalanches show a difference in relief between the distal rim and more proximal areas of the deposit.

The magnitude and spatial distribution of lateral ridges and distal rims are an important aspect of the overall distribution of deposit material with distance from the source. The location

of the center of mass of a landslide deposit is often considered to be a more representative metric of landslide mobility in place of the more widespread method of measuring mobility as the ratio between the total height of fall (H_{\max}) and the total length of the deposit (L_{\max}) (Legros, 2002). The location of the center of mass can also be used to assess the distribution of mass throughout the deposit. One would expect that the center of mass of a thin deposit with a relatively thick distal rim would be located farther from the point of origin in comparison with a deposit of uniform thickness or a deposit that decreases in thickness with distance from the source. The relative location of the center of mass can be quantified by determining the ratio between the longitudinal distance of the center of mass measured from the point of origin (L) and the total length of the deposit measured from the point of origin (L_{\max}). For the purposes of this thesis, the ratio between L and L_{\max} is designated as the normalized center of mass ratio (COM_N).

Center of mass data from several well-studied rock avalanches travelling both over rock or soil and ice is compared to COM_N calculated for the Lamplugh rock avalanche in Table 6-3. Center of mass data for nine rock avalanches travelling over rock and soil, as reported in Locat et al. (2006), and four rock avalanches travelling over ice, available from Delaney and Evans (2014) and Ekström and Stark (2013) were used to investigate the relationship between COM_N and event type. Plots comparing COM_N for rock avalanches travelling over rock and soil versus ice, and in confined versus unconfined settings, are shown in Figure 6-3a and b, respectively. In Figure 6-3, COM_N is represented by the slope of the regression line for each dataset, showing that based on the limited data available, the centers of mass of rock avalanches travelling over ice are located closer to the distal margin than that of rock avalanches travelling over rock and soil. Differences in the center of mass location for confined versus unconfined events (no differentiation between substrates) is not significant. The effect of unconfined versus confined

spreading is difficult to assess since completely confined spreading rarely occurs because of topographic variation inherent to the locations that are most prone to large rock slope failures. Therefore, these datasets may not represent a true separation between confined and unconfined travel.

Table 6-3. Center of mass locations for rock avalanches travelling over rock/soil and ice and in confined and unconfined topographic settings.

	L (km)	L_{max} (km)	COM_N	Source
Rock/Soil, unconfined				
Jonas Creek North	1.59	2.80	0.57	Locat et al., 2006
Claps de Luc	0.31	0.80	0.39	Locat et al., 2006
La Medeleine	1.85	4.50	0.41	Locat et al., 2006
Charmonetier	0.48	0.60	0.79	Locat et al., 2006
Jonas Creek South	1.29	1.83	0.70	Locat et al., 2006
Rock/soil, confined				
Frank Slide	1.55	3.50	0.44	Locat et al., 2006
Slide Mountain	0.42	1.65	0.26	Locat et al., 2006
Queen Elizabeth	0.88	2.65	0.33	Locat et al., 2006
Arvel	0.12	0.35	0.33	Locat et al., 2006
Ice, unconfined				
Lamplugh (right)	6.47	10.50	0.62	this research
Ice, confined				
Mount Munday	2.62	4.61	0.57	Delaney and Evans, 2014
Mt. Stellar	3.28	9.01	0.36	Eckstrom and Stark, 2013
Mt. Steele	3.35	6.00	0.56	Eckstrom and Stark, 2013
Mt. Lituya	2.41	7.07	0.34	Eckstrom and Stark, 2013
Lamplugh (left)	6.02	10.50	0.57	this research

In this research COM_N is used as a proxy for thickness distribution because the availability of detailed data on variations in rock avalanche deposit thickness is limited. However, it is important to note that overall geometric differences may not always be reflected by the location of the center of mass. For example, the location of the center of mass will be at or near the center of the deposit for both a completely uniform deposit and a deposit with a thin interior, but a uniformly thick rim around the entire margin. While COM_N may be a useful metric for some rock avalanche deposits, it may not accurately represent the distribution of thickness for

all deposit geometries. The measure of COM_N should ideally be used in conjunction with transverse profiles to understand the distribution of thickness in rock avalanche deposits.

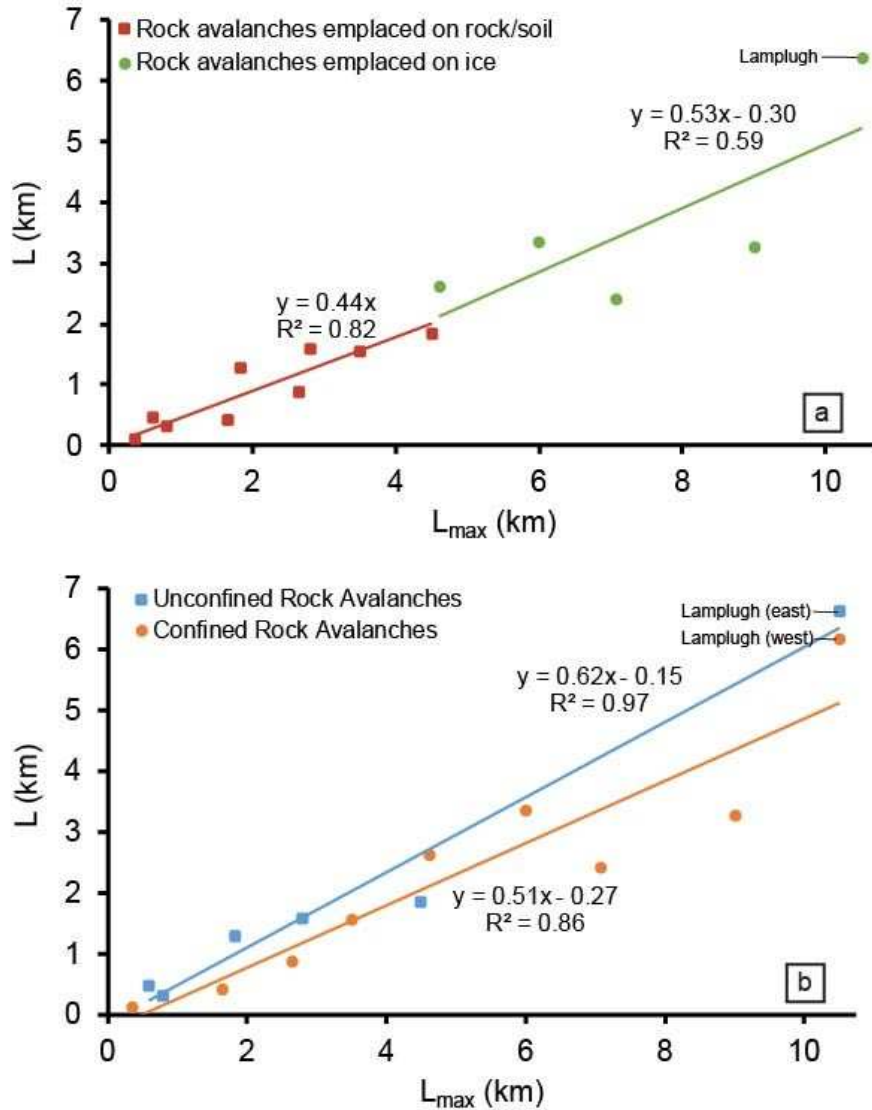


Figure 6-3. Plots of L_{max} versus L for a) rock avalanches travelling over rock/soil and ice and b) confined and unconfined rock avalanches.

6.3 Emplacement Hypotheses

DEMs from 6/15/2016 and 7/16/2016 show positive and negative elevation changes in the area of the 6/28/2016 Lamplugh rock avalanche. These elevation changes represent the

failure and emplacement of the rock avalanche in addition to any pre- or post-event changes that occurred on the adjacent ice surface or within the avalanche deposit. The changes that are observed can be attributed to either depletion from the initial rock failure, accumulation, or scour and entrainment of material in different locations within the deposit. A defining feature of the Lamplugh rock avalanche deposit is the large variation in thickness between different parts of the deposit. It can be reasonably hypothesized that the differential thickness distribution is due to either differential accumulation of material during emplacement or uniform accumulation of material during emplacement and differential melting on the surface or within the deposit after deposition. The maximum amount of ice melt that is reasonably expected to occur between the dates of pre- (6/15/2016) and post-event (7/16/2016) DEMs will not be larger than the amount of ice melt that was observed on the adjacent glacier surface during the same time period. The average change in elevation on the adjacent glacier surface (measured from Figure 5-2) is -1.84 meters and the 95th percentile of observed ice loss is -2.44 meters. Additionally, melting within the deposit during two different post-event periods (Figure 5-4) is approximately uniform throughout the deposit and does not exceed an average rate of -0.03 meters per day, which gives a total decrease in elevation by -1.02 meters for the 31 day period between 6/15/2016 and 7/16/2016. Although it is likely that the presence of snow and ice within the freshly emplaced deposit caused a greater rate of melting within the deposit between 6/15/2016 and 7/16/2016 than that which was observed later in the summer, it is not logical to conclude that this amount of melting can account for all of the elevation change observed within the deposit. The difference in average thickness between the distal and lateral rims and the remainder of the deposit is 4.7 meters, while the difference between the 95th percentile values of observed thickness in these areas is 9.7 meters. The difference between the average amount of depletion within the scour

zone and the average thickness of the remainder of the deposit is 7.6 meters. Similarly, the difference in the 5th percentile values (which corresponds to the maximum amount of scour) of elevation loss between the scoured area and the remainder of the deposit is 10.4 meters. These observations indicate that the amounts of differential accumulation and depletion of material within the Lamplugh rock avalanche deposit are too large to be attributed solely to changes in elevation from snow and ice melt.

An integrated examination of relatively large deposit features and smaller structures and surficial features within the Lamplugh rock avalanche deposit allows for the formulation of hypotheses regarding the progression of events that occurred during failure and emplacement. The presence of deposited material in combination with an overall decrease in elevation in Zone C indicates that material was removed from the surface before the final deposition of material occurred. Since Zone C is located directly downslope from the source area it is likely that the rapidly moving block of failed material from the source area scoured and entrained a large amount of surficial material from Zone C. The presence of thin debris surrounded by thick distal and lateral rims indicates that material moved readily across the glacier surface and accumulated at the margins upon deceleration and an eventual loss of energy.

Scour and entrainment in rock avalanches travelling on ice has been recognized, but the role and degree of material incorporation are not well quantified. Entrainment of snow and ice along the travel path of a rock avalanche causes an increase in deposit volume and may also affect the rheology of the rock avalanche mass by causing reductions in basal friction and material density (Sosio, 2015). Changes in the material characteristics of rock avalanches during emplacement can lead to increased mobility (Hung & Evans, 2004). Features indicative of entrainment, including scoured channels (McSaveney, 2002) and pits (Jibson et al., 2006) have

been directly observed in the travel paths of rock avalanches emplaced on glaciers. Lipovsky et al. (2008) measured a material loss of at least 16 meters in scoured areas along the travel path of the Mount Steele, Canada rock avalanche. Laboratory experiments (Schneider et al., 2011b) and numerical modelling (Sosio et al., 2012) have demonstrated reductions in friction of rock avalanche material upon the incorporation of ice. However, a lack of data and the difficulty of quantifying the amount of snow and ice in rock avalanche deposits contribute to a poor understanding of the degree to which ice entrainment affects the travel distance and overall emplacement characteristics of rock avalanches. The identification and quantification of a large area of scoured material along the travel path of the Lamplugh rock avalanche shows that as much as 14.2 Mm³ of snow and ice was incorporated into the original volume of failed material. Excluding contributions of snow and ice from the source area or other parts of the travel path, and assuming that all of the entrained material was snow and ice, the incorporated material from Zone C accounts for 23% of the total depleted material. This amount of snow and ice is significant and undoubtedly played a role in the mechanism of emplacement.

The accumulation of material below the source area (Zone B) and the presence of an internal toe feature (Zone D) in addition to the presence of thrust faults, fensters, and strike-slip faults provide evidence that emplacement occurred in multiple surges as opposed to a single mass of material. The presence of thrust faults in many segments of the lateral and distal rim indicates that multiple surges of material were progressively piled up against material that had previously come to rest. The presence of fensters also indicates that emplacement happened as a series of events, with fensters created during relatively late movement. The removal of deposited material to create fensters would only be possible if a previous surge had emplaced material that could then be removed by later movement. Strike-slip faults throughout the deposit show the

occurrence of multiple sequences of differential movement during emplacement, which is more plausible if sequential surges of material continued to cause adjustments of previously emplaced material. Differential movement is especially evident along portions of the toe where strike-slip faulting is manifested in the formation of offset lobes along the distal and lateral margins. The internal toe may be interpreted as a late surge of material that lost energy and material and stopped in a much more proximal area than any of the previous surges. The accumulation of material in Zone B is likely due to relatively small-scale failures of material from the source area that continued after the remainder of the deposit was emplaced.

The presence of a thin deposit bordered by thick lateral and distal rims indicate that much of the deposited material moved readily over the glacier surface before being emplaced along the margins of the rock avalanche deposit. Increased spreading due to low-friction ice surfaces has been demonstrated experimentally (Dufresne, 2012; Schneider et al., 2011b), but reduced basal friction alone will result in increased translation without significant differences in the thickness of the deposit (Davies et al., 1999). Snow and ice within the deposit either from the failed mass or scour and entrainment may also contribute to increased spreading by reducing frictional resistance within the mass of material, but the incorporation of snow and ice is not sufficient to solely cause the amount of runout that has been observed in nature (Schneider et al., 2011b). Dynamic fragmentation was first reported by Davies et al. (1999) as a mechanism to explain the long runout of rock avalanches and it has since been hypothesized that increased fragmentation of rock avalanches travelling on ice further contributes to increased spreading (Delaney and Evans, 2014). Fragmentation of rock during runout induces high particle velocities in multiple directions, which act to increase momentum and kinetic energy, consequently reducing deceleration of the moving rock mass (Davies et al., 1999). Delaney and Evans (2014) assert that

low-friction ice surfaces increase the amount of fragmentation that occurs within a travelling rock mass, which in turn causes increased spreading in comparison to rock avalanches travelling over higher friction substrates. The mechanisms of emplacement presented by Delaney and Evans (2014) and Davies et al. (1999) are consistent with the features observed in the Lamplugh rock avalanche deposit.

Based on the observation of overall rock avalanche geometry in conjunction with the identification of structures, interpretations about the sequence of events that occurred during failure and emplacement of the Lamplugh rock avalanche can be made. Initially, 49.8 Mm³ of rock failed from the source area and travelled onto a slope covered in snow and ice, while descending approximately 1,000 meters in elevation. As the moving mass continued to move downslope, 14.2 Mm³ of additional material, much of which was likely snow and ice, was scoured from the surface and entrained into the rock avalanche mass. Upon reaching the glacial valley, the mass began moving across the surface in a series of surges. The first surge of material stopped near the location of the distal margin and the following surges of material progressively plowed into previously emplaced material along the lateral and distal edges. Shearing occurred between the lateral edges of new surges and previously emplaced material, forming several generations of strike-slip faults. Local extension and compression that occurred during the differential movement of individual surges, created fensters and transverse ridges, respectively. After the main failure and emplacement of material, a relatively small amount of material continued to fail from the source area and accumulated at the base of the slope. A detailed understanding of the sequence and type of movement that occurs during rock avalanche emplacement is a critical step in developing an understanding of movement dynamics.

CHAPTER 7 CONCLUSION

High-resolution, pre- and post-event DEMs derived from stereo satellite imagery were used to quantify relatively large morphologic features indicative of the distribution of material within the Lamplugh rock avalanche deposit. Additionally, the use of high-resolution optical imagery enabled the identification of structures and surficial features within the rock avalanche deposit. The source volume was found to be 49.8 Mm^3 and the deposit volume was found to be 59.2 Mm^3 , yielding a 19% increase in material volume during emplacement. Scour and entrainment of 14.2 Mm^3 of material along the travel path indicates that up to nearly a quarter of the total eroded material could have been snow and ice, which likely had significant impacts on deposit rheology and emplacement. The distribution of material within the Lamplugh rock avalanche deposit varies significantly from reported rock avalanche thickness distribution models. The Lamplugh rock avalanche deposit is characterized by lateral and distal rims with an average thickness of 6.1 meters. The accumulation of material along the deposit edges is significant in comparison to the interior of the deposit, which is covered in thin deposits with an average thickness of 1.4 meters. The difference in thickness between the distal and lateral rims and the surrounding deposit is distinct from features typically found in rock avalanches travelling over rock or soil and indicates disparities in emplacement mechanisms. Irregular geometry in the toe of the Lamplugh rock avalanche provides evidence for the accumulation of multiple, flow-like surges of material, likely indicating differences in material characteristics of both the deposit and the substrate in comparison to rock avalanches travelling over rock and soil.

The integrated use of elevation data and optical imagery allowed for improved volume estimates both because of the fine resolution of input data and because of the ability to incorporate estimations of the effects of dynamic glacial processes. Perhaps even more important

than the estimation of total source and deposit volumes is the ability to examine the spatial variation of volume within the deposit in great detail. The methods used in this research are an improvement of past volume estimates for large rock avalanches in glaciated environments. Additionally, the use of elevation data facilitated the identification of structures and surficial features, further demonstrating the utility of integrated remotely sensed datasets as a means of studying rock-ice avalanches.

Observations of increasing magnitude and frequency of rock avalanche failures in glacial environments necessitates an improved understanding of failure and emplacement mechanisms as a means of informing future hazard assessments. The study of these events is particularly critical in light of evidence indicating that rapidly changing global climate conditions are linked to both the long-term conditioning and potential driving factors of massive rock slope failures in mountainous regions. This research demonstrates the ability to use the integration of elevation data and optical imagery to remotely study rock avalanches emplaced on glaciers. In the future, the increasing availability of high-resolution data will further promote the use of remote sensing data as a means of understanding the mechanisms relevant to failure and emplacement of rock avalanches on glaciers.

REFERENCES

- Alaska Department of Natural Resources, Information Resource Management. (1998a). *Alaska Coastline 1:63,360* [Data file] Retrieved from <http://www.asgdc.state.ak.us/#56>
- Alaska Department of Natural Resources, Information Resource Management. (1998b). *Alaska Glaciers 1:1,000,000* [Data file] Retrieved from <http://www.asgdc.state.ak.us/#2970>
- Bessette-Kirton, E.K. & Coe, J.A. (2016). Inventory of rock avalanches in western Glacier Bay National Park and Preserve, Alaska, 1984-2016: a baseline data set for evaluating the impact of climate change on avalanche magnitude, mobility, and frequency. U.S. Geological Survey data release. <https://doi.org/10.5066/F7C827F8>
- Beyer, R., Alexandrov, O., McMichael, S., Moratto, Z., Broxton, M. J., Nefian, A., Hancher, M., Lundy, M., To, V., & Edwards, L. (2016). The Ames Stereo Pipeline: NASA's Open Source Automated Stereogrammetry Software A part of the NASA NeoGeography Toolkit Version 2.5.3. Intelligent Robotics Group, NASA Ames Research Center. https://byss.arc.nasa.gov/stereopipeline/binaries/asp_book-2.5.3.pdf
- Bottino, G., Chiarle, M., Joly, A., & Mortara, G. (2002). Modelling rock avalanches and their relation to permafrost degradation in glacial environments. *Permafrost and Periglacial Processes*, 13(4), 283–288. <https://doi.org/10.1002/ppp.432>
- Coe, J. A., Bessette-Kirton, E. K., & Geertsema, M. (2017). Rock avalanches in Glacier Bay National Park, 1984-2016: a preliminary assessment of 33 years of Landsat data on avalanche magnitude, mobility, and frequency. Conference paper in press.
- Coe, J. A., Baum, R. L., Allstadt, K.E., Kochevar, B. F., Jr., Schmitt, R. G., Morgan, M. L., White, J. L., Strannon, B. T., Hayashi, T. A., & Kean, J. W. (2016). Rock-avalanche dynamics revealed by large-scale field mapping and seismic signals at a highly mobile avalanche in the West Salt Creek valley, western Colorado. *Geosphere*, 12(2), 607-631. <https://doi.org/10.1130/GES1265.1>
- Coe, J. A., Glancy, P. A., & Whitney, J. W. (1997). Volumetric analysis and hydrologic characterization of a modern debris flow near Yucca Mountain, Nevada. *Geomorphology*, 20, 11-28.
- Connor, C., Streveler, G., Post, A., Monteith, D., and Howell, W. (2009). The Neoglacial landscape and human history of Glacier Bay, Glacier Bay National Park and Preserve, southeast Alaska, USA. *The Holocene*, 19(3), 381–393.
- Cox, S. C., & Allen, S. K. (2009). Vampire rock avalanches of January 2008 and 2003, Southern Alps, New Zealand. *Landslides*, 6, 161–166. <https://doi.org/10.1007/s10346-009-0149-4>

- Davies, T. R., McSaveney, M. J., & Hodgson, K. A. (1999). A fragmentation-spreading model for long-runout rock avalanches. *Canadian Geotechnical Journal*, 36, 1096–1110. <https://doi.org/10.1139/t99-067>
- Davis, J. C. (2002). *Statistics and Data Analysis in Geology: Third Edition*. New York, NY: John Wiley & Sons, Inc.
- Delaney, K. B., & Evans, S. G. (2014). The 1997 Mount Munday landslide (British Columbia) and the behaviour of rock avalanches on glacier surfaces. *Landslides*, 11(6), 1019–1036. <https://doi.org/10.1007/s10346-013-0456-7>
- Deline, P., Hewitt, K., Reznichenko, N., & Shugar, D. (2015). Rock Avalanches onto Glaciers. In Davies, T. & Shroder, J. F. Jr., (Eds.) *Landslide Hazards, Risks, and Disasters* (pp. 263–270). <http://dx.doi.org/10.1016/B978-0-12-396452-6.00009-4>
- DigitalGlobe, Inc. (2016a). Accuracy of WorldView Products. DigitalGlobe White Paper. Retrieved from https://dg-cms-uploads-production.s3.amazonaws.com/uploads/document/file/38/DG_ACCURACY_WP_V3.pdf
- DigitalGlobe, Inc. (2016b). WorldView-1. DigitalGlobe Data Sheet. Retrieved from https://dg-cms-uploads-production.s3.amazonaws.com/uploads/document/file/99/WorldView1-DS-WV1_V02.pdf
- DigitalGlobe, Inc. (2016c). WorldView-2. DigitalGlobe Data Sheet. Retrieved from <https://dg-cms-uploads-production.s3.amazonaws.com/uploads/document/file/98/WorldView2-DS-WV2-rev2.pdf>
- DigitalGlobe, Inc. (2016d). WorldView-3. DigitalGlobe Data Sheet. Retrieved from https://dg-cms-uploads-production.s3.amazonaws.com/uploads/document/file/95/DG_WorldView3_DS_forWeb_0.pdf
- Dewberry (2013). IFSAR Quality Assurance (QA) Report: QA Report for FEDI Glacier Bay Cells 319, 320, 321, 322, 336, 337, 338, and 339, Produced for U.S. Geologic Survey.
- Dufresne, A., & Davies, T. R. (2009). Longitudinal ridges in mass movement deposits. *Geomorphology*, 105(3–4), 171–181. <https://doi.org/10.1016/j.geomorph.2008.09.009>
- Dufresne, A., Prager, C., & Bösmeier, A. (2016). Insights into rock avalanche emplacement processes from detailed morpho-lithological studies of the Tschirgant deposit (Tyrol, Austria). *Earth Surface Processes and Landforms*, 41(5), 587–602. <https://doi.org/10.1002/esp.3847>
- Ekström, G. & Stark, C. P. (2013). Simple scaling of catastrophic landslide dynamics. *Science (New York, N.Y.)*, 339(6126), 1416–1419. <https://doi.org/10.1126/science.1232887>

- Eppler, D. B., Fink, J., & Fletcher, R. (1987). Rheologic Properties and Kinematics of Emplacement of the Chaos Jumbles Rockfall Avalanche, Lassen Volcanic National Park, California. *Journal of Geophysical Research*, 92(B5), 3623-3633.
- Evans, S. G., Hungr, O., & Eneqren, E. G. (1994). The Avalanche Lake rock avalanche, Mackenzie Mountains, Northwest Territories, Canada: description, dating, and dynamics. *Canadian Geotechnical Journal*, 31, 749-768.
- Evans, S. G., & Clague, J. J. (1999). Rock avalanches on glaciers in the Coast and St. Elias Mountains, British Columbia. In: *Proceedings of the 13th Annual Vancouver Geotechnical Society Symposium*, Vancouver, (pp. 115-123).
- Evans, S. G., & Clague, J. J. (1994). Recent climatic change and catastrophic geomorphic processes in mountain environments. *Geomorphology*, 10(1-4), 107-128. [https://doi.org/10.1016/0169-555X\(94\)90011-6](https://doi.org/10.1016/0169-555X(94)90011-6)
- Evans, S. G., & Delaney, K. B. (2015). *Catastrophic Mass Flows in the Mountain Glacial Environment*. In Haeberli, W., Whiteman, C., and Shroder, J. F. Jr., (Eds.) *Snow and Ice-Related Hazards, Risks, and Disasters* (pp. 563-606). <https://doi.org/10.1016/B978-0-12-394849-6.00016-0>
- Fahnestock, R. K. (1978). Little Tahoma Peak Rockfalls and Avalanches, Mount Rainier, Washington, U.S.A. In: Voight, B. (Ed.), *Rockslides and Avalanches, 1 Natural Phenomena*. *Developments in Geotechnical Engineering 14A* (6), (pp. 181-196). New York, NY: Elsevier.
- Friedmann, S. J., Taberlet, N., & Losert, W. (2006). Rock-avalanche dynamics: Insights from granular physics experiments. *International Journal of Earth Sciences*, 95, 911-919. <https://doi.org/10.1007/s00531-006-0067-9>
- Geertsema, M., & Cruden, D. M. (2008). Travels in the Canadian Cordillera. In: *Proceedings of the 4th Canadian Conference on Geohazards*, 12. <https://doi.org/10.13140/2.1.1580.3208>
- Geertsema, M., Clague, J. J., Schwab, J. W., & Evans, S. G. (2006). An overview of recent large catastrophic landslides in northern British Columbia, Canada. *Engineering Geology*, 83(1-3), 120-143. <https://doi.org/10.1016/j.enggeo.2005.06.028>
- Geertsema, M. (2012). Initial observations of the 11 June 2012 rock/ice avalanche, Lituya Mountain, Alaska. In: Wei, S., Ying, G., & Chengcheng, Z. (Eds.), *Proceedings of the First Meeting of Cold Region Landslides Network (International Consortium on Landslides)*, Harbin, (pp. 49-53). <https://doi.org/10.13140/2.1.2473.5682>
- Gruber, S., & Haeberli, W. (2007). Permafrost in steep bedrock slopes and its temperatures-related destabilization following climate change. *Journal of Geophysical Research*, 112, F02S18. <https://doi.org/10.1029/2006JF000547>

- Hadley, J. B., (1978). Madison Canyon Rockslide, Montana, U.S.A. In: Voight, B. (Ed.), *Rockslides and Avalanches, 1 Natural Phenomena. Developments in Geotechnical Engineering 14A (6)*, (pp. 167-180). New York, NY: Elsevier.
- Hewitt, K., Clague, J. J., & Orwin, J. F. (2008). Legacies of catastrophic rock slope failures in mountain landscapes. *Earth-Science Reviews*, *87*, 1–38.
<https://doi.org/10.1016/j.earscirev.2007.10.002>
- Hewitt, K. (2009). Rock avalanches that travel onto glaciers and related developments, Karakoram Himalaya, Inner Asia. *Geomorphology*, *103*, 66-79.
<https://doi.org/10.1016/j.geomorph.2007.10.017>
- Hsü, K. J. (1975). Catastrophic Debris Streams (Sturzstroms) Generated by Rockfalls. *Geological Society of America Bulletin*, *86*, 129-140.
- Hsü, K. J. (1978). Albert Heim: Observations on Landslides and Relevance to Modern Interpretations. In: Voight, B. (Ed.), *Rockslides and Avalanches, 1 Natural Phenomena. Developments in Geotechnical Engineering 14A (6)*, (pp. 71-93). New York, NY: Elsevier.
- Huggel, C., Clague, J. J., & Korup, O. (2012). Is climate change responsible for changing landslide activity in high mountains? *Earth Surface Processes and Landforms*, *37*(1), 77-91.
<https://doi.org/10.1002/esp.2223>
- Hungr, O., & Evans, S. G. (2004). Entrainment of debris in rock avalanches: An analysis of a long run-out mechanism. *Geological Society of America Bulletin*, *116*(9–10), B25362.
<https://doi.org/10.1130/B25362.1>
- Korup, O. & Dunning, S. (2015). Catastrophic mass wasting in high mountains. In Huggel, C., Carey, M., Clague, J. J., & Käab, A., (Eds.) *The High-Mountain Cryosphere: Environmental Changes and Human Risks* (pp. 127-146). Cambridge, United Kingdom: Cambridge University Press.
- Jibson, R. W., Harp, E. L., Schulz, W., & Keefer, D. K. (2006). Large rock avalanches triggered by the M 7.9 Denali Fault, Alaska, earthquake of 3 November 2002. *Engineering Geology*, *83*(1–3), 144–160. <https://doi.org/10.1016/j.enggeo.2005.06.029>
- Jiskoot, H. (2011). Long-runout rockslide on glacier at Tsar Mountain, Canadian Rocky Mountains: potential triggers, seismic and glaciological implications. *Earth Surface Processes and Landforms*, *36*, 203–216. <https://doi.org/10.1002/esp.2037>
- Johnson, B. (1978). Blackhawk Landslide, California, U.S.A. In: Voight, B. (Ed.), *Rockslides and Avalanches, 1 Natural Phenomena. Developments in Geotechnical Engineering 14A (6)*, (pp. 181-196). New York, NY: Elsevier.

- Krautblatter, M., Huggel, C., Deline, P., & Hasler, A. (2012). Short Communication Research Perspectives on Unstable High-alpine Bedrock Permafrost: Measurement, Modelling and Process Understanding. *Permafrost and Periglacial Processes*, 23(1), 80-88. <https://doi.org/10.1002/ppp.740>
- Larsen, C. F., Motyka, R. J., Freymueller, J. T., Echelmeyer, K. A., & Ivins, E. R. (2005). Rapid viscoelastic uplift in southeast Alaska caused by post-Little Ice Age glacial retreat. *Earth and Planetary Science Letters*, 237, 584-560. <https://doi.org/10.1016/j.epsl.2005.06.032>
- Larsen, C. F., Motyka, R. J., Arendt, A. A., Echelmeyer, K. A., & Geissler, P. E. (2007). Glacier changes in southeast Alaska and northwest British Columbia and contribution to sea level rise. *Journal of Geophysical Research*, 112, F01007. <https://doi.org/10.1029/2006JF000586>
- Legros, F. (2002). The mobility of long-runout landslides. *Engineering Geology*, 63(3-4), 301-331. [https://doi.org/10.1016/S0013-7952\(01\)00090-4](https://doi.org/10.1016/S0013-7952(01)00090-4)
- Lipovsky, P. S., Evans, S. G., Clague, J. J., Hopkinson, C., Couture, R., Bobrowsky, P., Bobrowsky, Ekström, G., Demuth, M. N., Delaney, K. B., Roberts, N. J., Clarke, G., & Schaeffer, A. (2008). The July 2007 rock and ice avalanches at Mount Steele, St. Elias Mountains, Yukon, Canada. *Landslides*, 5, 445-455. <https://doi.org/10.1007/s10346-008-0133-4>
- Loso, M., Arendt, A., Larsen, C., Rich, J., & Murphy, N. (2011). Alaskan National Park Glaciers, Status and Trends. *National Resource Technical Report NPS/AKRO/NRTR-2014/922*.
- Marangunic, C. & Bull, C. (1966). The Landslide on the Sherman Glacier. In: The Great Alaska Earthquake of 1964 (Hydrology, Part A), Publication 1603. National Academy of Sciences, Washington, D.C., (pp. 383-394).
- McSaveney, M. J. (2002). Recent rockfalls and rock avalanches in Mount Cook National Park, New Zealand. *Reviews in Engineering Geology*, 15, 35-70. <https://doi.org/10.1130/REG15-p35>
- McSaveney, M. J. (1978). Sherman Glacier rock avalanche, Alaska, U.S.A. In: Voight, B. (Ed.), *Rockslides and Avalanches, 1 Natural Phenomena*. Developments in Geotechnical Engineering 14A (6), (pp. 197-258). New York, NY: Elsevier.
- Mudge, M. R. (1965). Rockfall-Avalanche and Rockslide-Avalanche Deposits at Sawtooth Ridge, Montana. *Geological Society of America Bulletin*, 76, 1003-1014.
- National Operational Hydrologic Remote Sensing Center (2004). *Snow Data Assimilation System (SNODAS) data products at NSIDC*. Boulder, CO: National Snow and Ice Data Center. Digital media.

- National Park Service. (2014). *National Park Boundaries* [Data file] Retrieved from <https://catalog.data.gov/dataset/national-park-boundariesf0a4c>
- Pelto, M.S. (2010). Satellite Identification of Transient Snowline Variation During the Melt Season for Mass Balance Assessment Taku and Brady Glacier, Alaska. In: Pelto, M. & Kelly, R. (Eds.) *Proceedings of the 67th Eastern Snow Conference*, Hancock, MA (pp. 51-60).
- Petley, D. (2016, July 3). Lamplugh Glacier rock avalanche: A massive new landslide in Alaska on Tuesday. The Landslide Blog, AGU. Retrieved from <http://blogs.agu.org/landslideblog/2016/07/03/lamplugh-glacier-rock-avalanche-1/>
- Petley, D. (2014, February 22). Mount La Perouse: Sunday's rock avalanche in Alaska has been found. The Landslide Blog, AGU. Retrieved from <http://blogs.agu.org/landslideblog/2014/02/22/mount-la-perouse-rock-avalanche/>
- Petley, D. (2014, February 25). Mount La Perouse rock avalanche: more images. The Landslide Blog, AGU. Retrieved from <http://blogs.agu.org/landslideblog/2014/02/25/mount-la-perouse-rock-avalanche-2/>
- Pflaker, G., Hudson, T., Bruns, T., & Rubin, M. (1978). Late Quaternary offsets along the Fairweather fault and crustal plate interactions in southern Alaska. *Canadian Journal of Earth Sciences* 15, 805-816.
- Post, A. (1967). Effects of the March 1964 Alaska earthquake on glaciers. U. S. Geological Survey Professional Paper, 544-D, 42.
- Pudasaini, S. P., & Krautblatter, M. (2014). A two-phase mechanical model for rock-ice avalanches. *Journal of Geophysical Research* 119(10), 2272–2290. <https://doi.org/10.1002/2014JF003183>
- Reznichenko, N. V., Davies, T. R. H., & Alexander, D. J. (2011). Effects of rock avalanches on glacier behaviour and moraine formation. *Geomorphology*, 132, 327-338. <https://doi.org/10.1016/j.geomorph.2011.05.019>
- Schneider, D., Huggel, C., Haerberli, W., & Kaitna, R. (2011a). Unraveling driving factors for large rock-ice avalanche mobility. *Earth Surface Processes and Landforms* 36(14), 1948-1966. <https://doi.org/10.1002/esp.2218>
- Schneider, D., Kaitna, R., Dietrich, W. E., Hsu, L., Huggel, C., & McArdell, B. W. (2011b). Frictional behavior of granular gravel-ice mixtures in vertically rotating drum experiments and implications for rock-ice avalanches. *Cold Regions Science and Technology*, 69(1), 70–90. <https://doi.org/10.1016/j.coldregions.2011.07.001>

- Shean, D. E., Alexandrov, O., Moratto, Z. M., Smith, B. E., Joughin, I. R., Porter, C., & Morin, P. (2016). An automated, open-source pipeline for mass production of digital elevation models (DEMs) from very-high-resolution commercial stereo satellite imagery. *ISPRS Journal of Photogrammetry and Remote Sensing*, *116*, 101-117. <https://doi.org/10.1016/j.isprsjprs.2016.03.012>
- Shugar, D. H., & Clague, J. J. (2011). The sedimentology and geomorphology of rock avalanche deposits on glaciers. *Sedimentology*, *58*, 1762–1783. <https://doi.org/10.1111/j.1365-3091.2011.01238.x>
- Shreve, R. L. (1968). Sherman Landslide. In: The Great Alaska Earthquake of 1964 (Hydrology, Part A), Publication 1603. National Academy of Sciences, Washington, D.C., (pp. 395-401).
- Shreve, R. L. (1968a). The Blackhawk Landslide. *Geological Society of America Special Paper*, *108*, 47 p. <https://doi.org/10.1130/SPE108-p1>
- Sosio, R., Crosta, G. B., Chen, J. H., & Hungr, O. (2012). Modelling rock avalanche propagation onto glaciers. *Quaternary Science Reviews*, *47*, 23-40. <https://doi.org/10.1016/j.quascirev.2012.05.010>
- Tsutsui, K., Rokugawa, S., Nakagawa, H., Miyazaki, S., Cheng, C. T., Shiraishi, T., & Yang, S. (2007). Detection and volume estimation of large-scale landslides based on elevation-change analysis using DEMs extracted from high-resolution satellite stereo imagery. *IEEE Transactions on Geoscience and Remote Sensing*, *45*(6), 1681-1696. <https://doi.org/10.1109/TGRS.2007.895209>
- U. S. Geological Survey. (2012). *USGS NED Original Product Resoution (OPR) AK_IFSAR-GB-338_2012 ArcGrid* [Data file]. Retrieved from <https://earthexplorer.usgs.gov/>
- U. S. Geological Survey, National Geospatial-Intelligence Agency, & National Aeronautics and Space Administration. (2000). *Shuttle Radar Topography Mission 1 Arc-Second Global: SRTMIN58W137V3* [Data file]. Retrieved from [https://earthexplorer.usgs.gov/Wieczorek, G.F., Geist, E.L., Motyka, R. J., & Jakob, M. \(2007\). Hazard assessment of the Tidal Inlet landslide and potential subsequent tsunami, Glacier Bay National Park, Alaska. *Landslides*, *4*, 205-215. <https://doi.org/10.1007/s10346-007-0084-1>](https://earthexplorer.usgs.gov/Wieczorek,G.F.,Geist,E.L.,Motyka,R.J.,&Jakob,M.(2007).HazardassessmentoftheTidalInletlandslideandpotentialsubsequenttsunami,GlacierBayNationalPark,Alaska.Landslides,4,205-215.https://doi.org/10.1007/s10346-007-0084-1)
- Wilson, F.H., Hulst, C.P., Mull, C.G., & Karl, S.M. (2015). Geologic map of Alaska: *U.S. Geological Survey Scientific Investigations Map 3340*, 197 p., 2 sheets, scale 1: 584,000. <http://dx.doi.org/10.3133/sim3340>.

APPENDIX A

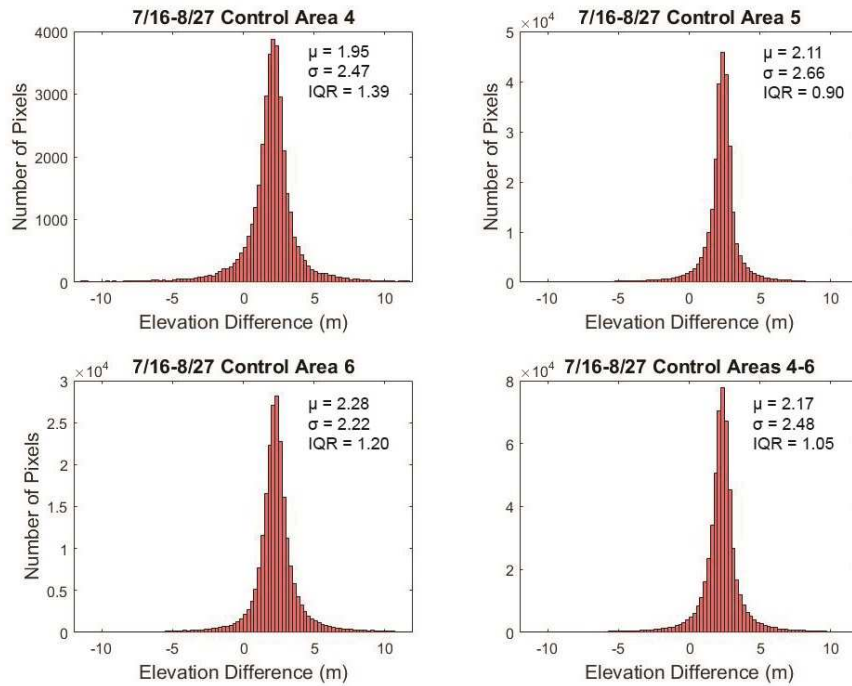


Figure A-1. Elevation difference in Control Areas 4-6 between ASP DEMs from 7/16/2016 and 8/27/2016.

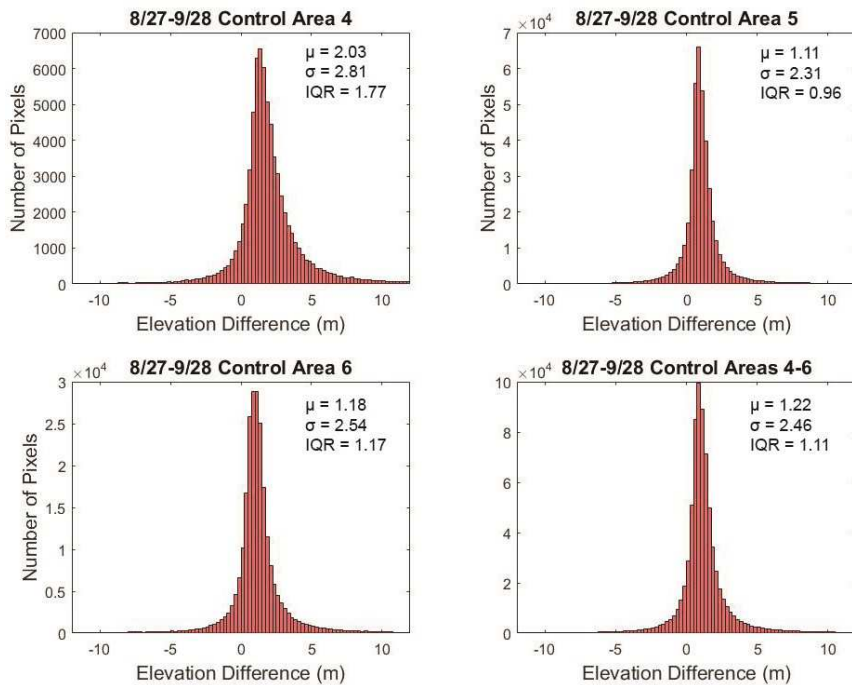


Figure A-2. Elevation difference in Control Areas 4-6 between ASP DEMs from 8/27/2016 and 9/28/2016.

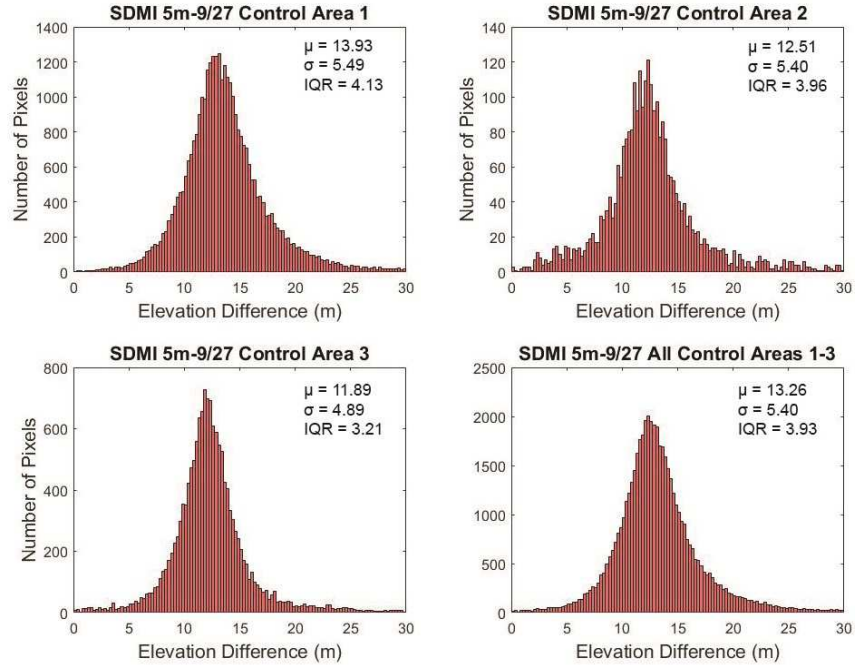


Figure A-3. Elevation difference in Control Areas 1-3 between SDMI 5-meter and ASP-generated 9/27/2016 DEMs.

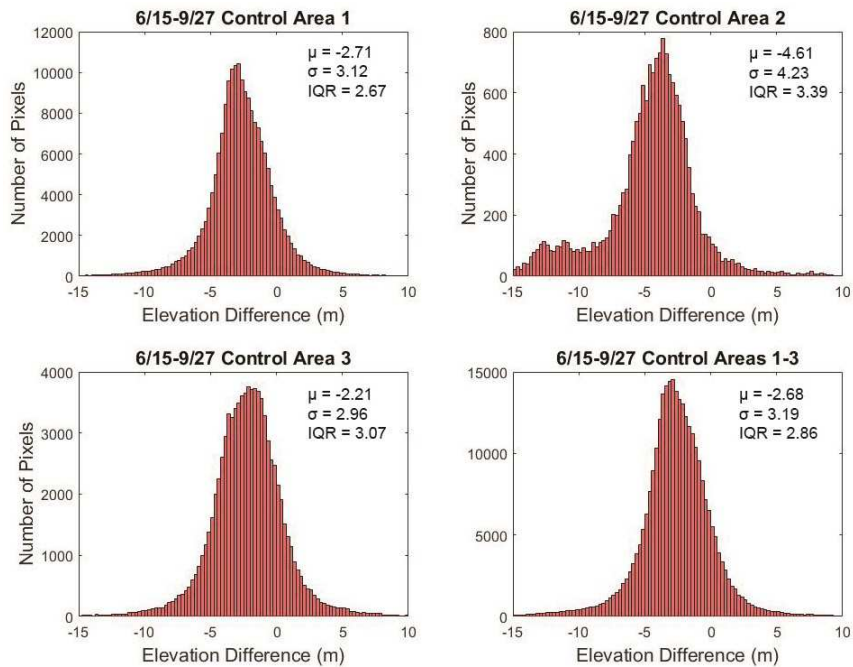


Figure A-4. Elevation difference in Control Areas 1-3 between ASP DEMs from 6/15/2016- and 9/27/2016.

APPENDIX B



Figure B-1. Digital Globe, Inc. image of the Lamplugh rock avalanche on 7/16/2016 that was used for mapping of structures and surficial features.

APPENDIX C

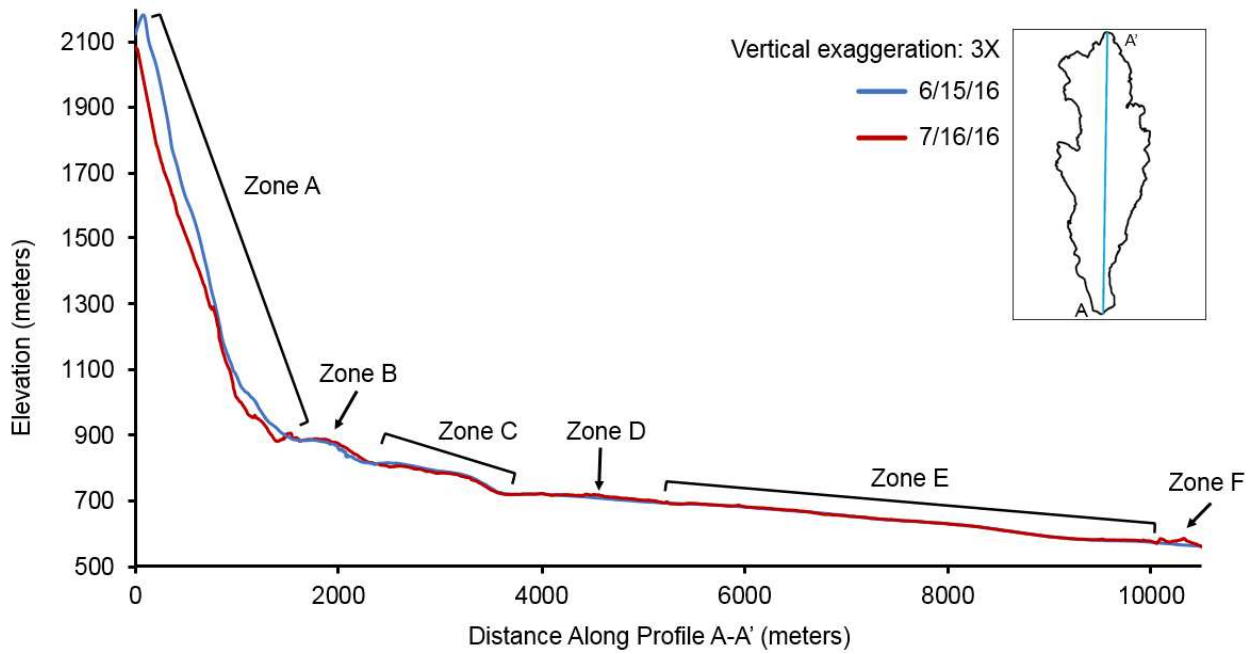


Figure C-1. Pre- and post-event elevation profiles along A-A' showing the location of zones A-F. Pre-event elevation data is derived from a 5-meter resolution SDMI DEM (source area only) and the ASP-generated DEM from 6/15/2016. Post-event elevation data is derived from DEMs from 9/27/2016 (source area only) and 7/16/2016.

APPENDIX D

SUPPLEMENTAL ELECTRONIC FILES

The supplemental file included with this thesis is a complete map of structures and surficial features in the Lamplugh rock avalanche mapped at a scale of 1:16,000 on a Digital Globe, Inc. image from 7/16/2016. A simplified version of this map is included as Figure 5-7.